Politecnico di Torino

Politecnico di Torino

Master's Degree in

Mechatronic Engineering

Three-Phase Synchronous Machine: Digital Torque Control

Supervisors

Prof. Radu Iustin Bojoi

Prof. Sandro Rubino

Candidate

Giuseppe Francesco Cardone

Abstract

In these days,where the issue of environmental pollution and climate change is stronger than ever, the institutions of government around the world are looking for alternative and more sustainable ways to produce and consume energy.

The transports represent one of the biggest impacts of human beings on the planet and for this reason is nowadays at the centre of the global debate. Internal combustion engines had been crucial for the development of the modern economies since the end of the 19th century. However,despite the large improvements of these latter in recent decades, the increasingly stringent restrictions on emissions are forcing vehicle manufacturers to hybrid and electric power-trains.

In this scenario, the thesis' aim is the implementation and the comparison of what constitutes the state-of-the-art of the torque controllers for three-phase AC motors, with an in-depth analysis of non-electrically excited synchronous machines for traction applications.

Before deepening in the different control topologies, an accurate modelling of the electric machine combined with the power electronic converter is mandatory.

The generic synchronous machine is modelled considering the electrical and magnetic equations both with a model-based approach in Simulink and a mixed model/circuit-based approach in Plecs (Chapter 2). As sample machine, a large, highly saturated IPM machine from automotive industry is chosen.

The traction inverter is modelled as a two-level voltage source inverter (VSI) with a model-based approach in Simulink and a circuit-based approach in Plecs (Chapter 3). As sample inverter, one equipped with Microsemi power modules MSCSM120AM02CT6LIAG is considered. The input DC voltage dynamics is neglected and assumed constant.

Finally, the different motor control units implemented are modelled inside Simulink triggered subsystems in order to simulate the discrete-time dynamics of a real digital controller (Chapter 4).

About the control, the main requirements of an high-performance torque controller include the linearity of the torque regulation, the performance-independence from the operating point and the ease of adapting the control on other machines without tuning everything again. These constraints are satisfied in different ways according to the control scheme and the pros and cons of each solution will be emphasized.

In addition, in the last chapter, a dedicated solution for isotropic synchronous machines is proposed and Simulink simulated over an axial-flux synchronous machine provided by Texa (Chapter 5).

Contents

1 Introduction **2**

1.1 Digital torque control of three-phase AC machine 2

1.2 Radial flux synchronous machines classification 3

1.3 Stationary $\alpha\beta$ coordinates, rotor dq coordinates, stator dqs coordinates 4

2 Three-phase Synchronous Machine **7**

2.1 Machine characteristic equations 7

2.1.1 dq Electrical model 7

2.1.2 dq Magnetic model 8

2.1.3 dq Losses model 9

2.2 Matlab maps extrapolation 10

2.2.1 Four quadrants extension of maps 11

2.2.2 Direct and Inverse flux-linkage maps 12

2.2.3 Machine losses 13

2.2.4 Differential inductances 14

2.2.5 Torque maps,MTPA and MTPV 16

2.2.6 MTPS and Efficiency maps 18

2.3 Simulink machine models 24

2.3.1 Flux-based dq model 24

2.3.2 Current-based dq model 25

2.3.3 dq models with machine losses 25

2.4 Plecs machine models 27

2.4.1 Current-controlled generators model 27

2.4.2 Voltage behind reactance model 28

2.5 Open-loop tests of the four SM models 30

3 Voltage Source Inverter and Modulation Techniques **34**

3.1 Voltage source inverter 34

3.1.1 Operating principles of a 2-levels voltage source inverter . 35

3.1.2 Non-ideality phenomena 37

3.2 Modulation techniques 38
3.2.1 Sinusoidal-PWM 39
3.2.2 Space vector-PWM 40
3.3 Matlab maps extrapolation 41
3.3.1 On-state resistance map 41
3.3.2 Switching losses map 42
3.3.3 Dead-time selection and equivalent voltage drop 42
3.4 Simulink VSI model 43
3.5 Plecs VSI model 44
3.6 Open-loop tests of the block SVPWM-VSI-SM 45

4 Motor Control Unit **49**
4.1 Analog-to-digital conversion and execution delay 49
4.2 Position tracking observer 51
4.3 Stator flux observer 53
4.4 Control approaches in dq rotor coordinates 55
4.4.1 Current vector control (CVC) 56
4.4.2 Flux vector control (FVC) 60
4.5 Control approaches in dqs stator coordinates 62
4.5.1 Direct flux vector control (DFVC) and SVM-Direct torque control (SVM-DTC) 63
4.5.2 Flux polar control (FPC) 68
4.6 Predictive controllers 70
4.6.1 Model predictive control (MPC) 70
4.6.2 Deadbeat control (DB) 70
4.7 Closed-loop tests of the complete e-drive 72

5 Texa Motor **79**
5.1 Experimental flux and torque maps extrapolation 79
5.2 Differential inductances, MTPA, MTPV and MTPS 83
5.3 Proposed CVC 85

List of Figures

1.1 Typical layout of an e-drive digital torque control. 3
1.2 Radial Flux Synchronous machines:main rotor topologies. 4
1.3 $\alpha\beta$,dq and dqs frames. 5
2.1 Steady-state equivalent circuital model of the machine. 9
2.2 Flux maps in the $\mathbf{I}_{m,dq}$ plane. 12
2.3 Inverse Flux maps in the $\mathbf{\Lambda}_{dq}$ plane. 13
2.4 Differential inductances maps in the $\mathbf{I}_{m,dq}$ plane. 15
2.5 Torque maps in the $\mathbf{I}_{m,dq}$ plane. 16
2.6 IsoTorques,current limit,MTPA,MTPV in the $\mathbf{I}_{dq}$ plane. 18
2.7 IsoTorques,flux limit, MTPA, and MTPV in the $\mathbf{\Lambda}_{dq}$ plane. 18
2.8 Torque,Power and Efficiency in MTPS. 20
2.9 Current,Voltage and Flux in MTPS. 21
2.10 $\mathbf{I}_d$ map in the Torque,Speed plane. 23
2.11 $\mathbf{I}_q$ map in the Torque,Speed plane. 23
2.12 $\mathbf{I}_{dq}$ phase map in the Torque,Speed plane. 23
2.13 $\mathbf{I}_{dq}$ magnitude map in the Torque,Speed plane. 23
2.14 Efficiency map in the Torque,Speed plane. 23
2.15 PF absolute value map in the Torque,Speed plane. 23
2.16 Flux-based dq model. 24
2.17 Current-based dq model. 25
2.18 Flux-based dq model including losses. 26
2.19 Current-based dq model including losses. 26
2.20 Current-controlled generators model including losses. 27
2.21 Voltage behind reactance model including losses. 30
2.22 dq current dynamics in the OL tests of the four SM models. 32
3.1 Three-phase two-level VSI. 36
3.2 Voltage vectors of three-phase two-level VSI. 37
3.3 Sinusoidal modulation. 40
3.4 Space-vector modulation. 41
3.5 Temperature dependence of the ON-state resistance for the parallel of two SiC MOSFET. 41

3.6 Switching losses per phase with combined commutated current dependence. 42
3.7 Simulink / SV-PWM and VSI with non-ideality phenomena. . . . 43
3.8 Plecs / SV-PWM and VSI with non-ideality phenomena. 44
3.9 Torque,dq current and duty cycles dynamics in the OL tests of the SVPWM-VSI-SM block. 47
4.1 CB-PWM modulator. 50
4.2 Laplace block diagram PTO. 51
4.3 Simulink PTO. 52
4.4 Gopinath stator flux observer. 54
4.5 Bae-Patel-based considered control structure. 57
4.6 Laplace block diagram CVC. 58
4.7 Laplace block diagram FVC. 60
4.8 Laplace block diagram ds-axis DFVC/DTC/FPC. 63
4.9 Laplace block diagram qs-axis DFVC. 64
4.10 Laplace block diagram qs-axis DTC. 65
4.11 Laplace block diagram MTPV limiter DFVC. 66
4.12 Laplace block diagram qs-axis FPC. 68
4.13 Torque and dq current dynamics BP-CVC. 74
4.14 Torque and dq current dynamics LUTs-based-CVC 74
4.15 Torque and dq flux dynamics BP-FVC. 75
4.16 Torque and flux dynamics DTC-SVM. 75
4.17 Torque,flux and qs current dynamics DFVC. 76
4.18 Torque,flux and load angle dynamics LUTs-based-FPC. 76
4.19 Torque and $\alpha\beta$ flux dynamics Deadbeat-$\alpha\beta$FVC. 77
4.20 Torque and dq flux dynamics Deadbeat-dqFVC. 77

Texa motor

5.1 Grid of dq currents tested in the flux maps extrapolation. 80
5.2 Measured and computed torque in the flux maps extrapolation. . . 81
5.3 Flux and Torque maps in the $\mathbf{I}_{dq}$ plane. 82

5.4 Differential inductance maps in the $\mathbf{I}_{dq}$ plane. 83
5.5 IsoTorque lines, current limit, MTPA, MTPV in the $\mathbf{I}_{dq}$ plane. . . . 84
5.6 Electromagnetic Torque and Mechanical Power in MTPS. 84
5.7 dq inductance maps in the $II - III$ quadrants of the $\mathbf{I}_{dq}$ plane @hot. 86
5.8 dq inductance maps in the $II - III$ quadrants of the $\mathbf{I}_{dq}$ plane @cold. 86
5.9 Three regions partition of the $\mathbf{I}_{dq}$ plane. 87
5.10 Proposed CVC. 89
5.11 Torque, power, speed and dq current dynamics. 92
5.12 dq current and dq flux dynamics in the dq plane. 92

List of Tables

1 IPM parameters. 7
2 Test conditions SM models. 31
3 SiC MOSFET (MSCSM120AM02CT6LIAG) main specs. 34
4 Test conditions SVPWM-VSI-SM simulations. 46
5 Test conditions MCU-VSI-SM simulations. 73
6 Test conditions Texa motor. 91

Acronims and symbols

Acronim	Meaning
SM	Synchronous machine
AM	Asynchronous machine
PM	Permanent Magnet
SPM	Surface-mounted Permanent Magnet machine
IPM	Internal Permanent Magnet machine
$PM-SyR$	Permanent Magnet assisted Synchronous Reluctance machine
SyR	Synchronous Reluctance machine
$RFSM$	Radial Flux Synchronous machine
$AFSM$	Axial Flux Synchronous machine
$AFPM$	Axial Flux Permanent Magnet machine
MUT	Machine Under Test
DM	Driving Machine
$MTPA$	Maximum Torque per Ampere
$MTPV$	Maximum Torque per Voltage
$MTPS$	Maximum Torque per Speed
VSI	Voltage Source Inverter
$SV-PWM$	Space Vector Pulse Width Modulation
PTO	Position Tracking Observer
BP	Bae-Patel
CVC	Current Vector Control
FVC	Flux Vector Control
$DFVC$	Direct Flux Vector Control
DTC	Direct Torque Control
FPC	Flux Polar Control
FEA	Finite Element Analysis
MMF	Magneto-motive Force
EMF	Electro-motive Force
MCU	Motor Control Unit
pp	Pole Pairs

Symbol	Meaning
ω_e	Electrical Synchronous speed
ω_m	Rotor Mechanical speed
θ_d	Electrical angle
θ_m	Rotor Mechanical position
v	scalar
$\boldsymbol{v}$	vector
V	vector magnitude
$\mathbf{V}$	matrix
$\wedge$	Cross-product
$\circ$	Element-wise product
$\oslash$	Element-wise division

Chapter 1:
Introduction

Before moving into modeling and simulation, it is pertinent to provide readers with a generalized overview of modern e-drive architectures as well as a basic classification of three-phase synchronous machines.
In the chapter end, the most commonly used reference frames for control applications are presented.

1.1 Digital torque control of three-phase AC machine

The basic scheme reported in Figure 1.1 shows the generic implementation of a digital torque control for a three-phase motor for traction application.
Starting from left, there is the DC voltage (v_{dc}) provided by a HV traction battery, by a DC/DC converter connected to this latter or by a rectifier in AC-grid connected inverters. Furthermore, typically a large capacitor is put in parallel at the inverter input to stabilize the DC bus and to supply instantaneous current during switching transients.

Being the inverter input a voltage source, this latter is defined as a voltage source inverter. The purpose of a three-phase VSI is to apply a three-phase power supply to the machine. This latter is pulsed, but with the attempt of replicating a fundamental component equal to a sinusoidal reference with its own frequency and amplitude.

The three-phase stator of the electrical machine receive in input the three-phase voltages (v_a, v_b, v_c) and generates a rotating MMF which interacting with the rotor, allows the electromagnetic torque (Te) production. The mechanical speed (ω_m) dynamics depends on the load counter-torque, on the frictions, and on the total inertia seen by the drive shaft, since the machine acts as a torque generator.

The core of the control is represented by the Motor Control Unit (MCU), which implements the digital torque control. It takes in input the measured phase currents (i_a, i_b, i_c), the measured mechanical position (θ_m), the measured DC-link voltage, and the input reference torque (Te^*_{IN}), providing in output the six PWM commands ($q_a, q_b, q_c, \overline{q}_a, \overline{q}_b, \overline{q}_c$) which are sent to the gate drivers (not represented in Figure

1.1) and in the end control the six respective power switches in the inverter legs. The just-mentioned feedbacks are only the minimal set of controller inputs (not considering sensorless control). Many others can be added to refine the control strategy (e.g., sensed stator temperature (one or multiple), measured mechanical torque, measured line-to-line voltages, enables, fault signals...).

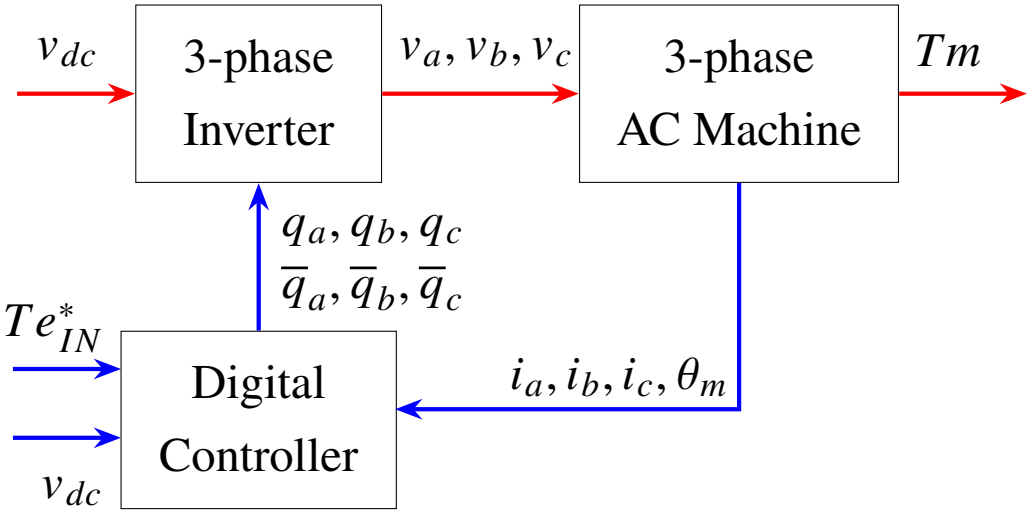

Figure 1.1: Typical layout of an e-drive digital torque control.

1.2 Radial flux synchronous machines classification

Four main types of three-phase non-electrically excited RFSMs can be distinguished:

- Surface-mounted Permanent Magnet (SPM)
- Internal Permanent Magnet (IPM)
- Permanent Magnet assisted Synchronous reluctance (PM-SyR)
- Synchronous reluctance (SyR)

In first approximation, the main differences between them concern the rotor part. Indeed, the quantity and the location of the permanent magnets on the rotor determine the motor's type and how this latter produces torque.
The Figure 1.2 below provides a schematic representation of the main rotor topologies.

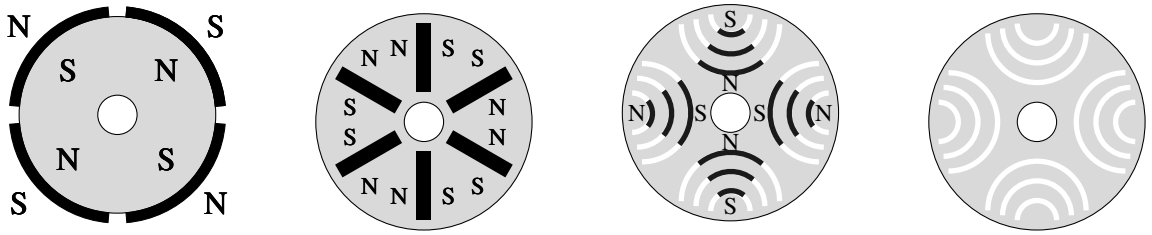

(a) $2pp$ SPM (b) $3pp$ IPM. (c) $2pp$ PM-SyR. (d) $2pp$ SyR.

Figure 1.2: Radial Flux Synchronous machines:main rotor topologies.

Thanks to isotropy, in SPM machine torque is produced exclusively due to the interaction between the PM magnetic field and the stator currents. On the other hand, SyR machines produce torque by anisotropy, whereby the rotor tries to minimize its magnetic energy. IPM and PM-SyR produce torque through a combination of these two phenomena.

1.3 Stationary $\alpha\beta$ coordinates, rotor dq coordinates, stator dqs coordinates

In order to accurately define all subsequent machine models and the associated control algorithms, it is necessary to introduce all the relevant coordinate systems.

First of all, the so-called $\alpha\beta$ frame is introduced. It is essentially a stationary complex plane where α represents the real axis and β the imaginary one. It is used to convert a three-phase system into a two-phase one as discussed in the appendix (A.1).
Another common adopted frame is the rotor dq one where the d-axis direction, hence the electrical angle θ_d with respect to the α axis, in this text is assumed to be in the same direction of the larger positive PM flux for SPM, IPM and PM-SyR machines and along the minimum reluctance/maximum inductance path for SyR machines.

Independently of the machine type the unified electromagnetic torque in rotor dq coordinates is expressed as:

$$T_e = \frac{3}{2} \cdot pp \cdot \boldsymbol{\lambda}_{dq} \wedge \boldsymbol{i}_{dq} = \frac{3}{2} \cdot pp \cdot \left(\lambda_d \cdot i_q - \lambda_q \cdot i_d\right) \tag{1}$$

Alternatively, using the stator dqs frame means assuming the ds axis along the stator's flux, with the qs axis in quadrature.

$$T_e = \frac{3}{2} \cdot pp \cdot \boldsymbol{\lambda}_{\boldsymbol{dqs}} \wedge \boldsymbol{i}_{\boldsymbol{dqs}} = \frac{3}{2} \cdot pp \cdot \left(\lambda_{ds} \cdot i_{qs}\right) \tag{2}$$

The scheme below (Figure 1.3) summarize the just discussed frames.

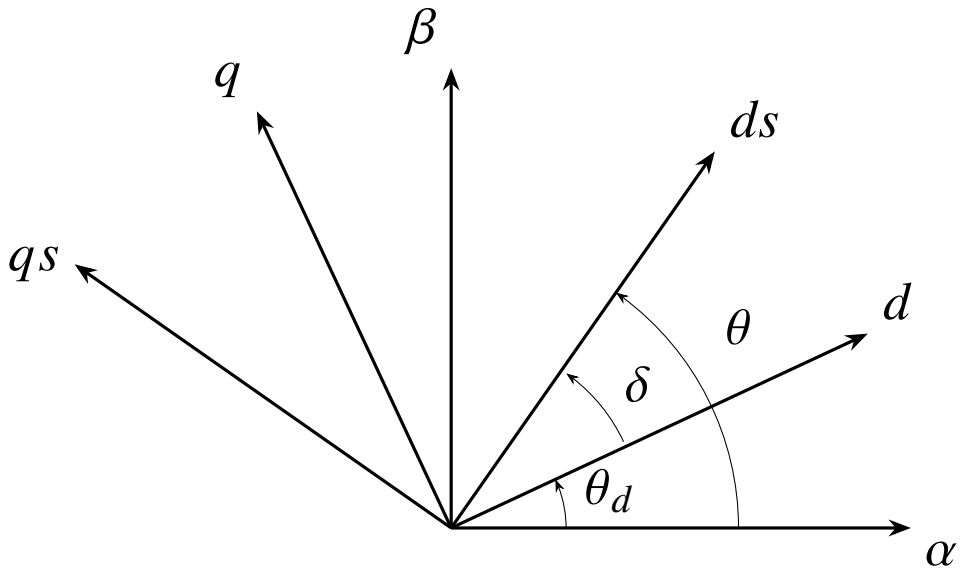

Figure 1.3: $\alpha\beta$,dq and dqs frames.

Unlike the $\alpha\beta$ frame, the dq and the dqs ones rotate at the electrical synchronous speed (ω_e). Therefore, since at steady state the space vectors associated to the three-phase currents, voltages and flux-linkages rotate as well at such speed, all these latter quantities become constant (apart from harmonics) in the dq and in the dqs frames.

Chapter 2:
Three-phase Synchronous Machine

As anticipated, an IPM machine will serve as a case study for modeling and simulation in the upcoming chapters.(Chapters:2,3,4).
The main specs of this latter machine are reported in Table 1:

Table 1: IPM parameters.

Motor			
Maximum Phase Current	I_{max}	1403.8	Apk
Maximum Speed	n_{max}	18100	rpm
Nominal Speed	n_0	4000	rpm
Nominal Frequency	f_0	200	Hz
Nominal DC Voltage	v_{dc0}	230	V
Peak Torque	Te_{peak}	431.5	Nm
Peak Power	P_{peak}	196.8	Kw
Pole Pairs	pp	3	/
Nominal Winding Temperature	T_{Cu0}	120	° C
Nominal PMs Temperature	T_{PM0}	80	° C
Nominal DC Stator Resistance @T_{Cu}	R_{s0}	0.00548	Ω
PMs Flux Linkage @$(i_{md} = 0, i_{mq} = 0, T_{Cu}, T_{PM})$	λ_{m0}	0.0558	Vs

2.1 Machine characteristic equations

2.1.1 *dq* Electrical model

Probably the most important ingredient for the construction of an electrical machine model is its characterization in the electrical domain. The so-called voltage equations do the job and relate voltages, currents and flux linkages in a single expression that is valid for all synchronous machines.

Starting from a three-phase stator modeling (Eq.3), the phase voltages are expressed as the sum of the voltage drop over the stator resistance and the phase flux linkage variation. This latter term includes both the inductive EMF due to the changing stator current and the motional EMF due to the rotor motion which involves an inductance variation and a magnets flux movement (more on this on Sec. 2.4.2).

Then, operating the direct Park transformation (A.5), it is possible to re-write the voltage equations in the rotor dq frame (Eq.4). In such a reference frame, a speed-dependent term appears explicitly, but this apparent model complication will be justified later due to a much easier magnetic model.

$$\begin{bmatrix} v_a \\ v_b \\ v_c \end{bmatrix} = R_s \begin{bmatrix} i_a \\ i_b \\ i_c \end{bmatrix} + \frac{d}{dt} \begin{bmatrix} \lambda_a \\ \lambda_b \\ \lambda_c \end{bmatrix} \tag{3}$$

$$\begin{bmatrix} v_d \\ v_q \end{bmatrix} = R_s \begin{bmatrix} i_d \\ i_q \end{bmatrix} + \frac{d}{dt} \begin{bmatrix} \lambda_d \\ \lambda_q \end{bmatrix} + \omega_e \begin{bmatrix} 0 & -1 \\ 1 & 0 \end{bmatrix} \begin{bmatrix} \lambda_d \\ \lambda_q \end{bmatrix} \tag{4}$$

2.1.2 dq Magnetic model

Secondly, it is necessary to characterize the machine behavior in the magnetic domain. Also in this case, the modeling starts from the three-phase system (Eq.5) where the phase flux linkages are obtained as the sum of a leakage term, a magnetizing one and the magnets flux contribution. This latter depends on the rotor position as well as the matrix of the magnetizing inductances **M**.

Afterwards, thanks to the Park transformation (A.5), the dq form is obtained (Eq.6). Here, the dependence on the rotor position disappears, the leakage phase inductances are hidden inside L_d and L_q and the saturation effects are encapsulated in a magnets flux linkage contribution λ_m expressed as function of i_q and in apparent inductances L_d and L_q that are functions of i_d and i_q.

$$\begin{bmatrix} \lambda_a \\ \lambda_b \\ \lambda_c \end{bmatrix} = \underbrace{L_{ls} \begin{bmatrix} i_a \\ i_b \\ i_c \end{bmatrix}}_{\text{Leakage term}} + \underbrace{\begin{bmatrix} L_{aa}(2\theta_d) & M_{ab}(2\theta_d) & M_{ac}(2\theta_d) \\ M_{ba}(2\theta_d) & L_{bb}(2\theta_d) & M_{bc}(2\theta_d) \\ M_{ca}(2\theta_d) & M_{cb}(2\theta_d) & L_{cc}(2\theta_d) \end{bmatrix} \begin{bmatrix} i_a \\ i_b \\ i_c \end{bmatrix}}_{\text{Magnetizing term}} + \underbrace{\lambda_{m0} \begin{bmatrix} \cos(\theta_d) \\ \cos(\theta_d - \frac{2\pi}{3}) \\ \cos(\theta_d + \frac{2\pi}{3}) \end{bmatrix}}_{\text{Magnets term}} \tag{5}$$

$$\begin{bmatrix} \lambda_d \\ \lambda_q \end{bmatrix} = \begin{bmatrix} L_d(i_d, i_q) & 0 \\ 0 & L_q(i_d, i_q) \end{bmatrix} \begin{bmatrix} i_d \\ i_q \end{bmatrix} + \begin{bmatrix} \lambda_m(i_q) \\ 0 \end{bmatrix} \tag{6}$$

Furthermore, λ_d and λ_q can be evaluated using two non-linear functions, which are implemented with the so-called flux linkage maps as done in Section 2.2.2.

2.1.3 *dq* Losses model

Ideally, all the electrical power provided to an electric machine is transformed into a mechanical one. However, in each physical system, losses are present and must be taken into account when dealing with accurate model construction. A complete description of the loss phenomena is outside the scope of this thesis, therefore some approximations are done here,in order not to over-complicate the model.
A sketch of the considered steady-state *dq* model, derived from [1], is shown in Figure 2.1 below.

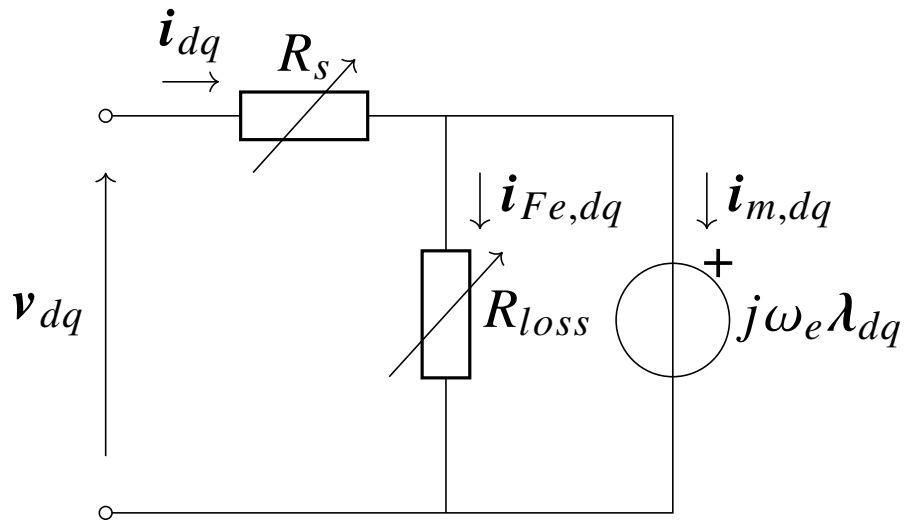

Figure 2.1: Steady-state equivalent circuital model of the machine.

Hence, the stator current ($\boldsymbol{i}_{dq}$) is based on the sum of a magnetizing one ($\boldsymbol{i}_{m,dq}$) and a loss one ($\boldsymbol{i}_{Fe,dq}$).
Typically, the first source of loss is due to the ohmic resistance of the stator (R_s). Such resistance depends on the temperature of the conducting material and on the frequency of the electrical source. Being modeled as a variable resistance, the copper losses are computed using the Joule's law:

$$p_j(i_d, i_q, f, T) = \frac{3}{2} \cdot Rs \cdot I_s^2 = \frac{3}{2} \cdot R_{dc} \cdot k_\theta \cdot k_{AC} \cdot I_s^2 \tag{7}$$

where R_{dc} is the nominal resistance at the nominal temperature T_{Cu}, k_θ is the temperature coefficient and k_{AC} represents the skin effect. The factor $\frac{3}{2}$ is inherited from the non-power invariance of the Clarke transformation.

Iron and permanent magnet losses represent other major loss components. These are due to the cycle of magnetization and demagnetization of the ferromagnetic material subject to a rotating magnetic field and to the eddy currents that are induced by a varying magnetic flux.
In the end, these losses are evaluated using a modified version of the Steinmetz's equation, mapped over the magnetizing current grid $\mathbf{I}_{m,dq}$ at the nominal frequency f_0:

$$\begin{aligned} p_{losses}(i_{md}, i_{mq}, f0) = p_h(i_{md}, i_{mq}, f0) + p_e(i_{md}, i_{mq}, f0) = \\ = C_h \cdot f_0^{\alpha} \cdot B_m^{\beta}(i_{md},i_{mq}) + C_e \cdot f_0^2 \cdot B_m^2(i_{md}, i_{mq}) \end{aligned} \tag{8}$$

where the unknown coefficients α, β, C_h and C_e are typically obtained through a data fitting process starting from the manufacturer's data-sheet.

Both the stator and the rotor core are made of ferromagnetic material, hence both are subject to such leakages. Permanent magnets are as well made of ferromagnetic material, but in first approximation they are subject only to eddy currents.
The loss maps at nominal frequency are taken for granted here, where they are just rescaled based on the working frequency (Eq.9).

$$\begin{aligned} \mathbf{P}_{Iron}(f) = \mathbf{P}_h(f0) \cdot \left(\frac{f}{f_0}\right)^{\alpha} + \mathbf{P}_e(f0) \cdot \left(\frac{f}{f_0}\right)^2 \\ \mathbf{P}_{PM}(f) = \mathbf{P}_{PM}(f0) \cdot \left(\frac{f}{f_0}\right)^2, \end{aligned} \tag{9}$$

For the modelling point of view, the effect of such losses can be modelled as an additional dissipative branch with resistance R_{loss} as shown in Figure 2.1 and discussed below in Section 2.2.3.
PWM supply, spatial harmonics, mechanical and other minor losses are neglected.

2.2 Matlab maps extrapolation

Typically and hopefully, the control designer receives by the machine designer a bunch of machine data FEA-evaluated or experimentally determined.
Among these, the ones available here are:

- $\mathbf{I}_{m,dq}$ grid and the corresponding $\mathbf{\Lambda}_{dq}$(Steady-state Flux maps averaged over a mechanical round)
- $\mathbf{I}_{m,dq}$ grid and the corresponding $\mathbf{P}_{Iron0}$ and $\mathbf{P}_{PM0}$(Losses maps at a reference frequency)
- **fT** (frequency,temperature) grid and the corresponding $\mathbf{K}_{AC}$ (AC copper coefficient)

In order to manipulate all these motor data and to elaborate all the relevant maps that will be exploited in the following Simulink and Plecs models, Matlab is used.

2.2.1 Four quadrants extension of maps

As just said, many machine data are typically collected in a grid/matrix form (e.g. $128X128$,$255X255$...). Referring in particular to $\mathbf{I}_{m,dq}, \mathbf{\Lambda}_{dq}, \mathbf{P}_{Iron0}$ and $\mathbf{P}_{PM0}$, these can be found usually for the first 2 quadrants of the dq plane (only positive q-axis currents). The reason is that the III and IV quadrants' data can be easily obtained from symmetry considerations.

Talking about λ_d, the cross-saturation effect due to the i_q current depends on the magnitude and not by its sign, therefore λ_d exhibits a symmetry with respect to the d-axis. Concerning λ_q instead, the effect of a negative i_q is opposite with respect to the positive counterpart, with λ_q which shows a symmetry with respect to the origin. Similarly to the λ_d case, the effect of positive or negative i_q current on the losses is the same since these last ones depends on the magnitude of the current and not on its sign.

Summing up:

- $\mathbf{I}_{md}[III, IV] = \mathbf{I}_{md}[II, I]$
- $\mathbf{I}_{mq}[III, IV] = -\mathbf{I}_{mq}[II, I]$
- $\mathbf{\Lambda}_{d}[III, IV] = \mathbf{\Lambda}_{d}[II, I]$
- $\mathbf{\Lambda}_{q}[III, IV] = -\mathbf{\Lambda}_{q}[II, I]$

- $\mathbf{P}_{PM}[III, IV] = \mathbf{P}_{PM}[II, I]$
- $\mathbf{P}_{Iron}[III, IV] = \mathbf{P}_{Iron}[II, I]$

2.2.2 Direct and Inverse flux-linkage maps

The first step in modelling any three-phase electric motor is the construction of its flux maps. Such maps represent the passage from currents to fluxes $(\lambda_d(i_{md}, i_{mq}), \lambda_q(i_{md}, i_{mq}))$, so for each couple of currents in the dq axes the corresponding fluxes in dq axes are associated.

Typically, as in this case, the FEA-evaluated steady-state flux-linkage maps are reported over the magnetizing component of the current ($\boldsymbol{i}_{m,dq}$ in Fig.2.1), while in a typical experimental extrapolation of these latter (as in Section 5.1) they are expressed as function of the total stator current ($\boldsymbol{i}_{dq}$ in Fig.2.1).

Another characteristic of the software-based extrapolation is the possibility to have a perfectly regular current grid domain, which makes the data easy to handle.
The given flux-linkage maps of the considered IPM machine are plotted in Fig.2.2.

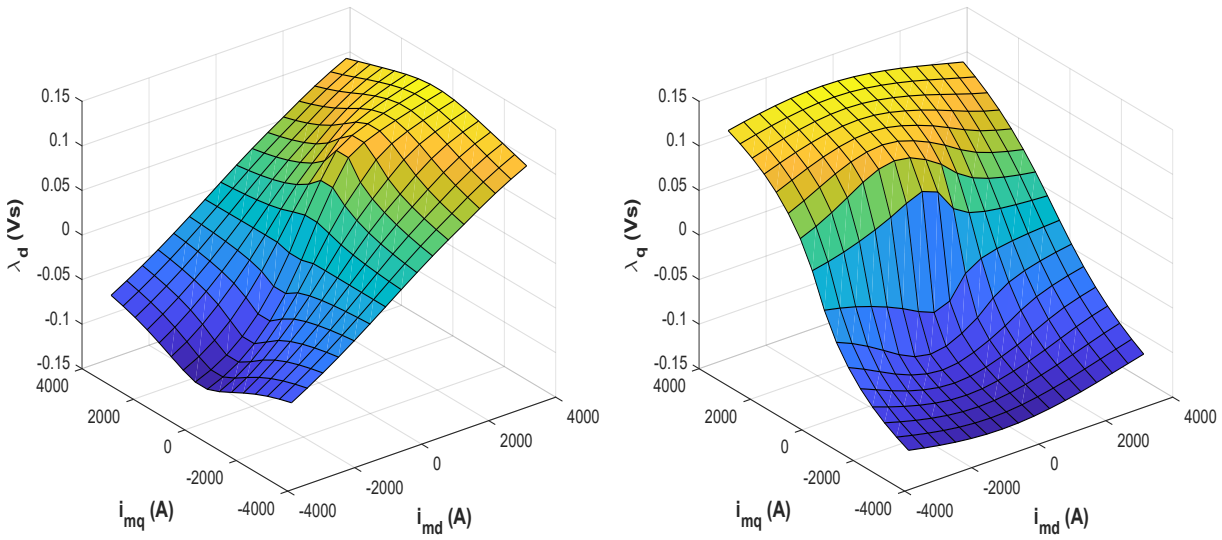

Figure 2.2: Flux maps in the $\mathbf{I}_{m,dq}$ plane.

The next point is to build the inverse relation and hence to pass from fluxes to currents ($i_{md}(\lambda_d, \lambda_q), i_{mq}(\lambda_d, \lambda_q)$).
Although it may seem the only counterpart of the above one, it actually hides the problem that the fluxes are in a non-regular domain, making the interpolation a bit more tedious. Nevertheless, Matlab has a proper command (*scatteredInterpolant*), which solves the issue and after the definition of two interpolant objects based on the initial data, provides the dq currents associated to a regularized dq flux linkage domain (Fig.2.3) .

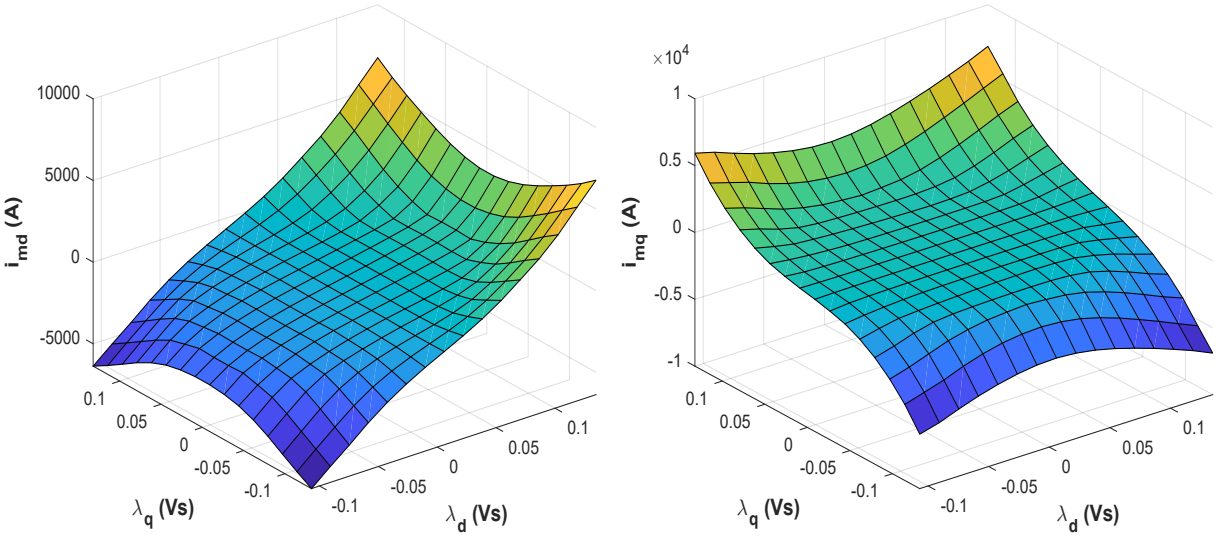

Figure 2.3: Inverse Flux maps in the $\mathbf{\Lambda}_{dq}$ plane.

2.2.3 Machine losses

Starting from the Equation (7) it is necessary to find the gains ($\mathbf{K}_\theta$ and $\mathbf{K}_{AC}$) that account for the temperature and frequency effects.
The skin coefficients $\mathbf{K}_{AC}$ are given for a a grid of frequency and temperature, while the temperature ones $\boldsymbol{k}_\theta$ are computed through the formula: $k_\theta = \frac{Ts+234.5}{Ts_{ref}+234.5}$ for all the stator temperatures in the **fT** grid. Then replicating the $\boldsymbol{k}_\theta$ vector for all the frequencies in the in the **fT** grid, the $\mathbf{K}_\theta$ matrix is built over the same domain of $\mathbf{K}_{AC}$. Finally,doing the element-wise product of these two matrices and multiplying the result for the nominal stator resistance R_{s0}, a 2-dimensional stator resistance map is formed .

$$\mathbf{R}_s = R_{s0} \cdot \mathbf{K}_\theta \circ \mathbf{K}_{AC} \tag{10}$$

As soon as this latter is evaluated based on the operating point(f,T), the Joule's law is applied and the dissipated power for each value of current $\boldsymbol{i}_{dq}$ can be computed as done in Equation (7).

Concerning the iron and PM losses, the leakage power is given for the grid of dq magnetizing currents at the nominal frequency f_0. Then, these values are rescaled over a range of frequencies as discussed in Section 2.1.3 (3-dimensional object is obtained) and eventually extended to the four quadrants as explained in Section 2.2.1.
From the obtained dissipated power map, the resistance of the dissipative iron-PM branch is computed (Joule's law) and then the leakage current magnitude can be computed.

$$\begin{aligned} \mathbf{R}_{loss} &= \frac{3}{2} \cdot \mathbf{V}^2 \oslash \mathbf{P}_{loss} = \frac{3}{2} \cdot (\omega_e \cdot \mathbf{\Lambda}_{dq})^2 \oslash \mathbf{P}_{loss} \\ \mathbf{I}_{loss} &= |\mathbf{V}| \oslash \mathbf{R}_{loss} = \frac{2}{3} \cdot \mathbf{P}_{loss} \oslash (|\omega_e| \cdot \mathbf{\Lambda}_{dq}) \end{aligned} \tag{11}$$

The $\mathbf{I}_{loss}$ values for each operating point(i_{md}, i_{mq}, f) are stored in a 3-dimensional map and together with the stator resistance 2-dimensional map (Eq.10) will be used later in Section 2.3.3 to define two Simulink LUTs.
In the end, the hysteresis and the eddy currents losses increase with the frequency (Eq.9) and therefore increasing the speed means increasing the discrepancy between the stator current $\boldsymbol{i}_{dq}$ and the magnetizing one $\boldsymbol{i}_{m,dq}$, as highlighted in Equation (11).

2.2.4 Differential inductances

Considering the dq electrical model in Equation(4), it is clear the need of computing the flux linkage time derivative $\frac{d\boldsymbol{\lambda}_{dq}}{dt}$.
Expressing such flux by means of Equation (6), the expression (12) is obtained.

$$\frac{d\boldsymbol{\lambda}_{dq}}{dt} = \frac{d\mathbf{L}_{dq}}{dt} \cdot \boldsymbol{i}_{dq} + \mathbf{L}_{dq} \cdot \frac{d\boldsymbol{i}_{dq}}{dt} + \frac{d\lambda_m}{dt} \tag{12}$$

The first term ($\frac{d\mathbf{L}_{dq}}{dt}$) results very hard to be computed and therefore the following approximation is considered to circumvent the problem:

$$\begin{aligned} \frac{d\boldsymbol{\lambda}_{dq}}{dt} &= \frac{d\boldsymbol{\lambda}_{dq}}{d\boldsymbol{i}_{m,dq}} \cdot \frac{d\boldsymbol{i}_{m,dq}}{dt} \qquad \text{,where} \\ \frac{d\boldsymbol{\lambda}_{dq}}{d\boldsymbol{i}_{m,dq}} &= \frac{\partial(\lambda_d, \lambda_q)}{\partial(i_{md}, i_{mq})} = \begin{bmatrix} l_{dd} & l_{dq} \\ l_{dq} & l_{qq} \end{bmatrix} \end{aligned} \tag{13}$$

Each of the two rows of the differential inductances matrix $[l_{dq}]$ is computed through the command *gradient* where the current steps are computed as the difference between any two consecutive elements of the vectors of i_{md} and i_{mq} currents since the current domain is regular here. Also in this case, the four quadrants extension (2.2.1) of the dq fluxes can be applied to have the differential inductances for the entire dq magnetizing current plane as shown in Figure 2.4.

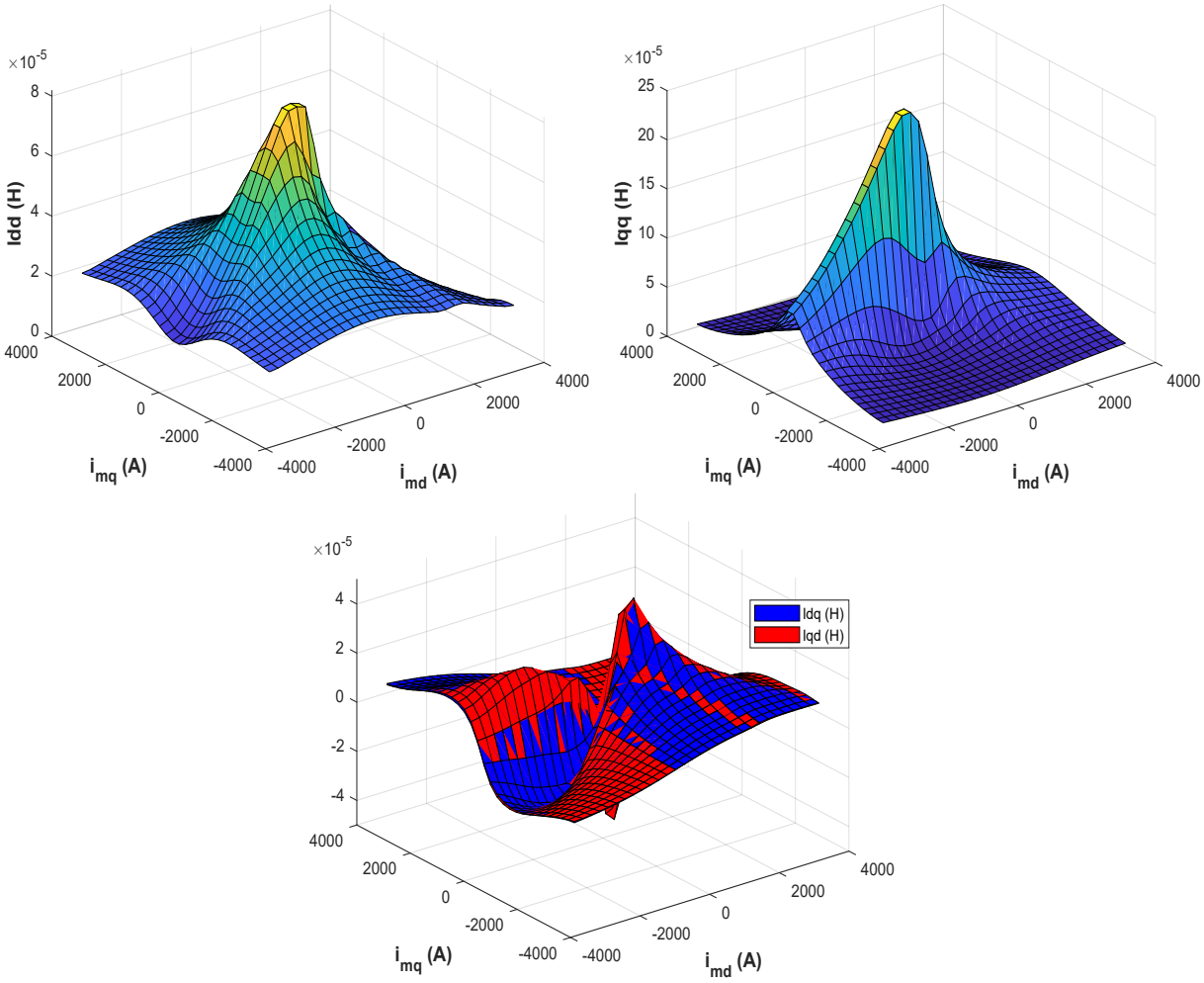

Figure 2.4: Differential inductances maps in the $\mathbf{I}_{m,dq}$ plane.

2.2.5 Torque maps,MTPA and MTPV

According to Equation(1)) and exploiting the flux-linkage maps (Section 2.2.2), it is possible to get the torque maps for each combination of $\boldsymbol{\lambda}_{dq}$ and $\boldsymbol{i}_{m,dq}$ as shown in Figure 2.5.

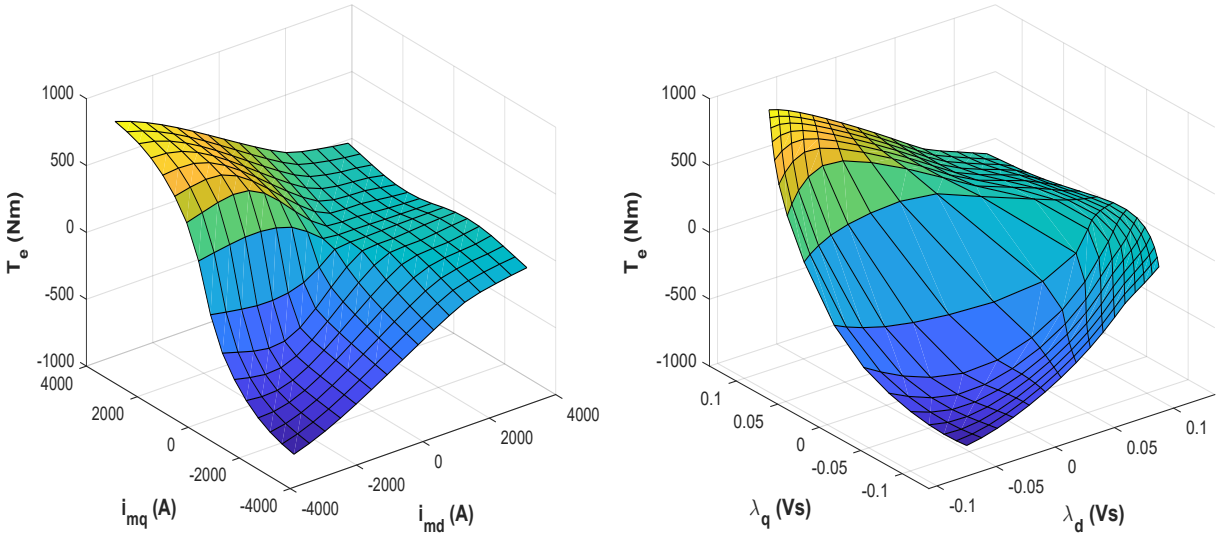

Figure 2.5: Torque maps in the $\mathbf{I}_{m,dq}$ plane.

Ideally, the torque request can go up to the mechanical constraints. However, typically way before such boundaries, the current limit appears, preventing the overheating of the machine. The minimum between the inverter current capability and the machine one defines such limitation. In this context, there is the need to maximize the torque production at the stator current peak value and in general, for each stator current magnitude, minimizing the Joule losses and hence the heat to be dissipated.

The maximum torque per ampere profile (MTPA) does the job and among all the $\boldsymbol{i}_{dq}$ combinations for each torque level, listed with the command *countourc*, it identifies the one with the minimum magnitude. Then, linking all the optimal points on the dq current plane, the MTPA trajectory is drawn and eventually reconstructed on dq flux-linkage plane exploiting the flux-linkage maps.

However, all the maps provided are evaluated over a magnetizing currents domain and not over a stator currents one. For this reason, assuming that the speed at which the flux-linkage maps were evaluated was low enough to consider iron losses negligible, the approximation $\boldsymbol{i}_{dq} \approx \boldsymbol{i}_{m,dq}$ is made in the Matlab script.

Another constraint is introduced by the inverter and it is the voltage one. For reasons that will be described in Chapter 3, such limit imposed a maximum voltage magnitude of $\frac{v_{dc}}{\sqrt{3}}$. Therefore, another intent is to maximize the torque for a given value of voltage or flux linkage, since this latter is strictly related to the former ($|\boldsymbol{v}_{dq}| \simeq \omega_e |\boldsymbol{\lambda}_{dq}|$) due to the simplified steady-state expression of Equation (4).

The maximum torque per voltage profile (MTPV) does the job and for each values of torque provides the $\boldsymbol{\lambda}_{dq}$ combination with the lowest magnitude. Conversely to the MTPA case, exploiting the inverse flux-linkage maps the MTPV profile can also be reconstructed on the dq current plane, always assuming $\boldsymbol{i}_{dq} \approx \boldsymbol{i}_{m,dq}$.

With the intent of plotting the current limit in the current plane and an arbitrarily chosen voltage/flux-linkage limit (DC voltage and speed dependent) in the flux-linkage plane, the following expressions are considered:

$$\begin{gathered} i_d^2 + i_q^2 \leq I_{max}^2, \text{with} I_{max} = 1403.8\text{A} \\ v_d^2 + v_q^2 \simeq (-\omega_e \lambda_q)^2 + (\omega_e \lambda_d)^2 \leq V_{max}^2 \rightarrow \lambda_q^2 + \lambda_d^2 \leq \left(\frac{V_{max}}{\omega_e}\right)^2, \\ \text{with } V_{max} = \frac{v_{dc0}}{\sqrt{3}} = 132.8 \text{ V and } \omega_e = \frac{n0 \cdot pp \cdot 2\pi}{60} = 1256.6\text{rad/s} \end{gathered} \tag{14}$$

The current limit is the one of the machine, the flux-linkage limit is instead imposed by the inverter, supplied with the nominal DC voltage $v_{dc0} = 230$ V and considering a mechanical speed of $n_0 = 4000$ rpm.

In addition, the torque maps are flattened on the bidimensional dq current and flux-linkage plane as isotorque lines with the command *contourf*.

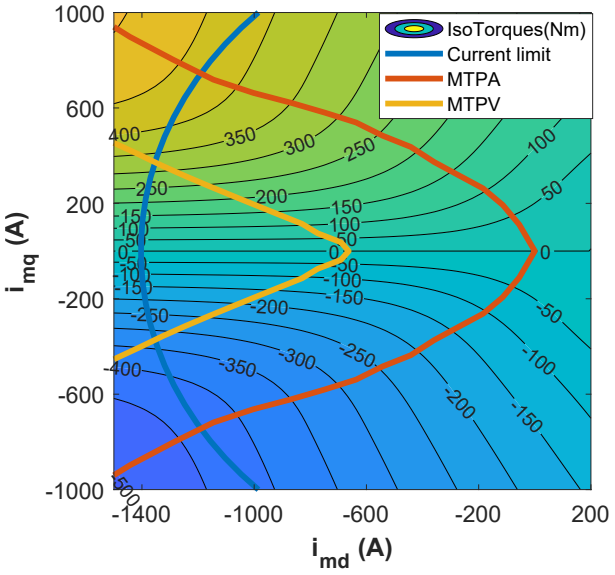

Figure 2.6: IsoTorques,current limit,MTPA,MTPV in the $\mathbf{I}_{dq}$ plane.

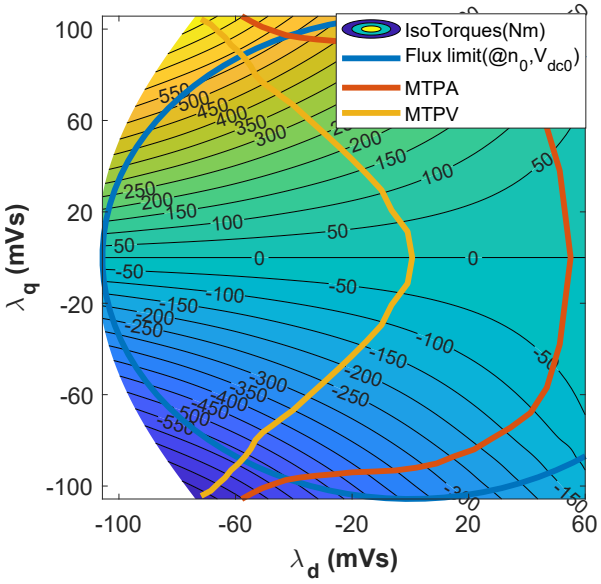

Figure 2.7: IsoTorques,flux limit, MTPA, and MTPV in the $\mathbf{\Lambda}_{dq}$ plane.

The characteristic current I_0 is defined as the current on the d-axis capable of cancelling the flux magnitude, possibly driving the machine to infinite speed except for mechanical constraints. It can be defined analytically from the d-axis expression in Equation (6) as:

$$I_0 = -\frac{\lambda_m(i_q = 0)}{L_d(i_q = 0, i_d = I_0)} \tag{15}$$

However, since I_0 appears on both sides of the equation, a numerical solution is needed. Alternatively, looking at the MTPV dq current associated with zero torque, I_0 is obtained. Indeed, this point is associated with the minimum flux-linkage for zero torque in the dq flux-linkage plane, which is very close to the definition of characteristic current.

2.2.6 MTPS and Efficiency maps

Another way to observe the effect of the current and voltage constraints (Section 2.2.5) is to build the maximum/minimum torque per speed profiles (MTPS). Essentially, looking for the highest/lowest torque at each speed means looking for the maximum performance of the machine at each speed both in motoring and in generation.

The starting point to compute these two profiles is the Figure 2.1. Exploiting the flux-linkage maps (Section 2.2.2) first the active and reactive power of the rightmost branch P_E and Q_E are obtained:

$$\begin{bmatrix} \mathbf{P}_E \\ \mathbf{Q}_E \end{bmatrix} = \frac{3}{2} \begin{bmatrix} -\omega_e \lambda_q & \omega_e \lambda_d \\ \omega_e \lambda_d & \omega_e \lambda_q \end{bmatrix} \begin{bmatrix} \mathbf{I}_{md} \\ \mathbf{I}_{mq} \end{bmatrix} \tag{16}$$

Then summing the iron losses active power P_{Iron}, it is possible to obtain the electrical power of the right side P_S and Q_S. Hence, reversing the Equation (17), the stator currents $\mathbf{I}_{dq}$ are computed for each value of speed and magnetizing current in the $\mathbf{I}_{m,dq}$ grid (Eq.18).

$$\begin{bmatrix} \mathbf{P}_S \\ \mathbf{Q}_S \end{bmatrix} = \frac{3}{2} \begin{bmatrix} -\omega_e \lambda_q & \omega_e \lambda_d \\ \omega_e \lambda_d & \omega_e \lambda_q \end{bmatrix} \begin{bmatrix} \mathbf{I}_d \\ \mathbf{I}_q \end{bmatrix} \tag{17}$$

The factor $\frac{3}{2}$ in Equations (16) and (17) is inherited from the non-power invariance of the Clarke transformation considered.

$$\begin{bmatrix} \mathbf{I}_d \\ \mathbf{I}_q \end{bmatrix} = \frac{2}{3} \cdot \frac{1}{\left(-\omega_e^2 \lambda_q^2 - \omega_e^2 \lambda_d^2\right)} \begin{bmatrix} \omega_e \lambda_q & -\omega_e \lambda_d \\ -\omega_e \lambda_d & -\omega_e \lambda_q \end{bmatrix} \begin{bmatrix} \mathbf{P}_S \\ \mathbf{Q}_S \end{bmatrix} \tag{18}$$

In addition, for each speed, computed the stator current matrices $\mathbf{I}_d$ and $\mathbf{I}_q$, exploiting the steady-state expression of Equation 4, considering the stator resistance at the investigated speed and at the nominal stator temperature T_{cu} (Section 2.2.3), the overall stator voltage matrices $\mathbf{V}_d$ and $\mathbf{V}_q$ are obtained. In the end, among all the stator currents and voltages, the discard of those which not satisfy the current and voltage limitations, provides a restricted group of corresponding magnetizing currents among which the maximum and minimum effective electromagnetic torques are computed.

With the intent later of testing the machine in an MTPS point (Section 3.6), hence to get the reference dq currents based on the speed, the original voltage limit $V_{max} = \frac{v_{dc0}}{\sqrt{3}}$ is multiplied by a 0.9 factor accounting for the steady-state approximation adopted in the computation of the stator dq voltages.

The total active electrical power and the mechanical power along the MTPS profiles are computed (Eq.19), assuming the mechanical torque Tm equal to the electromagnetic one Te since the mechanical losses are not considered and computing the electromagnetic torque from the magnetizing dq currents.

$$\begin{aligned} Pe_{MTPS} &= \frac{3}{2} \cdot (v_{d,MTPS} \cdot i_{d,MTPS} + v_{q,MTPS} \cdot i_{q,MTPS}) \\ Pm_{MTPS} &= Tm_{MTPS} \cdot \omega_{m,MTPS} \end{aligned} \tag{19}$$

Then, for the efficiency computation, four main cases are identified:

- mechanical power > 0 and electrical power ≤ 0 –>not feasible case –>$\eta = NaN$
- mechanical power ≤ 0 and electrical power > 0 –>power dissipator –>$\eta = 0$
- mechanical power < 0 and electrical power ≤ 0 –>generator–>$\eta = \frac{P_e}{P_m}$
- mechanical power≥ 0 and electrical power > 0 –>motor–>$\eta = \frac{P_m}{P_e}$

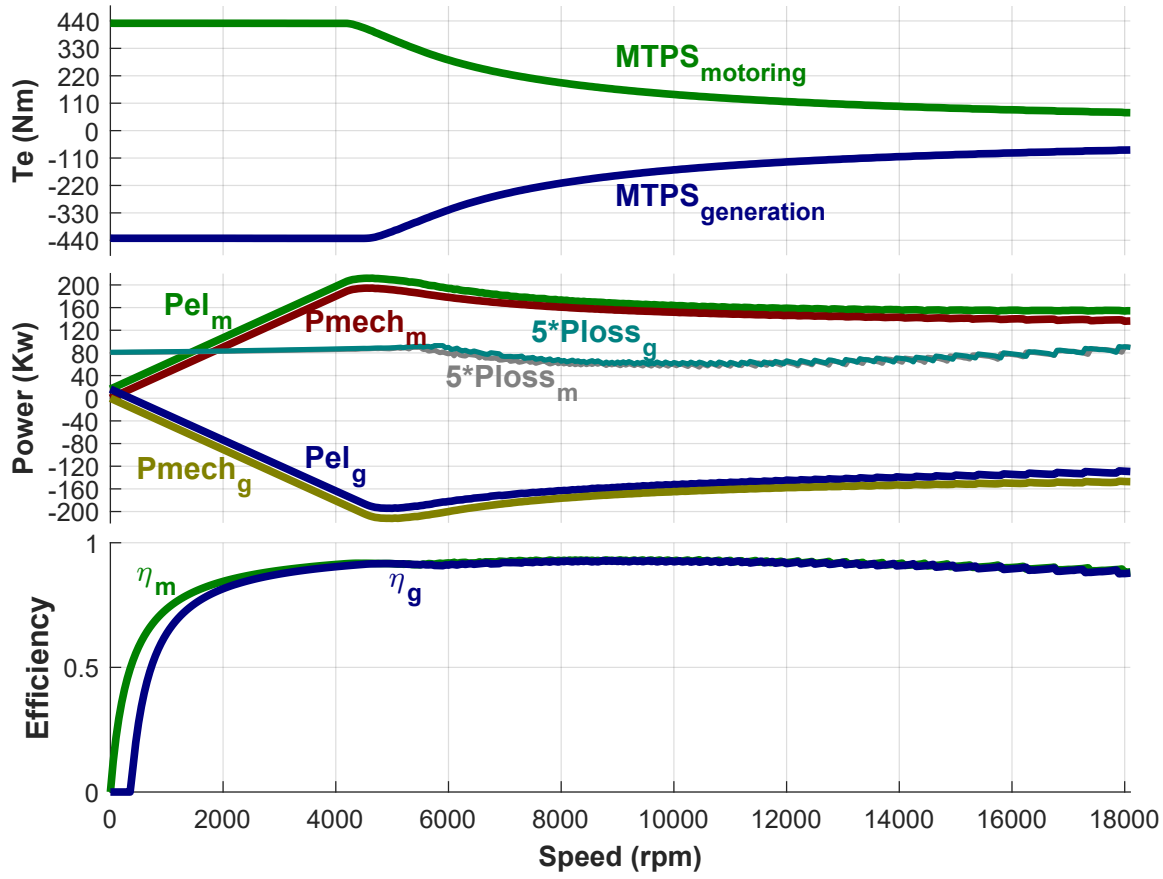

Figure 2.8: Torque,Power and Efficiency in MTPS.

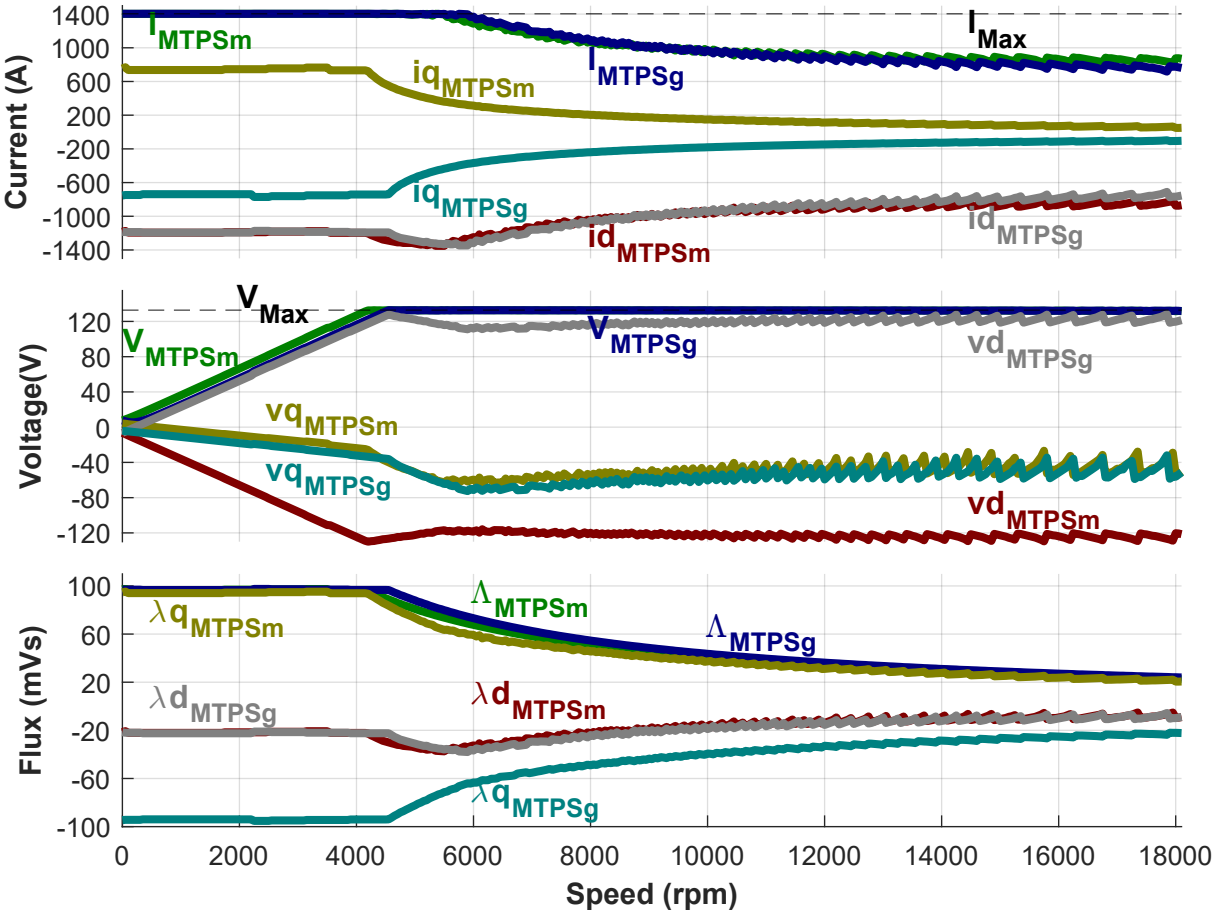

Figure 2.9: Current,Voltage and Flux in MTPS.

It is relevant to note that the electrical power is greater than zero for a narrow band of rpm close to the zero speed (Figure 2.8), where the mechanical power is close to zero. The reason is that in these occasions, the Joule losses are extremely high due to the extremely high current/torque request and therefore also in generation where this amount of power cannot come from the mechanical side due to the low speed, electrical power have to be injected to guarantee the power balance of the system. As a consequence $\eta_g = \frac{P_e}{P_m} = 0$ at low speed (Figure 2.8).

Another consideration regards the base speed, i.e. the speed that can be reached with maximum flux-linkage magnitude before the voltage limit appears. The two profiles results to be asymmetric in this sense, with the generation base speed higher with respect to the motoring one. The reason is that in generation the stator resistance helps decreasing the stator voltage, allowing a wider speed range before the flux weakening region starts.

A further step consists in building the so-called efficiency map and all the associated maps. The idea is to define a meshgrid of speed,torque operating points and for each of them find the best stator current or voltage according to a certain optimization criterion, among the ones that satisfy the usual current and voltage constraints (Section 2.2.5), finally computing the efficiency.

The most adopted criterion here is the one that looks for the minimum current magnitude. The computation with Matlab of these maps starts from the MPTS script where instead of scanning all the grid of $\mathbf{I}_{m,dq}$ currents, the focus is on the ones which are associated with the considered torque ,exploiting the *contourc* command in a similar fashion to what is done for the MTPA and the MTPV profiles.

With the intent later of using the results to determine the reference dq currents based on the speed and torque operating conditions in the current vector control (Section 4.4.1), the voltage limit is set as $V_{max} = 0.9\frac{v_{dc0}}{\sqrt{3}}$, accounting for the steady-state approximation adopted in the computation of the stator dq voltages.

As done with the MTPS profiles extrapolation, electrical and mechanical power are computed with Equation (19), assuming no mechanical losses and computing the electromagnetic torque from the magnetizing dq currents, hence $T_m = T_e$.

Before the flux weakening region starts, the optimal currents $\mathbf{I}_{dq}$ follow the MTPA profile. This is evident from Figure 2.12 where the phase of $\mathbf{I}_{dq}$ moves in the II and III quadrant for speeds below the base one with angles that resemble the MTPA trajectory (Figure 2.6). Once the voltage constraint appears, the current phase is rotated towards the -180° angle, forcing the i_d current against the magnets action, reducing the flux linkage, and allowing the achievement of an higher speed.
The efficiency is very high (Figure 2.14) apart from regions characterized by very low speed and high absolute value torque (electrical power has to compensate joule losses) and other ones where the mechanical power tends to zero (Torque,speed or both close to zero) and hence the efficiency is not defined or is zero.
The power factor shows good values as well (Figure 2.15), resulting in an efficient exploitation of the energy.

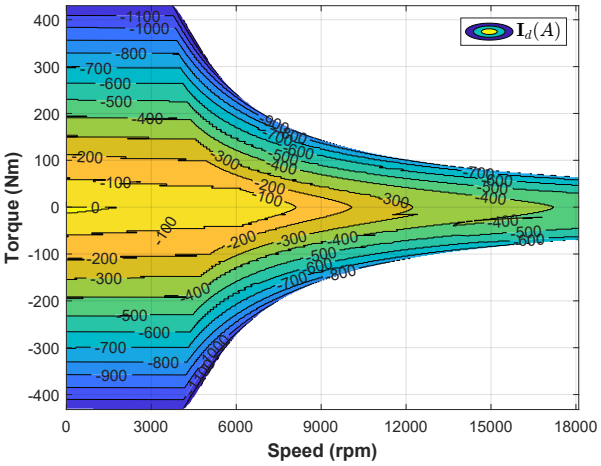

Figure 2.10: $\mathbf{I}_d$ map in the Torque,Speed plane.

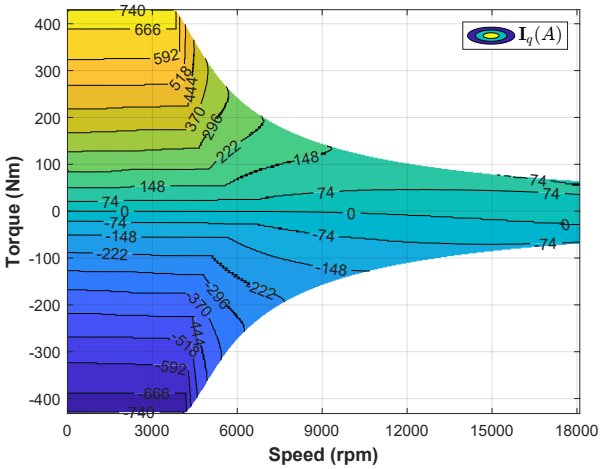

Figure 2.11: $\mathbf{I}_q$ map in the Torque,Speed plane.

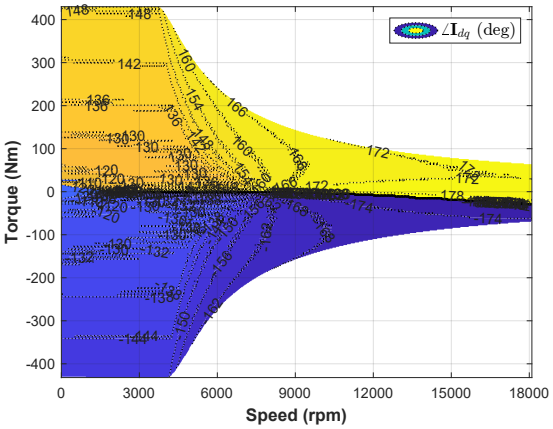

Figure 2.12: $\mathbf{I}_{dq}$ phase map in the Torque,Speed plane.

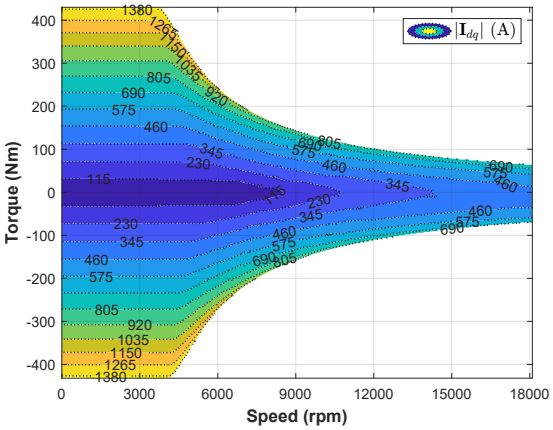

Figure 2.13: $\mathbf{I}_{dq}$ magnitude map in the Torque,Speed plane.

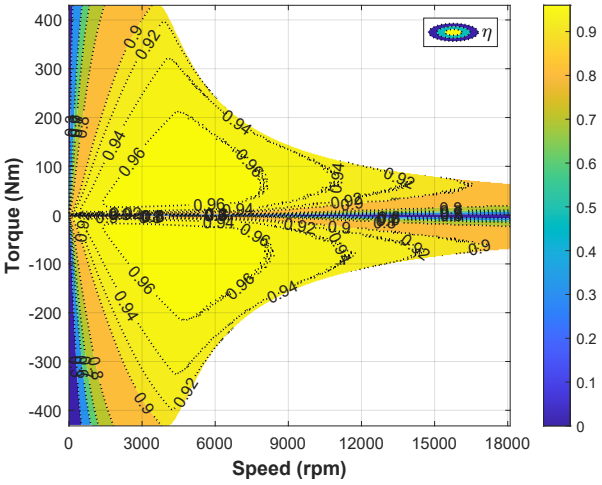

Figure 2.14: Efficiency map in the Torque,Speed plane.

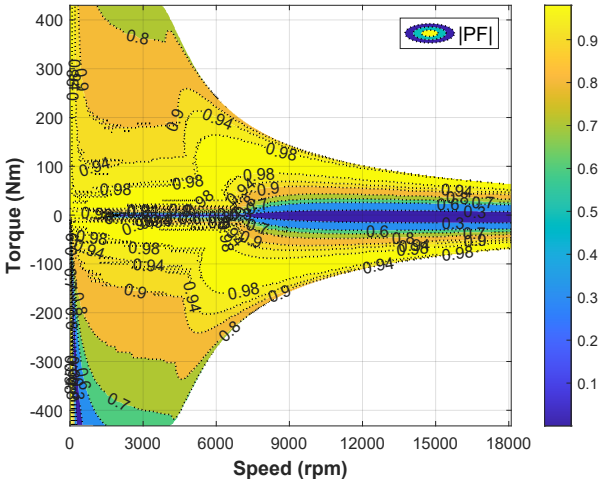

Figure 2.15: PF absolute value map in the Torque,Speed plane.

2.3 Simulink machine models

In Simulink, the modelling of the machine is done using blocks. These blocks do nothing but solve the equation that characterizes the machine in the different domains.

Starting from the mechanical speed, the mechanical and the electrical angles (θ_m and θ_d) are reconstructed in a normalized form ($[-\pi, \pi]$).
At this point, the applied abc voltages can be converted in dq ones using the Park transformation (A.5) and the dq voltage equations (Eq.4) are built isolating the derivative component $\frac{d}{dt}\begin{bmatrix}\lambda_d \\ \lambda_q\end{bmatrix}$.

There are now two possible approaches: the flux-based dq model or the current-based dq model.

2.3.1 Flux-based dq model

In the flux-based model the derivative component $\frac{d}{dt}\begin{bmatrix}\lambda_d \\ \lambda_q\end{bmatrix}$, once it is isolated after the application of the dq voltages, it is integrated imposing as an initial conditions $\lambda_d = \lambda_{m0}$ and $\lambda_q = 0$. Finally, the dq currents are evaluated through the use of the inverse flux maps (Section 2.2.2).

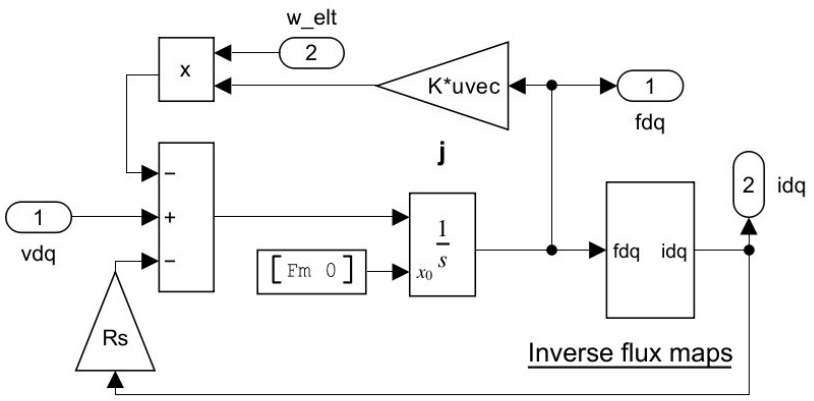

Figure 2.16: Flux-based dq model.

2.3.2 Current-based dq model

Adopting a current-based approach means that the dq flux-linkage derivative is expressed by the use of the Equation (13). Hence, the time derivative is multiplied by the inverse of the differential inductances matrix and the result is integrated to get the dq currents. This approach can show problem in convergence due to the high values that are caused by the inversion of a matrix with very small entries like the differential inductances $l_{dd}, l_{dq}, l_{qd}, l_{qq}$.

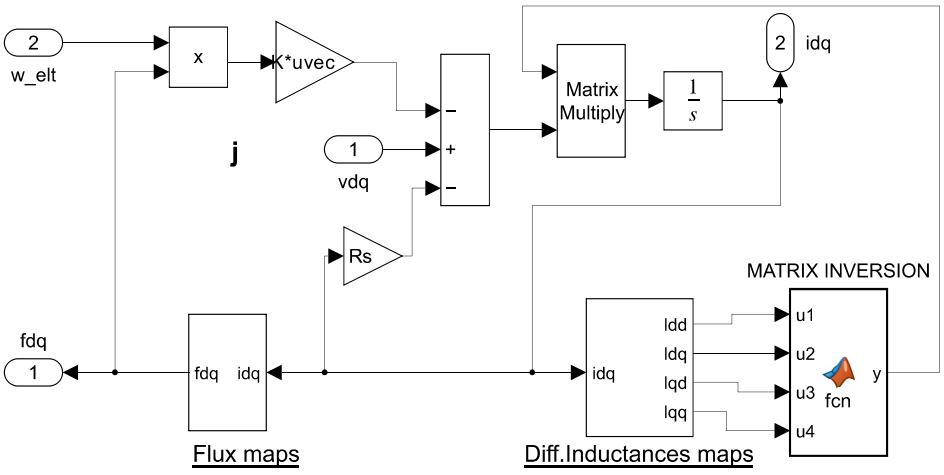

Figure 2.17: Current-based dq model.

2.3.3 dq models with machine losses

As already described in Sections 2.1.3 and 2.2.3, the loss phenomena considered here are:

- The Joule losses (including the stator resistance variation due to temperature and frequency)
- The iron losses (due to hysteresis and eddy currents)
- The permanent magnets losses (due to eddy currents)

In order to account for such phenomena in the models, the starting point is again Figure 2.1. The idea is to get the total stator current i_{dq}, summing to the magnetizing one $i_{m,dq}$ (related to λ_{dq}), the additional one $i_{Fe,dq}$ due to the iron and PM losses.

First the dissipative current magnitude I_{loss} is computed thanks to a 3-dimensional LUT (Section 2.2.3) and then considering the load angle δ, the dq components are obtained as:

$$\boldsymbol{i}_{Fe,dq} = -I_{loss} \cdot sign(\omega_e) \cdot \sin\delta + jI_{loss} \cdot sign(\omega_e) \cdot \cos\delta \tag{20}$$

The stator resistance is online updated with a 2-dimensional LUT (Section 2.2.3) and the voltage drop over this latter is computed.
In Figures 2.18 and 2.19 below, both the approaches are shown updated to include the losses and the stator resistance variation.

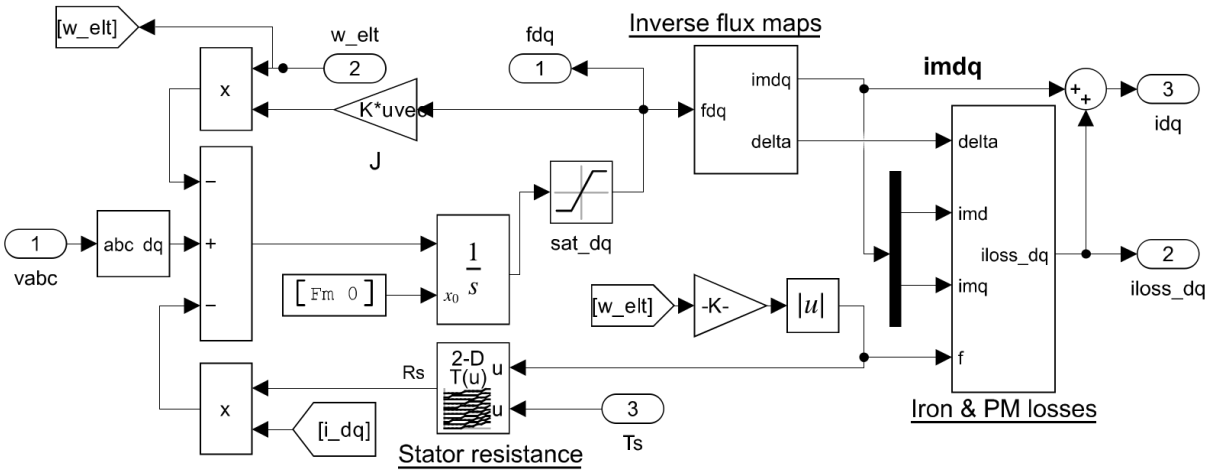

Figure 2.18: Flux-based dq model including losses.

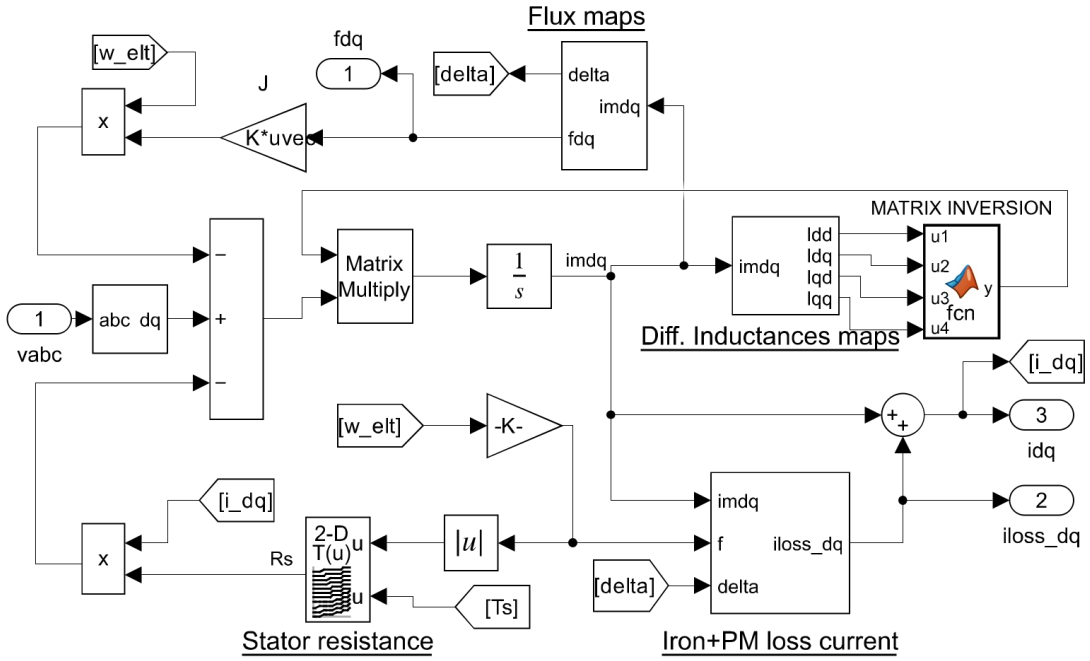

Figure 2.19: Current-based dq model including losses.

2.4 Plecs machine models

Plecs is a simulation software designed specifically for modelling and simulating power electronic systems and electrical drives. It allows the user to build the electrical circuits directly with electrical components. However, most of the time Simulink-style blocks together with C-script blocks are used to perform math operations, leaving the electrical circuit the only task to simulate the electrical behaviour of the motor.

2.4.1 Current-controlled generators model

One possible model adopts two current-controlled generators where the two imposed currents (i_a, i_c) are derived from two measured line to line voltages (v_{ab},v_{bc}). The only passage that deserves attention here is the Clarke transformation where instead of the usual phase voltages the adoption of the line to line ones involves a simple rearrangement of the Clarke matrix as shown in Equation (21).

$$\begin{bmatrix} v_\alpha \\ v_\beta \end{bmatrix} = \frac{2}{3} \begin{bmatrix} \frac{1}{2} & 0 & \frac{1}{2} \\ 0 & \frac{\sqrt{3}}{2} & 0 \end{bmatrix} \begin{bmatrix} v_{ab} \\ v_{bc} \\ v_{ac} \end{bmatrix} \tag{21}$$

Then operating the rotation (A.3) to get the dq voltages, computing the dq currents as done in the flux-based dq model with losses (Section 2.3.3) and finally operating the inverse Park transformation (A.6), the imposed i_a and i_c currents are retrieved. Essentially, it is a flux-based dq model with the addition of the direct and inverse Park transformations and a simple electrical circuit.

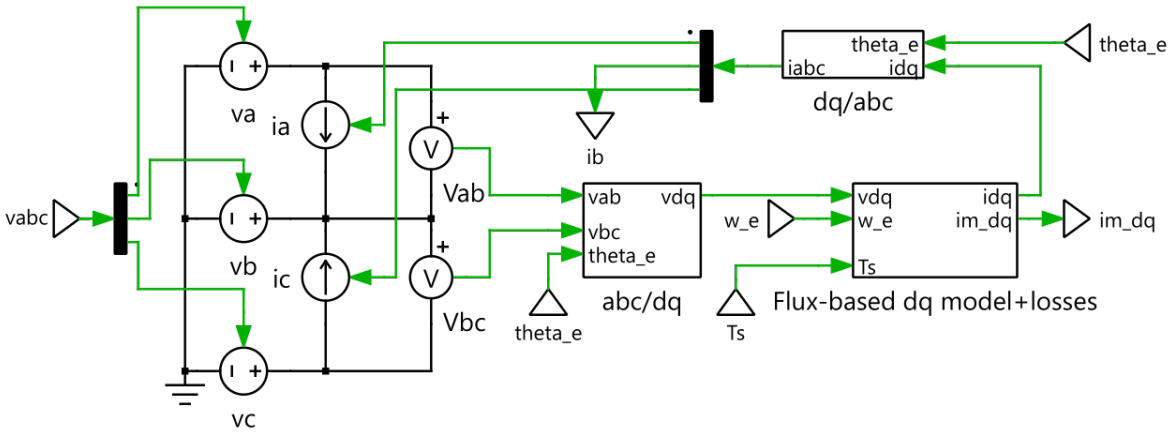

Figure 2.20: Current-controlled generators model including losses.

2.4.2 Voltage behind reactance model

The VBR model represents a totally different approach. In such a model, there is the intent to consider the electrical circuits characterizing the three-phase machine. Combining Equations (3) and (5), and assuming constant leakage phase inductance and magnets flux, the following expression in matrix form is obtained:

$$\begin{bmatrix} v_a \\ v_b \\ v_c \end{bmatrix} = \underbrace{R_s \begin{bmatrix} i_a \\ i_b \\ i_c \end{bmatrix}}_{\text{R}} + \underbrace{L_{ls}\frac{d}{dt}\begin{bmatrix} i_a \\ i_b \\ i_c \end{bmatrix} + \mathbf{M}\frac{d}{dt}\begin{bmatrix} i_a \\ i_b \\ i_c \end{bmatrix}}_{\text{L (inductive EMF)}} + \underbrace{\frac{d\mathbf{M}}{dt}\begin{bmatrix} i_a \\ i_b \\ i_c \end{bmatrix} + \lambda_{m0}\frac{d}{dt}\begin{bmatrix} \cos(\theta) \\ \cos(\theta - \frac{2}{3}\pi) \\ \cos(\theta + \frac{2}{3}\pi) \end{bmatrix}}_{\text{E (motional EMF)}} \quad (22)$$

where $\mathbf{M}$ is the matrix of magnetizing inductances.

In the end, each phase can be modeled as an RLE branch,with the R modelling the stator ohmic resistance, the L modelling the contribution of the leakage,self and mutual inductances and the E modelling the motional EMF due to the motion of the rotor. The problem is that the magnetizing inductances depends on the rotor position through the angle 2θ, hence they are not easy to be treated directly.

The idea here is to start from the dq voltage equations (Eq.4) and to basically operate the inverse Park transformation (A.6) to get and online update the L and E terms above (Eq.(22)).

Hence, from Equation(4), expressing the flux time derivative as done in Equation(13), assuming $[l_{dq}](\boldsymbol{i}_{dq}) = [l_{dq}](\boldsymbol{i}_{m,dq})$ and considering the zero-sequence component as well:

$$\begin{bmatrix} v_d \\ v_q \\ v_0 \end{bmatrix} = \underbrace{R_s \begin{bmatrix} i_d \\ i_q \\ i_0 \end{bmatrix}}_{R_{dq0}} + \underbrace{\begin{bmatrix} ldq \end{bmatrix} \frac{d}{dt}\begin{bmatrix} i_d \\ i_q \\ i_0 \end{bmatrix}}_{L_{dq0}} + \underbrace{\mathbf{J}\omega \begin{bmatrix} \lambda_d \\ \lambda_q \\ \lambda_0 \end{bmatrix}}_{E_{dq0}} \quad \text{where } \mathbf{J} = \mathbf{R}_z(\frac{\pi}{2}) = \begin{bmatrix} 0 & -1 & 0 \\ 1 & 0 & 0 \\ 0 & 0 & 1 \end{bmatrix} \quad (23)$$

Then, expressing $\boldsymbol{i}_{dq0}$ as $\mathbf{R}\boldsymbol{i}_{\alpha\beta0}$ and multiplying left and right side of Equation(23) for the inverse rotational matrix (A.3), it is possible to write:

$$\begin{bmatrix} v_\alpha \\ v_\beta \\ v_0 \end{bmatrix} = \underbrace{R_s \begin{bmatrix} i_\alpha \\ i_\beta \\ i_0 \end{bmatrix}}_{R_{\alpha\beta0}} + \underbrace{\mathbf{R^{-1}} \left[ldqls \right] \mathbf{R} \frac{d}{dt} \begin{bmatrix} i_\alpha \\ i_\beta \\ i_0 \end{bmatrix}}_{L_{\alpha\beta0}} + \underbrace{\mathbf{R^{-1}} \left[ldq0 \right] \frac{d\mathbf{R}}{dt} \begin{bmatrix} i_\alpha \\ i_\beta \\ i_0 \end{bmatrix} + \mathbf{R^{-1}} \mathbf{J} w \begin{bmatrix} \lambda_d \\ \lambda_q \\ \lambda_0 \end{bmatrix}}_{E_{\alpha\beta0}} \tag{24}$$

where

$$[ldqls] = \begin{bmatrix} ldd & ldq & 0 \\ lqd & lqq & 0 \\ 0 & 0 & Lls \end{bmatrix}, [ldq0] = \begin{bmatrix} ldd & ldq & 0 \\ lqd & lqq & 0 \\ 0 & 0 & 0 \end{bmatrix},$$

In $[ldqls]$, the additional inductive effect associated with the leakage flux (flux linkage that does not reach the rotor) has to be added. The reason for the addition of L_{ls} only over the homopolar component is that ldd and lqq are obtained from the flux maps that already account for the leakage term. In the following, such term will be considered with a constant value of 5% of the minimum value between ldd and lqq.

Conversely, since the leakage flux does not reach the rotor, there is no leakage inductance to account for in the motional term $[ldq0]$.

Multiplying both side of Equation(24) for the inverse Clarke matrix $\mathbf{T^{-1}}$ (A.2), expressing $\boldsymbol{i}_{\alpha\beta0}$ as $\mathbf{T}\boldsymbol{i}_{abc}$ and exploiting the Park symbols $\mathbf{P}, \mathbf{P^{-1}}$(A.5,A.6):

$$\begin{bmatrix} v_a \\ v_b \\ v_c \end{bmatrix} = \underbrace{R_s \begin{bmatrix} i_a \\ i_b \\ i_c \end{bmatrix}}_{R_{abc}} + \underbrace{\mathbf{P^{-1}} \left[ldqls \right] \mathbf{P} \frac{d}{dt} \begin{bmatrix} i_a \\ i_b \\ i_c \end{bmatrix}}_{L_{abc}} + \underbrace{\mathbf{P^{-1}} \left[ldq0 \right] \frac{d\mathbf{R}}{dt} \mathbf{T} \begin{bmatrix} i_a \\ i_b \\ i_c \end{bmatrix} + \mathbf{P^{-1}} \mathbf{J} w \begin{bmatrix} \lambda_d \\ \lambda_q \\ \lambda_0 \end{bmatrix}}_{E_{abc}} \tag{25}$$

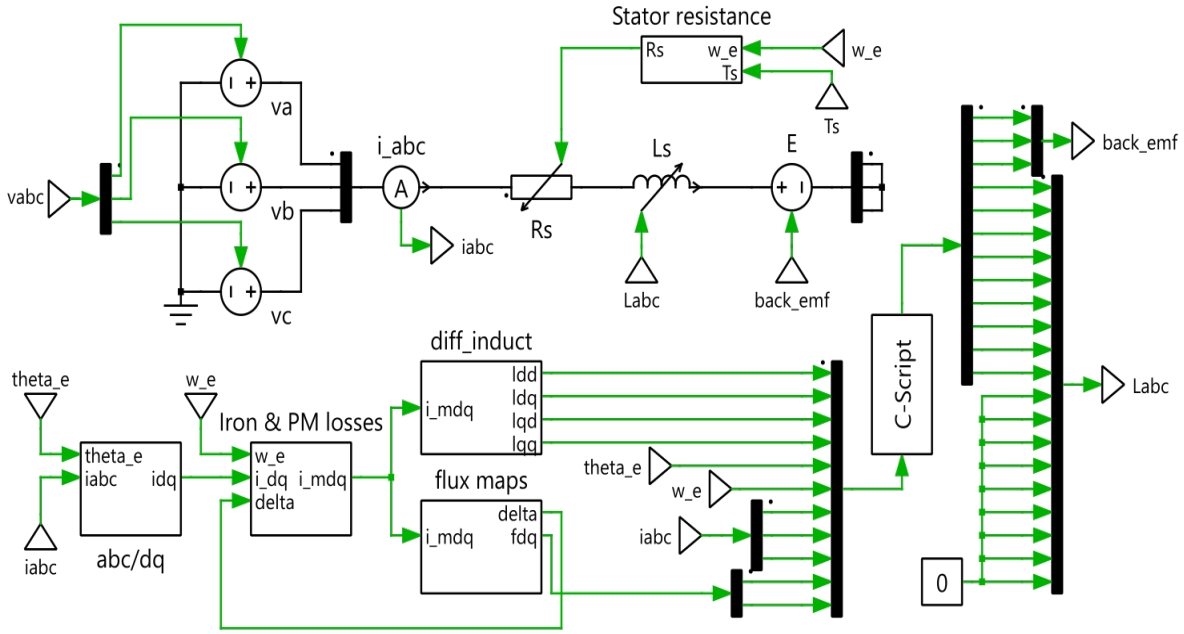

Figure 2.21: Voltage behind reactance model including losses.

In Figure 2.21, the C-script block performs all the above (Eq.(25) matrix products to get the matrix of the abc inductances and the abc back-emf voltages. The other entries, which define the abc inductances' time derivative, are set to zero because the abc inductances' variation is already present in the step-by-step updated inductance values.

2.5 Open-loop tests of the four SM models

Now that the four machine models are completed, open-loop tests can be done. From a desired stator dq currents the corresponding dq flux-linkages are obtained exploiting the flux maps (Section 2.2.2), neglecting the leakage current due to iron and PM losses.

Considering the steady-state form of the dq voltage equations (4), hence neglecting the flux derivative component and assuming nominal stator resistance R_{s0}, the corresponding steady-state reference dq voltages are computed.

The obtained dq voltages are then properly converted in abc voltages (A.5), provided in input to the models and a comparison between desired and obtained currents is done.

To ensure the convergence of the models, the dq current references are not set as step variations but as ramp ones with considerable dynamics.

A summary of the settings for these open-loop tests is shown in Table 2.

Table 2: Test conditions SM models.

Settings			
Initial abc current (VBR)	i_{abc0}	0,0,0	A
Initial d-axis magnetizing current (Current-based)	i_{md0}	0	A
Initial q-axis magnetizing current (Current-based)	i_{mq0}	0	A
Initial d-axis flux linkage (Flux-based/CCG)	$\lambda_{d0} = \lambda_{m0}$	0.0558	Vs
Initial q-axis flux linkage (Flux-based/CCG)	λ_{q0}	0	Vs
Final desired d-axis stator current	$min(i_d^*)$	-3e3	A
Final desired q-axis stator current	$max(i_q^*)$	3e3	A
Slopes desired dq currents	i_{Slope}^*	±1e5	A/s
Mechanical speed	n	1e5	rpm
Stator temperature	T_{Cu}	120	° C
Simulation time	t_{sim}	40	ms
Solver details			
Simulink solver	Ode45		
Plecs solver	RADAU		
Min step size	auto		
Max step size	1e-2		ms

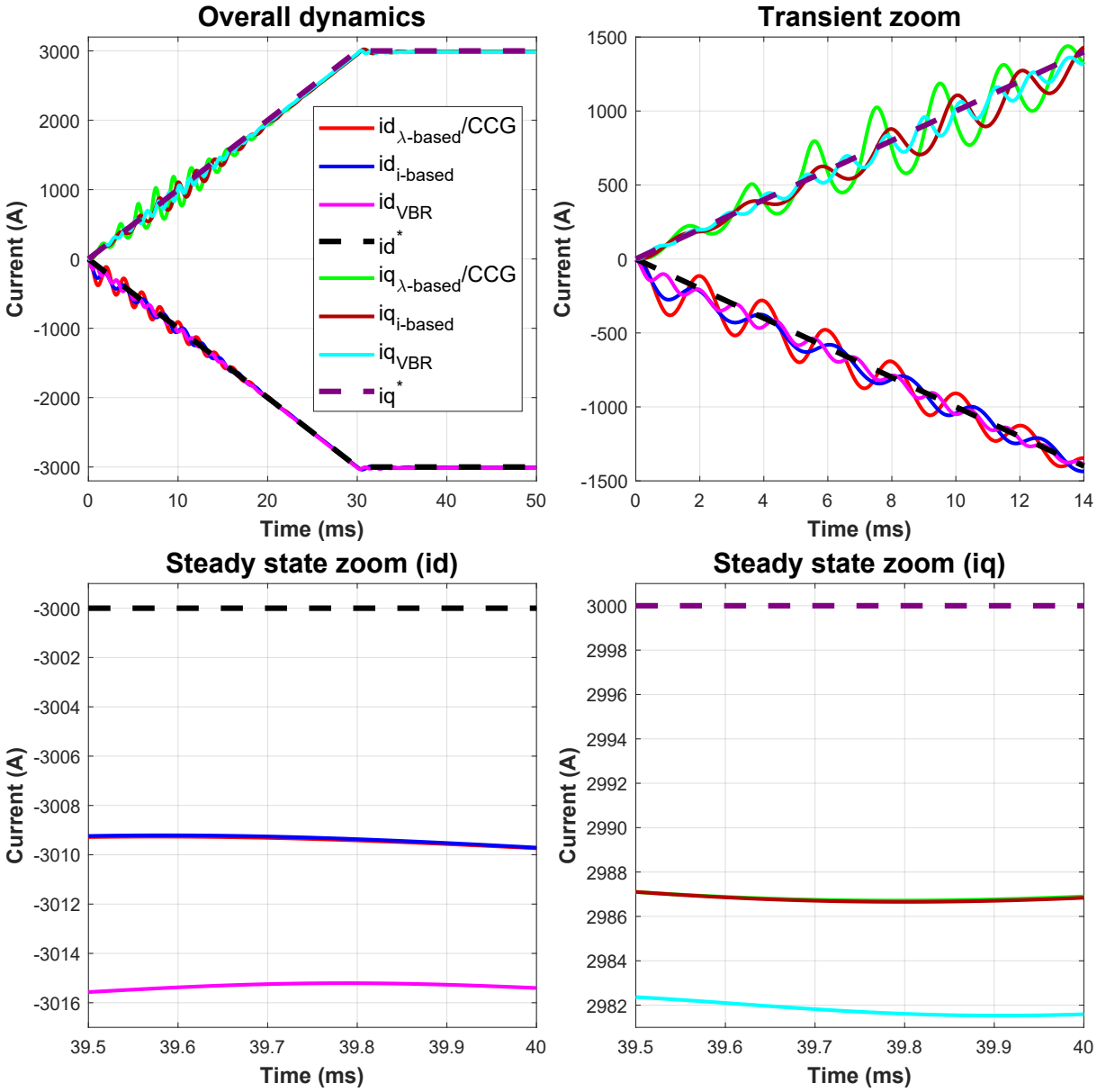

Figure 2.22: *dq* current dynamics in the OL tests of the four SM models.

The results in Figure 2.22 show the good convergence of all the machine models. The plots of the flux-based model and the CCG model are joined since as said the CCG model relies on the flux-based one.

In the transient, the flux-based model shows greater oscillations while the current-based and the VBR models appear more stable.
At steady-state instead, the gaps between the currents and their references are caused by the neglection of the loss current in the computation of the reference dq voltages.

Chapter 3:
Voltage Source Inverter and Modulation Techniques

For modelling and simulation purposes (Chapters:3,4) a three-phase two-level VSI equipped with Microsemi power modules *MSCSM120AM02CT6LIAG* (main specs in Table 3) and controlled with SV-PWM technique will be considered.

Table 3: SiC MOSFET (MSCSM120AM02CT6LIAG) main specs.

Microsemi SiC MOSFET			
Maximum Drain-source voltage	$V_{DS,max}$	1200	V
Maximum Continuous drain current @$T_C = 25°C$	$I_{D,max}$	947	A
Typical Drain-source on resistance @($T_C = 25°C$,$I_D = 480A$)	$R_{DS(on)}$	2.1	mΩ
Turn-on delay time @($T_j = 150°C$, $I_D = 600A$)	$T_{d(on)}$	56	ns
Rise time @($T_j = 150°C$, $I_D = 600A$)	T_r	55	ns
Turn-off delay time @($T_j = 150°C$, $I_D = 600A$)	$T_{d(off)}$	166	ns
Fall time @($T_j = 150°C$,$I_D = 600A$)	T_f	67	ns

3.1 Voltage source inverter

The primary role of the VSI is to convert the DC voltage source into a three-phase supply v_a, v_b, v_b able to control the machine. The VSI's power devices are controlled by means of PWM signals, received as input by the three PWM modulators.

The PWM modulators are typically integrated in the MCU with the triangular carrier approximated by an N-levels up/down counter and the duty cycle reference represented by a digit in the [0,N] range updated at each *interrupt service routine (ISR)*.
Replicating the clock-frequency-updated carrier would be tricky in simulation, requiring the use of a very tiny simulation step. Therefore, for simulation purposes, the PWM modulator are represented with their analog continuous-time counterparts.

The modulation technique as well is normally implemented in the MCU. However, only for this chapter, the modulation technique is implemented in continuous time inside the VSI block, with the intent of open-loop testing the VSI-SM block later, starting from the reference phase voltages (3.6).

3.1.1 Operating principles of a 2-levels voltage source inverter

Three-phase VSI most common and simple implementation is based on three legs, one for each phase, where each leg is composed of a series of two power devices (MOSFET or IGBT) acting as switches (see Figure 3.1). Whenever the upper switch is active the other one is not and viceversa. In the end, each phase of the machine receives a PWM phase voltage where the 'output' of each leg is represented by the node between the two power devices.

Assuming to split the DC voltage source of the inverter into a series of two identical DC voltage sources of amplitude $\frac{v_{dc}}{2}$,defining the virtual point O in between and referring the output voltages of the inverter legs to this point (v_{A0}, v_{BO}, v_{CO}), it is clear these latter can assume only two discrete values ,$\pm\frac{v_{dc}}{2}$, hence the name 2-levels VSI (see Figure 3.1 for clarity).

Neglecting for the moment the dead-time,hence assuming that the lower command of each leg is obtained just as the negation of the upper one,it is possible to express the inverter outputs dynamics based on such power switches commands through an instantaneous and a switching period averaged function:

$$\begin{aligned} v_{xO}(t) &= (2 \cdot q_x(t) - 1) \cdot \frac{v_{dc}}{2} \\ \bar{v}_{xO}(t) &= (2 \cdot d_x(t) - 1) \cdot \frac{v_{dc}}{2} \end{aligned} \tag{26}$$

Considering a star connection between the phases, hence defining the isolated neutral point n, the instantaneous and the averaged phase voltage equations are defined:

$$\begin{aligned} v_x(t) &= v_{xO}(t) - v_{nO}(t) \\ \bar{v}_x(t) &= \bar{v}_{xO}(t) - \bar{v}_{nO}(t) \end{aligned} \tag{27}$$

In addition,for symmetrical and balanced loads ($Z_a = Z_b = Z_c$, $e_a = e_b = e_c$) in star configuration :

$$v_{nO}(t) = \frac{1}{3}\left(v_{AO}(t) + v_{BO}(t) + v_{CO}(t)\right) \tag{28}$$

In the end,combining the Equations (26),(27), and (28),the instantaneous and averaged expressions (29) for the load voltages are retrieved.

$$
\begin{aligned}
v_a(t) &= \frac{v_{dc}}{3}\left(2\cdot q_a(t) - q_b(t) - q_c(t)\right) \quad \bar{v}_a(t) = \frac{v_{dc}}{3}\left(2\cdot d_a(t) - d_b(t) - d_c(t)\right) \\
v_b(t) &= \frac{v_{dc}}{3}\left(2\cdot q_b(t) - q_a(t) - q_c(t)\right) \quad \bar{v}_b(t) = \frac{v_{dc}}{3}\left(2\cdot d_b(t) - d_a(t) - d_c(t)\right) \\
v_c(t) &= \frac{v_{dc}}{3}\left(2\cdot q_c(t) - q_a(t) - q_b(t)\right) \quad \bar{v}_c(t) = \frac{v_{dc}}{3}\left(2\cdot d_c(t) - d_a(t) - d_b(t)\right)
\end{aligned}
\tag{29}
$$

In Figure 3.1 a three-phase 2-level VSI connected to a PMSM in star configuration.

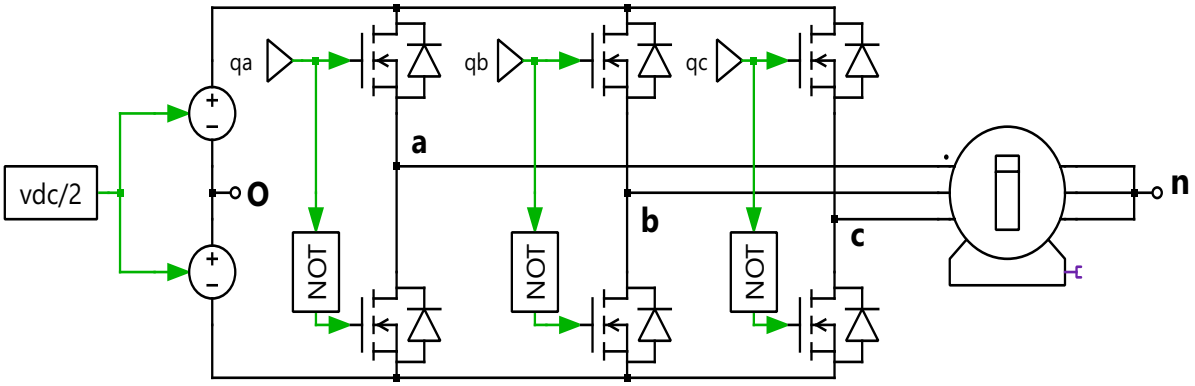

Figure 3.1: Three-phase two-level VSI.

The above expressions well defined the operations of an ideal 2-levels VSI. Due to the just two discrete values $\{0, 1\}$ that the switching function $q(t)$ can assume,the instantaneous phase voltages can have only five discrete levels $\{\pm\frac{2}{3}v_{dc}, \pm\frac{1}{3}v_{dc}, 0\}$.

Operating the Clarke transformation (A.1) of the 8 discrete combinations (000, 111, 100, 010, 001, 110, 101, 011), the result is a voltage space vector $\boldsymbol{v}$ which moves in the vertices and in the centre of an hexagon in the $\alpha\beta$ plane.

The average phase voltages over the switching period instead, can assume theoretically infinite states since the duty cycles can sweep continuously values between 0 and 1 (neglecting the discretization due to the finite number of bit of the controller). The boundaries within which the space vector $\boldsymbol{v}$ can move, are defined by the hexagon just introduced for the instantaneous case.

The goal of the modulation techniques is to maintain the linearity of the voltage regulation, obtaining phase voltages' fundamental components equal to the desired ones. Depending of the modulation technique, different linearity regions are defined.
The linearity limits of the sinusoidal modulation without common-mode injection (Section 3.2.1) are defined by a circle of radius $\frac{v_{dc}}{2}$, while the absolute linearity limits are defined with a circle of radius $\frac{v_{dc}}{\sqrt{3}}$. Crossing these latter limits means obtaining a deviation from the desired fundamental components of the phase voltages due to the saturation of the duty cycles, even with modulation techniques with common-mode injection as SV-PWM (Section 3.2.2).

The Figure 3.2 provides a graphical representation of the space voltage vector $\boldsymbol{v}$ in the $\alpha\beta$ plane, together with the limit regions just discussed.

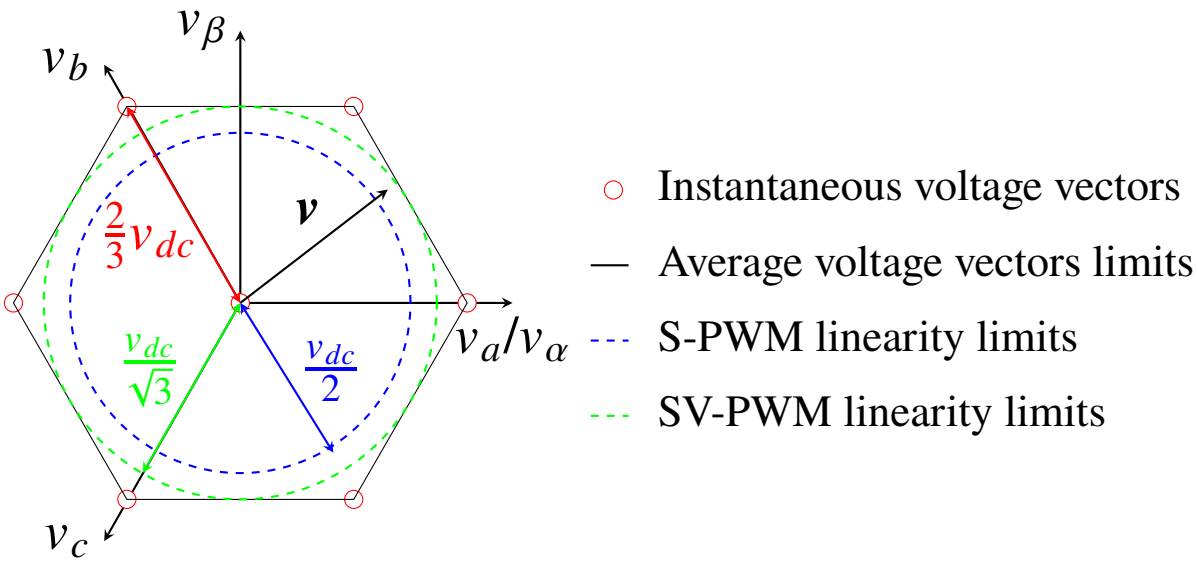

Figure 3.2: Voltage vectors of three-phase two-level VSI.

3.1.2 Non-ideality phenomena

There are three main loss phenomena that have to be taken into account in the VSI model:

- On-state resistance of the power switches and consequent conduction losses
- Dead-time insertion in the OFF-ON transition
- Power switches losses due to the commutations

In contrast with the ideal case, the conduction channel of the IGBT and SiC MOSFET in the on-state presents a resistance ($R_{CE(on)}$ or $R_{DS(on)}$).
This resistance causes a voltage drop that decrease the effective inverter output voltages v_{AO}, v_{BO}, v_{CO}, hence decreasing the range of the linear region.

In order to avoid short-circuiting the input DC voltage source, it is necessary to add a dead-time between the two consecutive ON-state commutations of the two power devices of each VSI's leg. The amount of necessary dead-time depends on the ON and OFF-commutation times of the power devices and it is part of the design. SiC MOSFETs have significantly faster dynamic resulting in dead-times in the order of 500 ns against values typically higher than 1 us for IGBTs.

Finally, without affecting the inverter output dynamics, the switching and conduction losses can be computed. The first ones are obtained from the turn-ON and turn-OFF energy and are mapped with a LUT. The second ones instead, are simply defined by the product of the on-state voltage drop and the phase current. Summing them, an estimate of the overall losses of the VSI is obtained.

3.2 Modulation techniques

The PWM signals are square waves with varying duty cycles that are sent to gate driver circuits, which generate the corresponding gate control signal for the VSI's power switches.

In carrier-based PWM such signals derive from the comparison of a modulating/reference signal with an high-frequency carrier. Adopting an unipolar unitary peak triangular carrier, means obtaining a PWM signal whose duty cycle d is equal to the modulating signal v_c, with $0 \leq v_c \leq 1$. The carrier period determines the switching one T_{sw}, where a switching frequency of $10kHz$ will be considered in the following.

For a 2-level voltage source inverter piloting a three-phase machine, three PWM modulators are needed, one for each phase. The commands for the lower switches are obtained from the upper ones, with a logic which accounts for the dead-time insertion, at least for a the Plecs circuital implementation (Section 3.5.)

3.2.1 Sinusoidal-PWM

The simplest way to obtain the reference duty cycle from the reference phase voltages is called sinusoidal modulation. The starting point is the averaged expression in Equation (26), where imposing a sinusoidal wave ($V^*(\sin(\omega t))$ as desired mobile mean value of the averaged inverter leg output voltage, the reference duty cycle $d_x^*(t)$ is extrapolated as:

$$d_x^*(t) = \frac{V^*}{v_{dc}} \sin(\omega t) + 0.5 \tag{30}$$

In addition, considering the averaged expressions of Equations(27) and (28), assuming a balanced three-phase system where: $\bar{v}_{AO}(t) = V^* \sin(\omega t), \bar{v}_{BO}(t) = V^* \sin(\omega t - \frac{2\pi}{3}), \bar{v}_{CO}(t) = V^* \sin(\omega t + \frac{2\pi}{3}) \rightarrow \bar{v}_{nO}(t) = 0$;
the following equality is defined:

$$\bar{v}_x(t) = \bar{v}_{xO}(t) \tag{31}$$

This results demonstrate the possibility of imposing a desired mobile-average phase voltage $\bar{v}_{xn}(t)$, exploiting the duty cycle expression above (30), extrapolated for a generic inverter leg. The obtained reference duty cycles d_a^*, d_b^*, d_c^* are sent to the CB-PWM modulators which generate the control signals. A Plecs implementation of a S-PWM is shown in Fig. 3.3. A saturation block limits the imposed duty cycle dynamics from 0 to 1.

In order to proper control the machine torque it is mandatary to operate in the so-called linear region, where the fundamental component of the obtained phase voltages v_a, v_b, v_c corresponds to the desired moving average values (apart for inverter non ideality) and the voltage harmonics are confined at high frequency around the switching frequency. With this kind of modulation technique the linear region goes from 0 to $\frac{v_{dc}}{2}$.

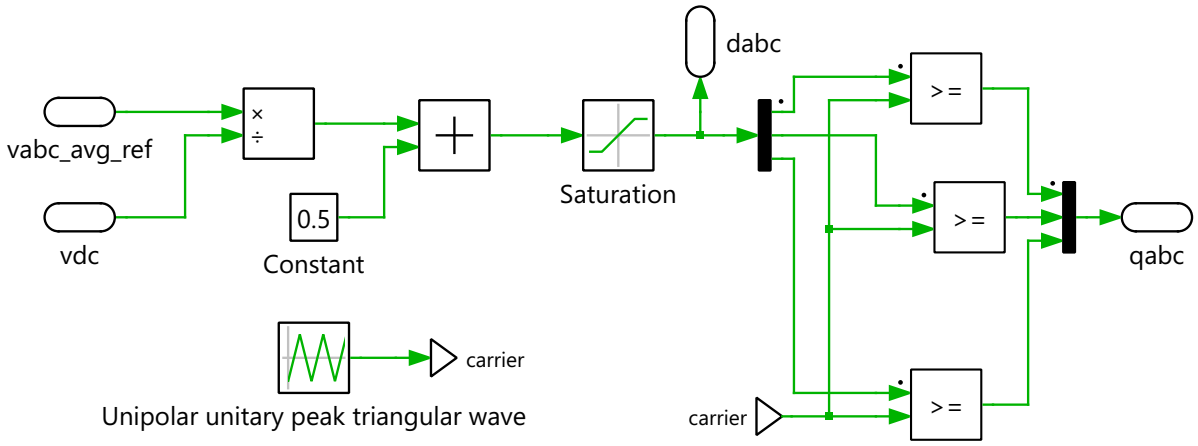

Figure 3.3: Sinusoidal modulation.

3.2.2 Space vector-PWM

Different modulation techniques with different optimization criteria are present in the literature. The majority of them exploit the common-mode rejection of the phase voltages.

Indeed, based on Equation(27), it is evident the possibility to impose inverter output voltages $v_{AO}(t), v_{BO}(t), v_{CO}(t)$ starting from the desired phase voltages $v_a(t), v_b(t), v_c(t)$ and adding a computed common mode to all of them $v_{nO}(t)$.
As result, the phase voltages will reject the common-mode and will coincide to the reference ones. The advantages are that with this trick it is possible to optimize certain criteria maintaining the linearity.

Among all the modulation techniques the most adopted is the so-called space vector modulation. Its primary objective is to extend the linear region up to the VSI sinusoidal limit,i.e. $\frac{v_{dc}}{\sqrt{3}}$. To do that, from the desired phase voltages, the common-mode voltage is computed through the expression:

$$v^*_{nO} = -\frac{\max(v^*_a, v^*_b, v^*_c) + \min(v^*_a, v^*_b, v^*_c)}{2} \tag{32}$$

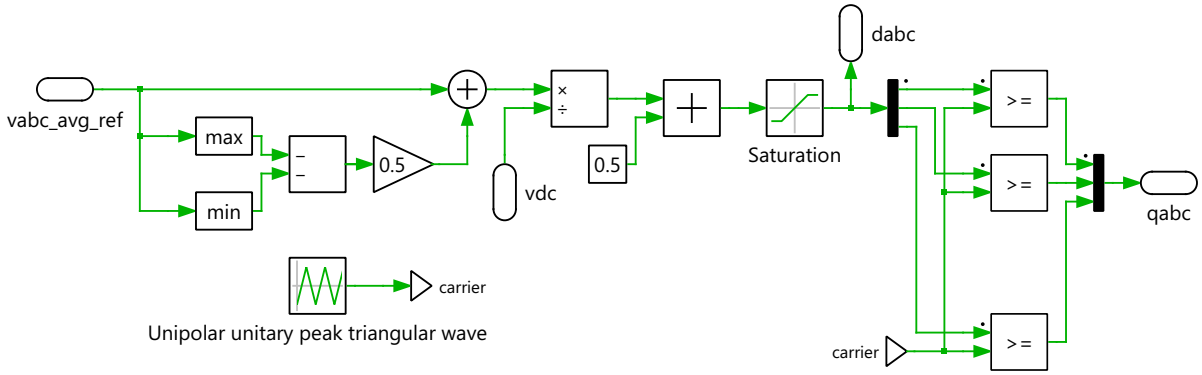

Figure 3.4: Space-vector modulation.

3.3 Matlab maps extrapolation

3.3.1 On-state resistance map

The conduction resistance is temperature dependent. In the datasheet the normalized profile of $R_{DS(ON)}$ in the [25 °C,180 °C] range of junction temperature is provided (Test conditions:$V_{GS} = 20V$,$I_D = 600A$). Hence, the intent is to replicate in Matlab this function, eventually extending the temperature domain with Matlab's *curve fitting tool*. Further, being the maximum drain current (947A at 25 °C) below the maximum motor current, two modules in parallel are needed.

With this setup, the computed normalized resistive profile is adapted multiplying for the typical resistance at 25 °C (2.1 mΩ) and divided by the two modules in parallel. The final map is shown in Fig. 3.5.

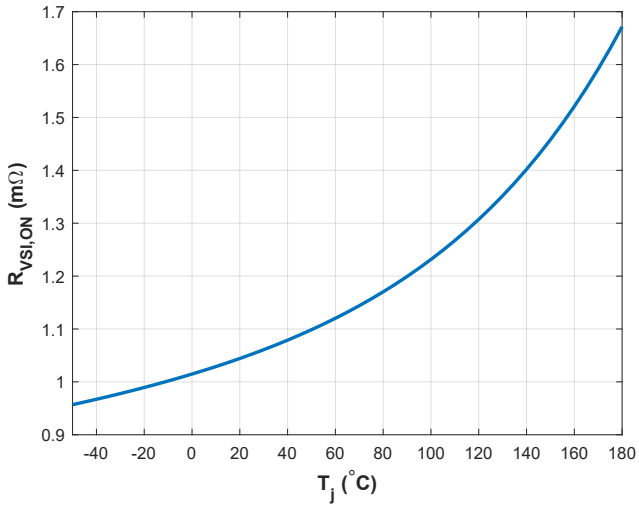

Figure 3.5: Temperature dependence of the ON-state resistance for the parallel of two SiC MOSFET.

3.3.2 Switching losses map

The commutation losses depend mainly on the commutated current. The datasheet provides the profile of the dissipated turn-ON and turn-OFF energy (E_{on}, E_{off}) for a range of current between 50 and 600 A (Test conditions:$V_{GS} = [-5, 20]$,$T_J = 150\,°C$,$V_{bus} = 600V$).

Summing E_{on} and E_{off}, the total dissipated energy E_{tot} in one switching period per MOSFET is obtained. Extending the current domain with the *curve fitting tool*, accounting for the two power devices in a leg, for the two modules in parallel and multiplying for the switching frequency f_{sw}, the final map shown in Figure 3.6 is obtained.

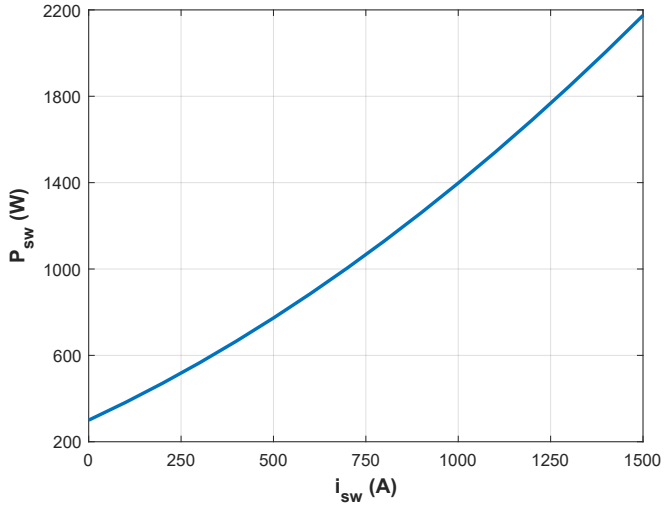

Figure 3.6: Switching losses per phase with combined commutated current dependence.

To note that the commutations with zero current present losses due to the parasitic capacitances.

3.3.3 Dead-time selection and equivalent voltage drop

At given test conditions: $V_{GS} = [-5, 20]$,$T_J = 150\,°C$,$V_{bus} = 600V$ and $I_d = 600A$, the datasheet reports a turn-OFF delay of 166 ns and a current fall time of 67 ns. In order to account for additional non-considered phenomena, the dead time is imposed approximately at twice the sum of the two reported delays with a value of 500 ns.

To approximate the effects of the dead-time, the equivalent voltage drop is computed as:

$$v_{err_{dt}} = v_{dc} \cdot \frac{t_{dt}}{Tsw} \cdot sign(i_x) \tag{33}$$

where i_x represent the generic phase current.

3.4 Simulink VSI model

The implementation of the PWM modulator is straightforward and it is represented by a relational operator.
The effective load voltages v_a, v_b, v_c are computed based on Equations (26),(27),(28), also considering the ON-state voltage drop over the SiC MOSFET and the dead time equivalent voltage drop.
The switching losses are computed based on the commutated phase currents i_a, i_b, i_c and are combined with the Joule losses due to ON-state resistance to provide the total losses of the inverter.

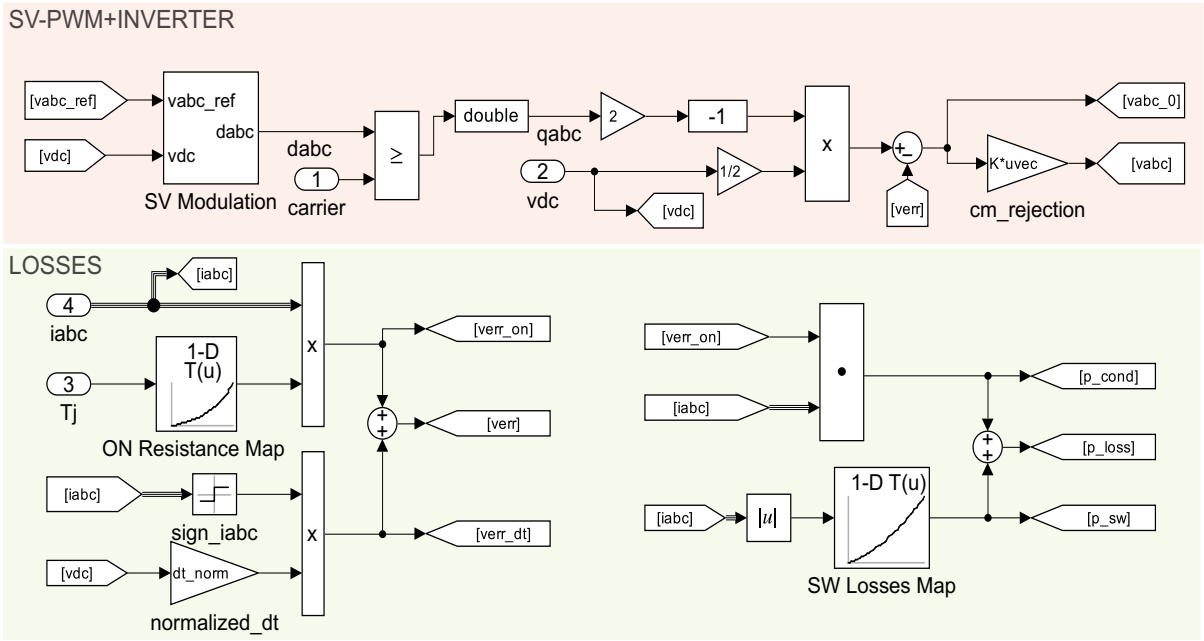

Figure 3.7: Simulink / SV-PWM and VSI with non-ideality phenomena.

3.5 Plecs VSI model

In Plecs, the approach is 'component' based, hence the ON-state resistance (half the value of a single SiC-MOSFET resistance due to the parallel), at certain junction temperature, can be directly set up in the power devices.

Dead-time insertion is done first by obtaining the control signals and their negations and then delaying the turn-ON passage by means of a turn-ON delay block.

Switching and conduction losses are not computed here.

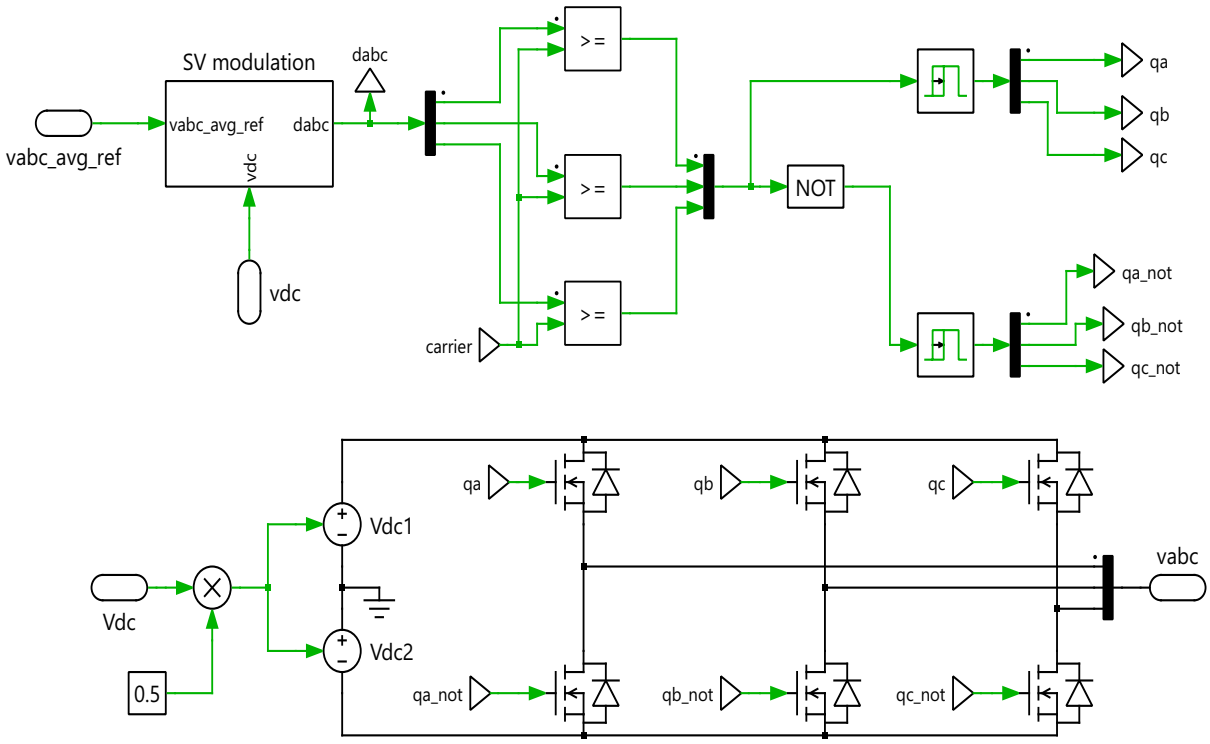

Figure 3.8: Plecs / SV-PWM and VSI with non-ideality phenomena.

3.6 Open-loop tests of the block SVPWM-VSI-SM

After the develop of an exhaustive SVPWM-VSI model, two of the machine models described in Sections 2.3 and 2.4 (Flux-based dq model and VBR model) are put in cascade and the two resulting blocks SVPWM-VSI-SM are open-loop tested with the settings reported in Table 5.

The difference with respect to Section 2.5 where only the machine is tested, is that this time the imposed abc voltages are not equal to the sinusoidal ones derived from the reference dq voltages, but instead pulsed as result of the SVPWM-VSI action.

To define the reference dq voltages, the starting point is again the setting of desired stator dq currents, exploiting the steady-state form of the dq electrical model (Eq.4) and assuming the nominal stator resistance R_{s0}.

Once the reference abc voltages are obtained (A.5), the SV-PWM technique is used to retrieve the control signals. Hence, the inverter's output voltages v_{abc} are provided in input to the machine models.

With the aim of testing one $\boldsymbol{i}_{dq}$ point satisfying the voltage and current constraints, the MTPS profiles shown in Figure 2.8 are considered. Recalling that those profiles are defined for a voltage limit of $0.9\frac{v_{dc0}}{\sqrt{3}}$ lower than the real sinusoidal linearity limits (Figure 3.2), the convergence to the MTPS torque defined for the chosen speed point should be guaranteed even considering the non-ideality phenomena which decrease the linearity region.

Table 4: Test conditions SVPWM-VSI-SM simulations.

Settings			
Initial abc current (VBR)	i_{abc0}	0,0,0	A
Initial d-axis flux linkage (Flux-based)	λ_{d0}=λ_{PM}	0.0558	Vs
Initial q-axis flux linkage (Flux-based)	λ_{q0}	0	Vs
Mechanical speed	n	6e3	rpm
Final desired d-axis stator current	$min(i_d^*)$=$i_{d,MTPSm}(n)$	-1247	A
Final desired q-axis stator current	$max(i_q^*)$=$i_{q,MTPSm}(n)$	314	A
Slopes desired dq currents	i^*_{Slope}	±1e5	A/s
Final desired torque	$max(Te^*)$=$Te_{MTPSm}(n)$	283	Nm
DC-link voltage	v_{dc}=v_{dc0}	230	V
SiC-MOSFET junction temperature	T_j	100	° C
Stator temperature	T_{Cu}=T_{Cu0}	120	° C
Dead time	t_{dt}	500	ns
Switching frequency	f_{sw}	2e4	Hz
Simulation time	t_{sim}	40	ms
Solver details			
Simulink solver	Ode45		
Plecs solver	RADAU		
Min step size	auto		
Max step size	$\frac{T_{sw}}{100}$ s		

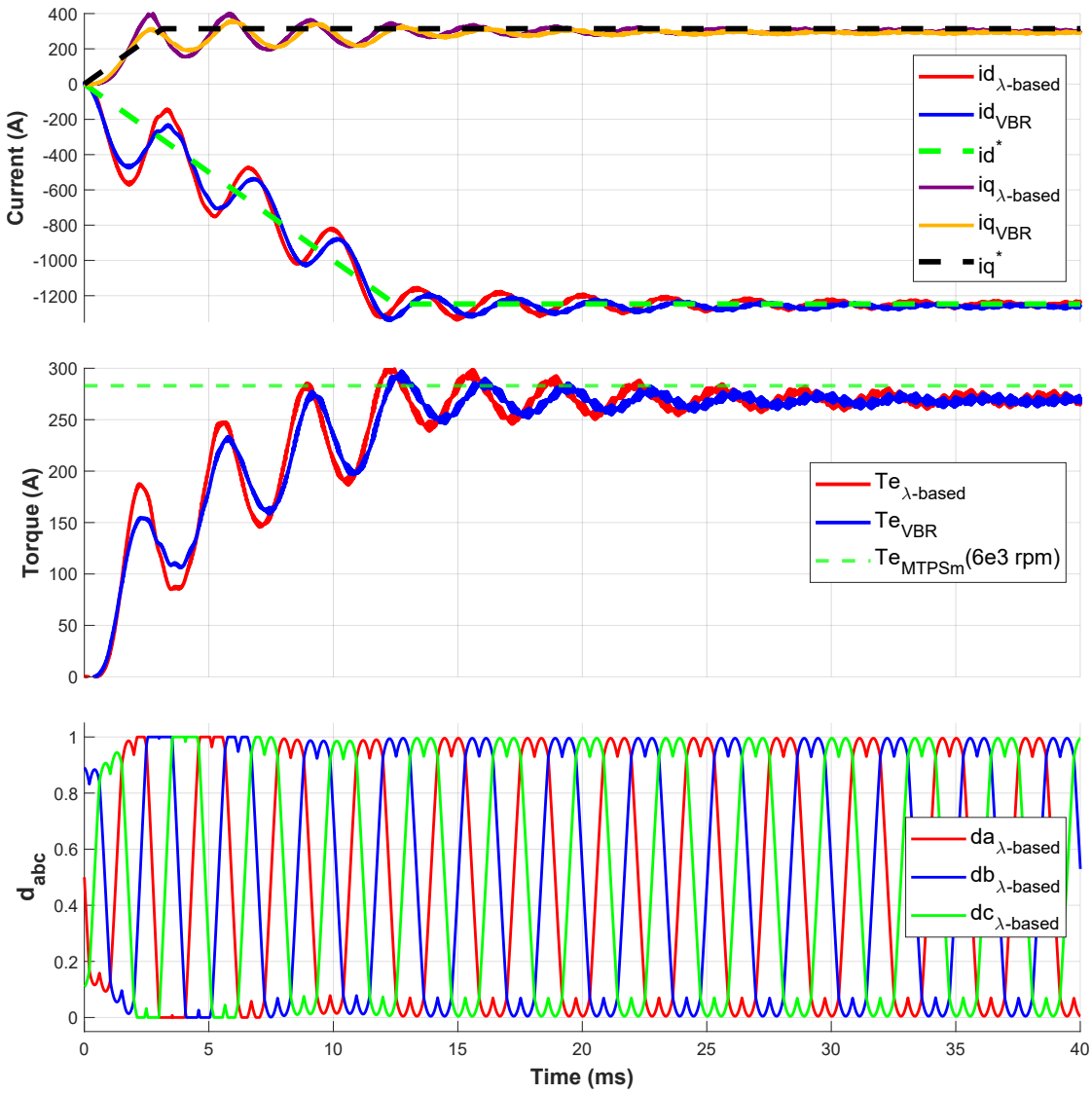

Figure 3.9: Torque,dq current and duty cycles dynamics in the OL tests of the SVPWM-VSI-SM block.

The results in Figure 3.9, show the great convergence of the dq currents and torque to the reference values. The little gap at steady state is again caused by the neglection of the loss current in the computation of the dq reference voltages, as well as increased by the dead-time effect and the power devices' voltage drop.

Given that the test point (6e3 rpm) is along the MTPS retrieved for $V_{max} = 0.9\frac{v_{dc0}}{\sqrt{3}}$, the duty cycles are close to saturation at steady state and saturate a bit during the transient. Due to the graphical superpositions of the duty cycles of the two OL tests, just the duty cycles dynamics obtained with the flux-based Simulink model are reported in Figure 3.9.

Chapter 4:
Motor Control Unit

As anticipated in Chapter 1 and shown in Figure 1.1, the Motor Control Unit is the core of the control, providing in output the proper commands for the inverter's power switches.

However, similarly to what is done in Chapter 3, the PWM modulator is included in the VSI block, leaving the modulation technique (SV) inside the MCU block and as output the sample-time updated reference duty cycles d_a^*, d_b^*, d_c^*.

Regarding the inputs, the MCU receives the torque request Te_{IN}^* (typically from the Vehicle Control Unit VCU or Traction Control Unit TCU and already accounting for the maximum/minimum constraints computed by the MCU at the previous step) and acquires the measurements of the rotor position θ_m and phase currents i_{abc}.

In addition, the MCU typically further limits the input reference torque based on the actual k-step computed maximum/minimum constraint, obtaining in the end, the feasible reference torque Te^*.

4.1 Analog-to-digital conversion and execution delay

Being a digital controller, all the measurements are discretized using an analog-to-digital conversion. As a consequence, sampling time and quantization error phenomena must be taken into account.

Usually, the analog ports of a performance microcontroller are associated with A/D converters having from 12 to 16 bits, resulting in quantization errors generally negligible.

Different story for the sampling time which determines the frequency at which all the computations on the microcontroller are updated, including the duty cycles. Normally, the sampling period also called (ISR,interrupt-service-routine), is set equivalent to the switching period T_{sw}.

However, especially for cases where T_{sw} is not so high, T_s can be set as $\frac{T_{sw}}{2}$, improving the performances. This derives from the symmetry with respect to the peak of the triangular wave which makes possible obtaining the desired duty cycle already at the first half of the switching period (Fig.4.1), allowing the eventual refresh of this latter in the second half.

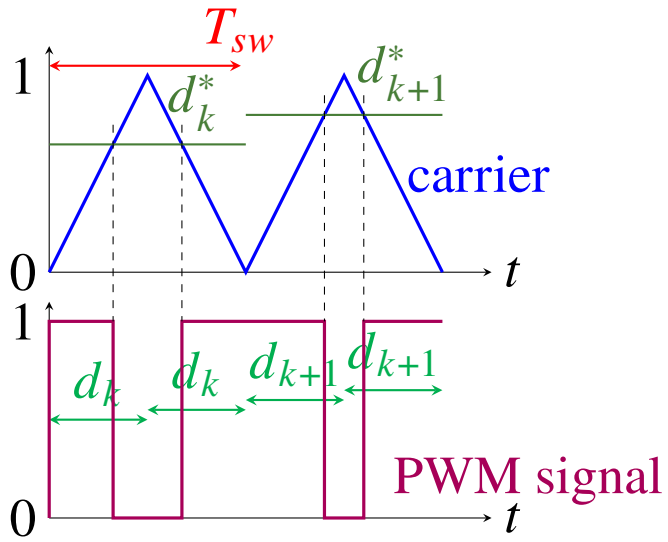

Figure 4.1: CB-PWM modulator.

The feasibility of the double sampling and double refresh approach depends on the speed of the microcontroller doing all the acquisitions and the calculus before the next sampling time. Indeed, another phenomenon that have to be considered is the so-called execution delay, which prevents the microcontroller from instantaneously updating the control commands. Therefore, the control commands computed at the current sampling period are applied in the next sampling instant.

Both Simulink and Plecs allows the modelling of the sampling effect with the use of the triggered subsystems, i.e., subsystems where each operation inside is done following the rising or falling edges of a trigger signal having as period the desired sampling time. About the execution delay instead, one-step delay is added in cascade to the computed duty cycles.

4.2 Position tracking observer

Considering sensored control schemes, the rotor position is measured via different types of position sensors (encoders, resolvers, hall effect sensors...).The rotor speed is usually not measured and therefore it must be estimated from the position measurements.

A simple and reliable way to estimate the speed from the position is derived from the proposed position-tracking observer in [2]. In the end, it is a closed-loop layout that tries to nullify the deviation of the estimated position from the measured one by means of a discrete PI regulator. In order to tune such PI, the Laplace equivalent scheme in Figure 4.2 is considered.

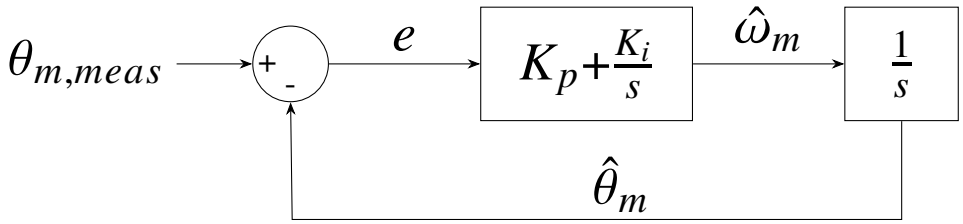

Figure 4.2: Laplace block diagram PTO.

The OL transfer function is expressed as:

$$G(s) = \left(K_p + \frac{K_i}{s}\right) \cdot \frac{1}{s} \tag{34}$$

At the crossover frequency:

$$|G(jw_c)| = \left|\frac{K_p jw_c + K_i}{(jw_c)^2}\right| = 1 \rightarrow \sqrt{(K_p w_c)^2 + K_i^2} = w_c^2 \tag{35}$$

$$\angle G(jw_c) = atan2(K_p w_c, K_i) - 180^\circ \rightarrow PM = atan2(K_p w_c, K_i) \rightarrow K_i = \frac{K_p w_c}{tan(PM)} \tag{36}$$

Substituting the last expression of (36) into (35):

$$\sqrt{(K_p w_c)^2 + \left(\frac{K_p w_c}{tan(PM)}\right)^2} = K_p w_c \sqrt{1 + \left(\frac{1}{tan(PM)}\right)^2} = w_c^2$$

$$K_p = \frac{w_c \cdot tan(PM)}{\sqrt{1 + tan^2(PM)}} \tag{37}$$

$$K_i = \frac{w_c^2}{\sqrt{1 + tan^2(PM)}}$$

Considering a unitary feedback path and an adequate phase margin, the bandwidth of the closed-loop system can be approximated to the crossover frequency, $f_b \approx f_c$. A good rule of thumb here is to set f_b in the range $[30, 50]Hz$ and a phase margin $PM >= 60°$.

In order to implement the observer in the discrete domain, the continuous integrators are substituted with the discrete ones, adopting for simplicity the Forward Euler integration method and setting zero initial conditions. Furthermore, since the final output of an absolute position sensor is typically in the range $[-\pi, \pi]$ or$[0, 2\pi]$, the normalization of the estimated angle must be performed. However, this normalization makes the angles' dynamics discontinuous with 2π amplitude jumps from the higher to lower limit, leading to the instability of the observer. To overcome this problem the continuity of the sine is exploited and the sine of the difference is computed.

In addition, the considered estimated speed is taken at the output of the PI integrator to filter the noise otherwise present due to the proportional action, even though the dynamic performance suffers a bit.

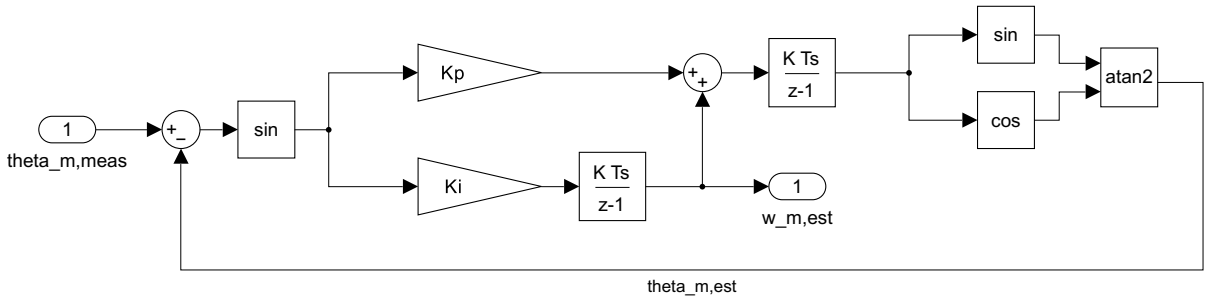

Figure 4.3: Simulink PTO.

4.3 Stator flux observer

Apart the CVC approach (Section 4.4.1), all the other control strategies require the estimation of the stator flux linkage. Since there are no flux transducers, a stator flux observer is needed.

The first idea that comes to mind is to exploit the flux maps (Section:2.2.2). Hence, given the measured currents $\boldsymbol{i}_{abc}$ and the derived electrical angle θ_d (from $\theta_{m,meas}$), operating the Park transformation (A.5) to get the $\boldsymbol{i}_{dq}$ currents, the $\boldsymbol{\lambda}_{dq}$ fluxes are obtained, neglecting the iron and PM losses. This approach is called $I\theta$ estimator since the only information needed are the sensed currents and the angle. However, the reliability of this latter is confined at very low speed, where the leakage current due to iron and PM losses is negligible (Fig.2.1). Another problem that occurs at high speed is the noise due to the sampling of the currents which brings noise in the derived fluxes.

An alternative way to estimate the flux is called VI estimator. Starting from the previous-step computed duty cycles and the measured dc-link voltage, it reconstructs the phase voltages v_{abcRec} based on Equation (29), considering also the voltage errors due to the inverter. Then, operating the Clarke transformation (A.1) both to reconstructed voltages and to the measured phase currents $\boldsymbol{i}_{abc}$, the $\boldsymbol{\lambda}_{\alpha\beta}$ time derivative can be isolated from the $\alpha\beta$ voltage equations (Eq.38).

$$\begin{bmatrix} v_\alpha \\ v_\beta \end{bmatrix} = R_s \begin{bmatrix} i_\alpha \\ i_\beta \end{bmatrix} + \frac{d}{dt} \begin{bmatrix} \lambda_\alpha \\ \lambda_\beta \end{bmatrix} \tag{38}$$

Integrating and operating the rotational transformation (A.3) the corresponding $\boldsymbol{\lambda}_{dq}$ fluxes are retrieved. The accuracy of this estimator is this time confined at high speed, since at low speed the integration of the back emf ($\frac{e_{\alpha\beta}}{s}$) tends to an undefined form since both numerator and denominator tend to zero. Another drawback of this approach is the lack of immunity to the possible dc components present in $\boldsymbol{i}_{\alpha\beta}$ and $\boldsymbol{v}_{\alpha\beta}$, that are integrated and can cause drift errors.

Merging the two approaches in what nowadays is called the Gopinath flux observer [3], allows the exploitation of the $I\theta$ estimator at low speed and of the VI one at high speed. A Simulink implementation of the Gopinath observer, is shown in Fig.4.4.

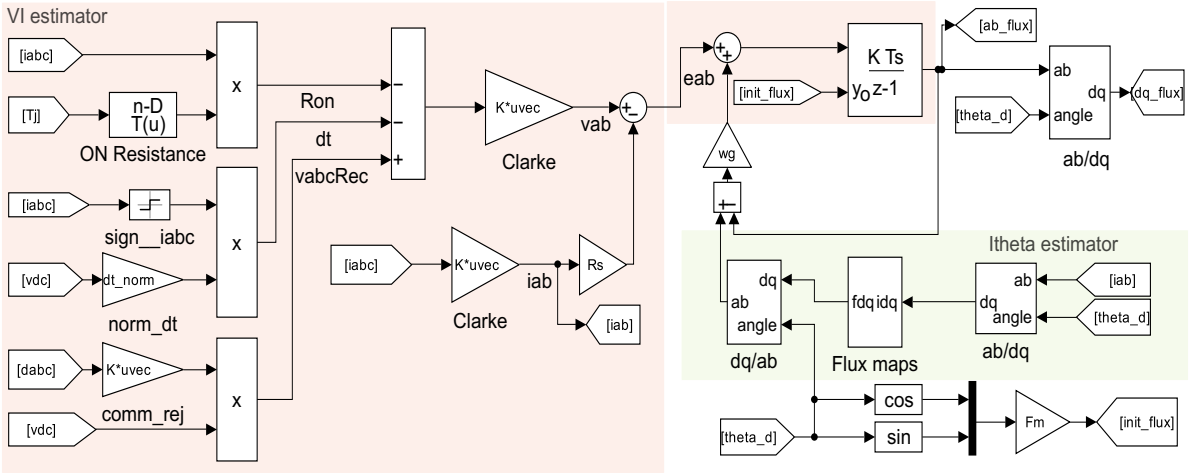

Figure 4.4: Gopinath stator flux observer.

The transition between the two estimators is determined in frequency by the gain w_g. Indeed,it can be demonstrated that:

$$\hat{\boldsymbol{\lambda}}_{\alpha\beta} = \hat{\boldsymbol{\lambda}}_{\alpha\beta_{I\theta}} \cdot \frac{w_g}{s + w_g} + \hat{\boldsymbol{\lambda}}_{\alpha\beta_{VI}} \cdot \frac{s}{s + w_g} \tag{39}$$

The first term in (39) is related to the $I\theta$ estimator and is associated with a low pass filter with a cut-off frequency of $f_{cut} = \frac{w_g}{2\pi}$, while the second one is related to the VI estimator and is associated with an high pass filter with the same cut-off frequency.

The correct initialization of the integrator is fundamental to ensure that the observer provide the correct flux at the startup-up and hence to prevent any current spikes in any of the flux-based control approaches. In addition, the forward Euler integration method have to be used to avoid adding a phase shift between sampled current and observed flux, which in the end leads to instability.

4.4 Control approaches in dq rotor coordinates

The torque control in dq rotor coordinates relies on the dq voltage equations (Eq.4). The d axis is used to control the d component of the current i_d (CVC, Section 4.4.1) or of the flux-linkage λ_d (FVC, Section 4.4.2), while in the same way the q axis is used to regulate i_q or λ_q.

Talking about the control of constant quantities in such a rotor dq frame (Section 1.3), the use of two PI regulators is straightforward and each regulator's output is used to set the reference voltage for the same axis.

The first step to do is the translation of the desired torque in the corresponding dq quantities ($\boldsymbol{i}_{dq}*$ or $\boldsymbol{\lambda}_{dq}*$),considering the speed, the dc voltage, eventual current limitations and so on. The second one is instead the proper regulation of such quantities to ensure quickness and stability in the case of sudden change of the torque request.

In order to improve the performance of the control, the feed-forward action is implemented. Essentially, as the name suggests it consists in adding at the output of the PI regulators any known contribution to speed-up the control and help the regulators action. In this case, based on Equation(4), the known terms are represented by the motional terms $\omega\lambda_q$ and $\omega\lambda_d$ that are added at the output of the PI regulators with the proper sign.

An other ingredient to build a stable closed-loop system is the Anti-windup mechanism. Its task is to prevent integrator from accumulating errors when the control signal has reached its limits. In this way the integral part is totally disengaged in the case of strong step variation where the proportional part quickly react and saturates the output. The integral action becomes effective again after the fast transient, preventing big overshoot or even instability. In this thesis, as Anti-windup method, the clamping one is adopted in the discrete PIs.

To properly mimic the inverter's capability, the reference voltage asked by the controllers have to be bounded. According to the sinusoidal voltage limit imposed by the considered SV-PWM ($v_{lim} = \frac{v_{dc}}{\sqrt{3}}$), given the priority to one axis, the voltage limits of each axis are found. For instance, given the priority to the d axis: $v_{lim,d} = \pm v_{lim}$ and $v_{lim,q} = \pm\sqrt{v_{lim}^2 - v_d{*}^2}$. In order to get the actual PIs' output limits, the feed-forward action is removed from the these latter axis limits.

This static prioritization represents one of the problems of the rotor dq control approaches since the voltage request between the two axes dynamically changes. During a torque reversal test for example, the q axis requires more voltage to reverse the q axis component while being at steady-state and high speed, requires more voltage in the d axis since i_d has to counteract the magnet flux. In the implementations proposed, the priority is given to the d axis. The problem is that at high speed the d axis saturates the voltage limit, preventing the q axis regulator from controlling i_q and hence generating oscillations on the torque.

4.4.1 Current vector control (CVC)

The most intuitive way to retrieve the current references is to exploit the maps shown in Fig.2.10 and 2.11. Building such maps for multiple values of dc voltage and concatenating along this latter dimension, the final result are 3-D maps, that given the torque request, the current speed and the dc-link voltage, provide the stator currents $\boldsymbol{i}_{dq}*$ [4].
However, to avoid NaN results as these latter maps's outputs, the input torque request Te^*_{IN} have to be preliminarily bounded, building the MTPS limits for multiple values of v_{dc}, obtaining hence the feasible reference torque Te^*. In addition, to ensure the stability of the control, an additional safety coefficient $k_{vlim} < 1$ is considered to get the $v_{dc,LUT}$ used in the interpolation of the maps. Eventually, further dependencies can be added increasing the maps' sizes.

In the case the losses are unknown or bad estimated, an alternative solution is to adopt a slightly modified version of the Bae-Patel (BP) control structure [5] (Figure 4.5).

Indeed, compared to the original proposed BP solution, the outer voltage loop is not implemented and an additional dependence on the magnetizing current limit is added, as well as a voltage limit safety coefficients $k_{vlim} < 1$.

The price to pay with respect to the EM-based approach is a bit of torque error especially at high speed where the not accounted losses come out. Indeed, the BP-LUTs in Figure 4.5, are previously computed in Matlab starting from the given flux-linkage maps (Section 2.2.2) and hence provide in output the magnetizing currents $\boldsymbol{i}_{m,dq}*$ and not the stator ones $\boldsymbol{i}_{dq}*$ needed. Therefore, part of these reference currents are dissipated by the iron and PM losses, resulting in a torque discrepancy at high speed.

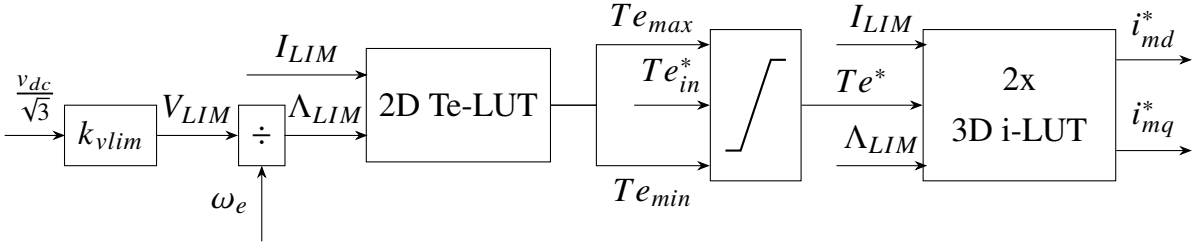

Figure 4.5: Bae-Patel-based considered control structure.

Independently of the approach used to retrieve the reference dq currents, the tuning of the PI regulators is done modelling all the blocks in the Laplace domain.

As discussed in Section 4.1,the reference duty cycles become effective after the first half of the switching period. Moreover, the desired duty cycles are applied with an execution delay of at least one sampling period. In the end, the effects of the PWM and of the MCU are modeled with a first-order delay approximation of $1.5T_{sw}$. The VSI is considered ideal for simplicity.

To build the machine transfer function, the starting point is represented by the dq voltage equations (Eq.(4)), where the derivatives of the flux-linkages are expressed exploiting (13) and assuming $[l_{dq}](\boldsymbol{i}_{dq}) = [l_{dq}](\boldsymbol{i}_{m,dq})$. The intent is to find the in-out relation, considering as input of each axis expression, the sum of the corresponding voltage and the back-emf term and as output the considered axis current.

Furthermore, assuming negligible the cross-differential inductances l_{dq} and l_{qd} as well as the resistive voltage drop, the result for a generic operating point ($\boldsymbol{i}_{dq}$) (42) is obtained:

$$\begin{aligned} l_{dd}\frac{di_d}{dt} \approx v_d + \omega_e\lambda_q \xrightarrow{Laplace} \frac{i_d}{v_d + \omega_e\lambda_q} = \frac{1}{sl_{dd}} \\ l_{qq}\frac{di_q}{dt} \approx v_q - \omega_e\lambda_d \xrightarrow{Laplace} \frac{i_q}{v_q - \omega_e\lambda_d} = \frac{1}{sl_{qq}} \end{aligned} \tag{40}$$

In addition, considering an ideal current sensing ($\boldsymbol{i}_{abc}$) with a consequent Park transformation ($\boldsymbol{i}_{dq}$), the Laplace equivalent circuit for the generic d or q axis is defined (Figure 4.6).

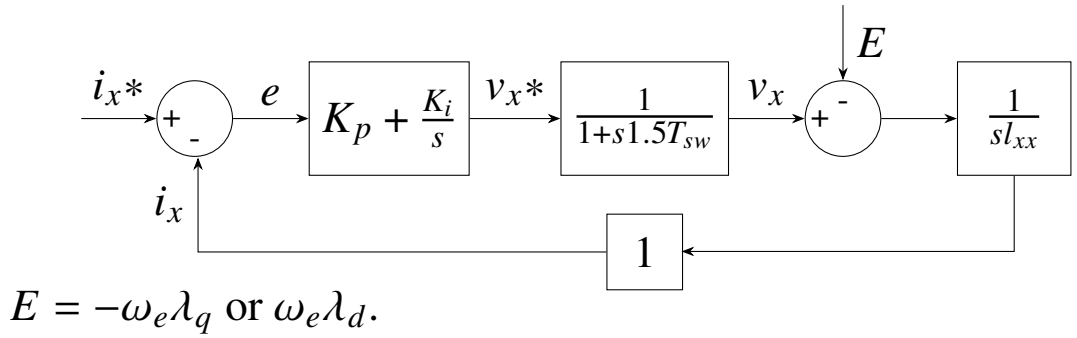

Figure 4.6: Laplace block diagram CVC.

Omitting the back-emf since it will be compensated by the feed-forward action,the open loop transfer function is:

$$G(s) = \left(\frac{K_p s + K_i}{s}\right) \cdot \left(\frac{1}{1 + s \cdot 1.5T_{sw}}\right) \cdot \left(\frac{1}{sl_{xx}}\right) \tag{41}$$

Considering that the converter's delay introduces a pole at high frequency and that the zero of the controller is placed much before this latter to ensure good phase margin, the crossover pulsation can be estimated as: $w_c = \frac{K_p}{l_{xx}}$.

In order to cross the 0dB axis with a slope of around -20dB/dec, it is a good practice to impose a crossover frequency lower than the frequency of the pole introduced by the converter (typically $f_c = \frac{f_{sw}}{10-20}$). Then, to obtain K_i once the crossover frequency and K_p are set, a good rule of thumb is to place the controller zero at least one decade before the chosen crossover frequency $f_z = \frac{f_c}{10-20}$.

Considering $\omega_c \approx \omega_b$, the gains are computed as:

- $K_{pd} = \omega_b l_{dd}$
- $K_{pq} = \omega_b l_{qq}$
- $K_{id} = K_{pd}\omega_b z_i$,with $z_i \in [0.05, 0.1]$
- $K_{iq} = K_{pq}\omega_b z_i$,with $z_i \in [0.05, 0.1]$

For completeness and only for this control topology, the frequency responses of the accurate method and the simplified one (presented just above) are compared in the Appendix (Figure A.1). In the end, the results demonstrate the very good approximation provided by the simplified method with its consequent adoption in the other below control schemes.

The pros of the CVC solutions are:

- simple control structure, both below the base speed and in flux weakening region, without the need to add external MTPV modules to ensure stability
- no flux observer needed, as for the other flux-based control approaches, with the feedforward action typically implemented exploiting the flux maps.

The cons instead are:

- poor dynamic performance compared to other types of controllers
- need to maintain a big voltage margin, hence extrapolating less power, to prevent instability in fast torque, since the PIs design is done considering the small signal approximation around a generic operating point of the considered linearized model.
- static prioritization of one axis and the PI gains' dependence on the operating point, which lead to variable dynamic performances
- for BP-CVC only → torque error at high speed, since the iron losses are not accounted.

4.4.2 Flux vector control (FVC)

Starting from the previously discussed BP-CVC (Section 4.4.1 and Figure 4.5), the passage to a BP-FVC approach is straightforward. Indeed, given the reference dq magnetizing current, the reference dq fluxes are obtained exploiting the flux-linkage maps (Section 2.2.2).

The design of the PI regulators relies again on Equation (4), where this time there is no need to express the fluxes' time derivative by means of the differential inductances since the fluxes themselves become the state variables.

$$\begin{aligned} \frac{d\lambda_d}{dt} \approx v_d + \omega_e \lambda_q &\xrightarrow{Laplace} \frac{\lambda_d}{v_d + \omega_e \lambda_q} = \frac{1}{s} \\ \frac{d\lambda_q}{dt} \approx v_q - \omega_e \lambda_d &\xrightarrow{Laplace} \frac{\lambda_q}{v_q - \omega_e \lambda_d} = \frac{1}{s} \end{aligned} \tag{42}$$

The Laplace equivalent block diagram is shown in Figure 4.7, again neglecting the stator resistance. The stator flux observer (Section 4.3) is used to provide the estimated feedback fluxes $\hat{\lambda}_{dq}$ and is modeled as ideal.

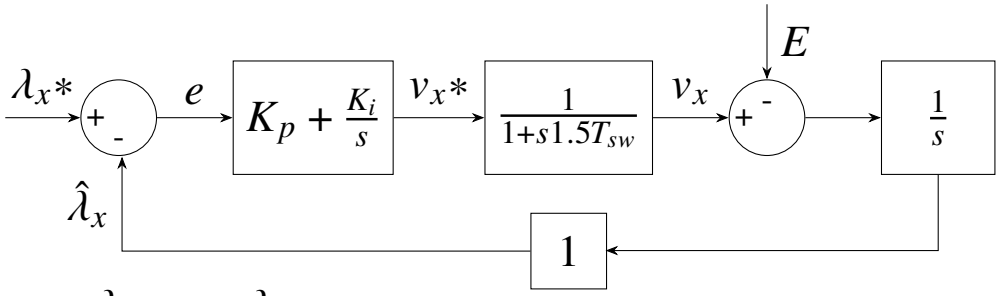

$E = -\omega_e \lambda_q$ or $\omega_e \lambda_d$.

Figure 4.7: Laplace block diagram FVC.

The open loop transfer function (43) is very similar to (41).

$$G(s) = \left(\frac{K_p s + K_i}{s}\right) \cdot \left(\frac{1}{1 + s \cdot 1.5 T_{sw}}\right) \cdot \left(\frac{1}{s}\right) \tag{43}$$

Under the same assumptions of the CVC (Section 4.4.1): the crossover pulsation can be approximated as $\omega_c = K_p$, the corresponding crossover frequency is set in the range $fc = \frac{fsw}{10-20}$, the controller's zero is placed at least one decade before this latter and $\omega_c \approx \omega_b$.

Thus, for both axes, the gains are set as:

- $K_p = \omega_b$
- $K_i = K_p \omega_b z_i$,with $z_i \in [0.05, 0.1]$

Regulators' output limits and Anti-windup are implemented as in CVC (Section 4.4.1). The feed-forward action instead relies on the stator flux observer which is able to provide an accurate flux estimate even at high speed where the use of the flux maps/$I\theta$ estimator fails (Section 4.3).

The pros of the presented BP-FVC are:

- PI gains' immunity to the differential inductances, and hence, no tuning efforts with gains shared by both axes
- as CVC, no need of additional MTPV modules for stable FW operations
- better dynamic performances compared to CVC
- lower voltage margin needed compared to CVC, hence more power extrapolated, since no small signal approximation is needed here
- no sensible torque error at high speed as in BP-CVC, since the stator flux observer ensures good estimation even at high speed
- practically current-less at high speed, where the flux observer provides the flux estimate based on the VI estimator and the current-dependent terms become negligible.

The cons are instead:

- need to implement a stator flux observer, which complicates the basic BP-CVC structure
- static prioritization of one axis, which prevents constant dynamic performance
- dynamic performance considerably lower than stator dqs approaches.

4.5 Control approaches in dqs stator coordinates

As the name suggest the torque control in dqs stator coordinates relies on the dqs voltage equations (Eq.44), that are derived from the dq voltage ones (Eq.4) by means of a rotational transformation of the load angle δ.

$$\begin{aligned}\mathbf{R}(\delta)\begin{bmatrix}v_d\\v_q\end{bmatrix} &= \mathbf{R}(\delta)R_s\begin{bmatrix}i_d\\i_q\end{bmatrix} + \mathbf{R}(\delta)\frac{d}{dt}\begin{bmatrix}\lambda_d\\\lambda_q\end{bmatrix} + \mathbf{R}(\delta)\mathbf{J}\omega_e\begin{bmatrix}\lambda_d\\\lambda_q\end{bmatrix} = \\ \begin{bmatrix}v_{ds}\\v_{qs}\end{bmatrix} &= R_s\begin{bmatrix}i_{ds}\\i_{qs}\end{bmatrix} + \mathbf{R}(\delta)\frac{d}{dt}\left(\mathbf{R}(-\delta)\begin{bmatrix}\Lambda\\0\end{bmatrix}\right) + \begin{bmatrix}0\\\omega_e\Lambda\end{bmatrix} = \\ &= R_s\begin{bmatrix}i_{ds}\\i_{qs}\end{bmatrix} + \begin{bmatrix}1 & \Lambda\end{bmatrix}\frac{d}{dt}\begin{bmatrix}\Lambda\\\delta\end{bmatrix} + \begin{bmatrix}0\\\omega_e\Lambda\end{bmatrix}\end{aligned} \tag{44}$$

The final formulation of Equation(44), emphasizes the possibility of regulating the flux-linkage magnitude exploiting the ds axis and to use the qs axis to regulate the qs current, hence the torque (DFVC/DTC, Section 4.5.1) or the load angle (FPC, Section 4.5.2). The translation of the torque request into the corresponding dqs quantities ($\mathbf{\Lambda}^*$,$\boldsymbol{i}^*_{qs}$ or $\boldsymbol{\delta}^*$) is still a critical part and differentiates the different control strategies.

As for the controls in the rotor dq approach (Section 4.4), the use of PI regulators is still preferred, with the output of each axis regulator setting the reference voltage. The feedback variables $\hat{\Lambda}$,$\hat{\delta}$,$\hat{Te}$ or $\hat{i_{qs}}$ are estimated with the flux observer (Section 4.3) considered ideal in the controller design. Regarding the regulation, the same requirements of stability and quickness of the control action have to be ensured, with the PIs that are combined with the feed-forward compensation of the back-emf together with the Anti-windup clamping method.

In general, in steady-state conditions, the ds axis just has to compensate for the stator resistance. Hence, a little amount of voltage is enough to regulate the flux-linkage amplitude. As a rule of thumb $v_{lim,ds} \in \pm[3R_{s0}I_{max}, 6R_{s0}I_{max}]$.
The back-emf instead is concentrated on the qs axis. This means that at steady-state and for high-speed conditions (low i_{qs}), almost all the qs axis voltage is used to compensate the back-emf. Therefore $v_{lim,qs} = \pm\sqrt{v_{lim}^2 - v_{ds}^{*2}} \approx \pm v_{lim}$.

In dynamic conditions, the torque regulation from generation to motoring with respect to the motoring to generation case presents asymmetries. Considering the positive speed case, in the passage from generation to motoring the intent is to increase i_{qs}, Te or δ, asking therefore for a positive v^*_{qs}. However, due to the back-emf compensation just a negligible voltage can be used to regulate the controlled quantity without overcoming the qs axis positive voltage limit. Instead, in the passage from generation to motoring the PI asks for a negative v^*_{qs}, therefore before reaching the lower qs voltage limit up to two times v_{lim}(in FW) can be used to regulate the variable.

4.5.1 Direct flux vector control (DFVC) and SVM-Direct torque control (SVM-DTC)

The historical dqs controllers are the DFVC and SVM-DTC. In both, there is the need to get a flux amplitude reference $\Lambda*$ to operate the ds axis regulation. One way to proceed was proposed in [6], where the input torque request Te^*_{IN} is used to find the corresponding MTPA flux amplitude that is finally bounded to account for the BP-flux limit computed as in Figure 4.5.

The design of the ds axis PI regulator in Figure 4.8 is based on the ds state-space equation (45) derived from (44), neglecting the stator resistance contribution. In the end, the design is practically identical to the FVC one in Figure 4.7, apart from the absence of the back-emf term which consequently implies the absence of any feed-forward term.

$$\frac{d\Lambda}{dt} \approx v_{ds} \xrightarrow{Laplace} \frac{\Lambda}{v_{ds}} = \frac{1}{s} \tag{45}$$

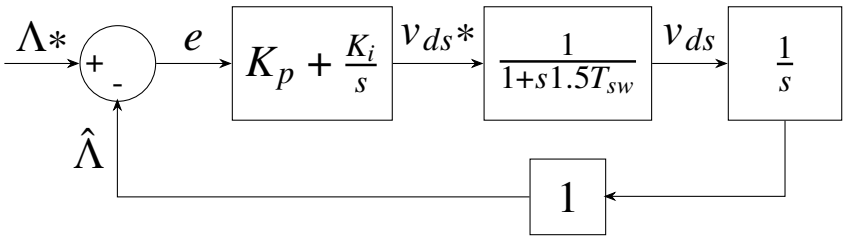

Figure 4.8: Laplace block diagram ds-axis DFVC/DTC/FPC.

Hence, the PI gains are set as:

- $K_p = \omega_b$
- $K_i = K_p \omega_b z_i$,with $z_i \in [0.05, 0.1]$

Designing the qs axis for the DFVC, means considering the i_{qs} state-space equation (46),obtained from (40) applying a rotational transformation with rotational angle δ, assuming steady-state conditions and neglecting the v_{ds} voltage [7].

$$\begin{aligned} l_{qs}\frac{di_{qs}}{dt} \approx v_{qs} - \omega_e \Lambda \xrightarrow{Laplace} \frac{i_{qs}}{v_{qs} - \omega_e \Lambda} = \frac{1}{s l_{qs}} \text{ ,with} \\ l_{qs} = \frac{2 l_{dd} l_{qq}}{l_{dd} + l_{qq} - \left(l_{qq} - l_{dd}\right) \cos\left(2\delta\right)} \end{aligned} \tag{46}$$

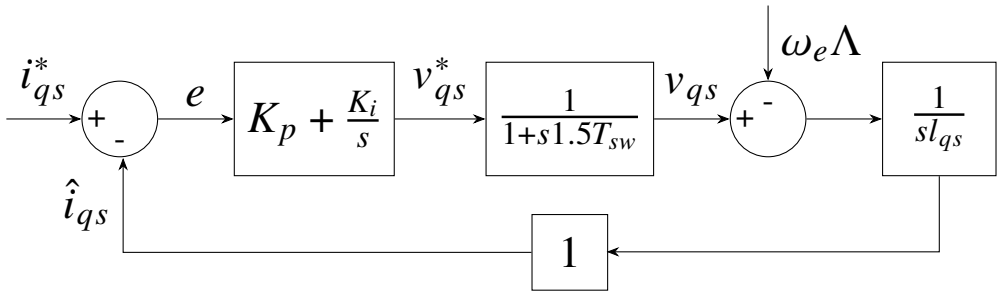

Figure 4.9: Laplace block diagram qs-axis DFVC.

The similarity of (46) with (40) results in the PI gains:

- $K_p = \omega_b l_{qs}$
- $K_i = K_p \omega_b z_i$,with $z_i \in [0.05, 0.01]$

To get the estimated current $\hat{i}_{qs}$, the sampled currents i_{abc} are transformed in the dqs frame by means of a Park transformation (A.5),using as rotational angle θ (Figure 1.3).

Designing the qs axis for the DTC instead,requires combining (2) with (46),again neglecting the v_{ds} contribution to finally get:

$$\frac{2l_{qs}}{3pp\Lambda}\frac{dTe}{dt} \approx v_{qs} - w_e\Lambda \xrightarrow{Laplace} \frac{Te}{v_{qs} - w_e\Lambda} = \frac{3pp\Lambda}{s2l_{qs}} \tag{47}$$

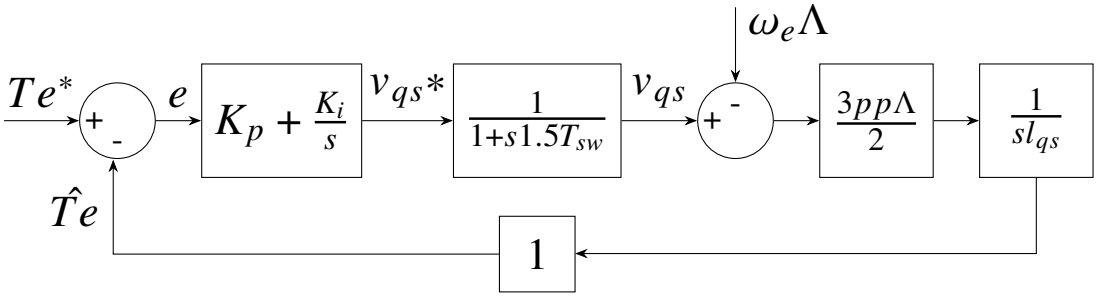

Figure 4.10: Laplace block diagram qs-axis DTC.

Therefore here:

- $K_p = \omega_b \frac{2l_{qs}}{3pp\hat{\Lambda}}$
- $K_i = K_p\omega_b z_i$,with $z_i \in [0.05, 0.1]$

The estimated torque is obtained from Equation(2), exploiting $\hat{i}_{qs}$ and $\hat{\Lambda}$.

In order to find the reference torque Te^* or qs axis current $i_{qs}*$ exploiting (2), first the input desired torque Te^*_{IN} is bounded to account for the set BP-flux limit and current limit (Figure 4.5). Then, an additional limitation is required to respect the MTPV limits, in contrast with BP-CVC and BP-FVC, where the BP-flux limitation is able alone to set the correct torque reference capable of driving the motor in FW region.

The additional MTPV module consists in a load angle PI regulator, whose design is critical. The idea is to compare the maximum load angle along the MTPV acting as reference with the current one estimated by the flux observer. Working with the absolute values of such angles, means having a negative error when crossing the MTPV profile and hence activating the control to further limit the torque limit imposed by the BP-flux one (Figure 4.5).

For positive errors, the MTPV profile is not crossed, the MTPV control must be disabled and the torque limit coincides with the one imposed by the flux one Te_{lim}. Therefore, the output of the PI must be bounded to stay in the range $[-Te_{lim}, 0]$.

The additional reduction of the torque limit can be seen equivalently as a reduction of the maximum qs current (Eq.2) as proposed in [6]. In the same article, a preliminary tuning procedure for DFVC's load angle regulator is presented, where, assuming ideal inverter and observer and considering the qs axis final expression in Equation(44), the block diagram in Figure 4.11 is obtained.

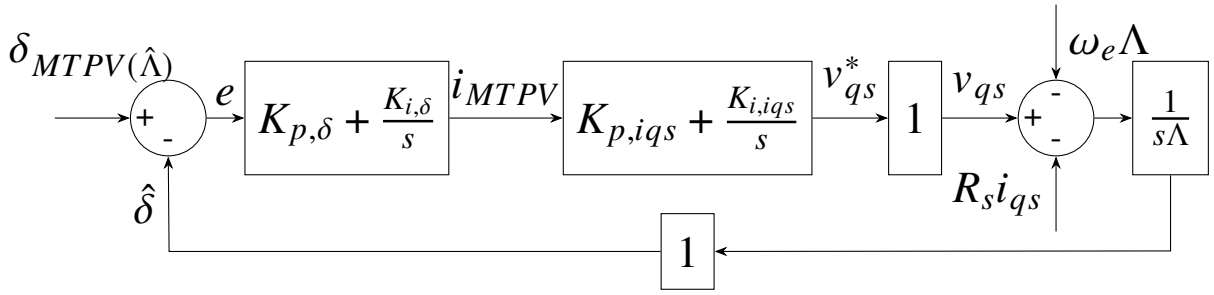

Figure 4.11: Laplace block diagram MTPV limiter DFVC.

Since the integral actions vanish at high frequencies, the crossover frequency/bandwidth can be approximated as:

$$\omega_b \approx \omega_c \approx \frac{K_{p,\delta} K_{p,iqs}}{\Lambda} \tag{48}$$

However, the bandwidth choice is critical and is often found heuristically. For the IPM machine under investigation for example, the bandwidth of the MTPV limiter is set close to that one of the ds and qs axes. The MTPV limiter gains are then online updated as:

- $K_{p,\delta} = \frac{\omega_b \hat{\Lambda}}{K_{p,iqs}}$
- $K_{i,\delta} = K_{p,\delta} \omega_b z_i$,with $z_i \in [0.05, 0.1]$

For the DTC's MTPV limiter, the current i_{MTPV} in Figure 4.11 is substituted by the torque Te_{MTPV} since downstream there is a torque PI regulator. As a consequence, the MTPV regulator gains can be obtained as:

- $K_{p,\delta} = \frac{\omega_b \hat{\Lambda}}{K_{p,Te}}$
- $K_{i,\delta} = K_{p,\delta} \omega_b z_i$,with $z_i \in [0.05, 0.1]$

The advantages that the presented DFVC and DTC offer are:

- no need of significant LUTs to maintain the torque regulation linearity apart from the MTPA and the MTPV profiles, hence the control becomes extremely robust and easily adaptable for all the three-phase AC machines [6]
- decoupling the torque and flux production allows to the qs axis regulator the use of almost all the voltage made available by the inverter to regulate the torque with consequent dynamic performances sensibly higher compared to the rotor dq approaches
- stator flux magnitude regulation is independent from the operating point
- typically lower voltage margin with respect to rotor dq approaches
- practically current-less at high speed, where the flux observer provides the flux estimate based on the VI estimator and the current-dependent terms become negligible.

The disadvantages of these approaches are instead:

- PI gains of the qs axis operating-point dependent, with consequent variable dynamic performances
- MTPV limiter design is critical and time-consuming
- implementation of a stator flux observer is mandatory
- as all the stator dqs control approaches, they exhibit an asymmetric behaviour during fast torque reversals.

4.5.2 Flux polar control (FPC)

The FPC came out from the attempt of overcoming the main drawback of the DFVC and DTC. The intent is to maintain the flux amplitude regulation in the ds axis, however, addressing the qs axis' task to the regulation of the load angle, which intrinsically acts as MTPV limiter. Two main approaches are possible.

The first one was proposed in [7] and consists in the implementation of a load angle LUT, which receives in input the reference torque (bounded considering the BP flux limit as in Figure 4.5) and the flux both in p.u.. The computation of such map starts determining the dq current and the associated dq flux between the MTPV and the MTPA curves, where normally the machine has to work. Once the torque and the flux maps of this region are extracted, the p.u. notation is exploited to get a regular domain. Afterwards, just interpolating these two maps the load angle reference is easily obtained.

Alternatively, a BP-FPC can be implemented starting from the BP-FVC simply computing the load angle reference from the obtained dq reference flux.

For the closed-loop design, the qs-axis voltage equation is considered (Eq.44).

$$\Lambda \frac{d\delta}{dt} \approx v_{qs} - \omega_e \Lambda \xrightarrow{Laplace} \frac{\delta}{v_{qs} - \omega_e \Lambda} = \frac{1}{s\Lambda} \tag{49}$$

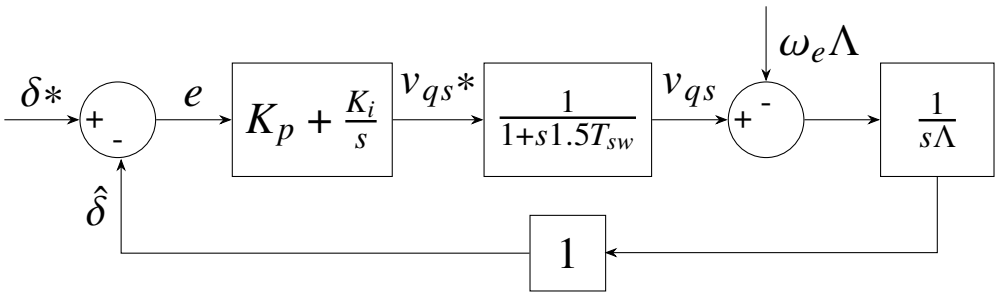

Figure 4.12: Laplace block diagram qs-axis FPC.

Hence, the PI gains are set as:

- $K_p = \omega_b \hat{\Lambda}$
- $K_i = K_p \omega_b z_i$,with $z_i \in [0.05, 0.1]$

The main benefits of the FPC are:

- the PI gains independence from the differential inductances which results in constant performances for all the operating points and easy tuning procedures
- the decoupling of the two axes, allows the qs axis regulator the use of almost all the voltage made available by the inverter, with consequent dynamic performances sensibly higher compared to the rotor dq approaches
- MTPV limiter already implemented in the load angle LUT
- typically the lowest voltage margin among the PI-based controllers, with the consequent highest power extrapolation
- practically current-less at high speed, where the flux observer provides the flux estimate based on the VI estimator and the current-dependent terms become negligible.

The drawbacks are instead:

- the torque regulation linearity has to be guaranteed with the load angle LUT and it is not automatic as in DFVC and DTC
- as all the stator dqs control approaches, they exhibit an asymmetric behaviour during fast torque reversal tests.

4.6 Predictive controllers

In the case the parameters of the inverter and of the machine are well known, as usually happens in the automotive industry, the possibility of implementing an accurate flux observer makes possible the adoption of ultrafast predictive controllers, that do not rely on PI regulators.

4.6.1 Model predictive control (MPC)

This type of controller is based on the optimization of a cost function J, deciding at each step the optimal state on the $\alpha\beta$ plane among the eight possible states of a 2-levels VSI. The state is set at each sampling period and with this setup the equivalence $f_s = f_{sw}$ is lost since the control may apply the same reference state for consecutive sampling periods.

This solution is particularly used in heavy industrial applications when there is the exigency to reduce the average switching frequency to increase the lifespan of the machine. However, it is still uncommon for traction applications and for this reason it is not treated in this text.

4.6.2 Deadbeat control (DB)

The aim of a deadbeat regulator is to find the input signal able to drive the system's output to its desired value in the fastest way possible. The idea is to predict the reference voltages ($\boldsymbol{v}^*_{\alpha\beta}$,$\boldsymbol{v}^*_{dq}$ or $\boldsymbol{v}^*_{dqs}$), estimating all the flux-linkage related quantities at the next sampling time, thanks to the backward integration in the flux observer.
The estimation of the currents instead is critical since they depend on the differential inductances that are difficult to predict. Therefore, usually only the controls that do not rely on state-space equations with currents are implemented:

- $\alpha\beta$ FVC
- dq FVC
- dqs FPC

In particular, the discretized machine models shifted by one sampling time (Eq.50) are considered. The actual sampled current as well as the actual estimated speed (Section 4.2) are used instead of the predicted values.

In order to account for the inverter losses, the addition of the On-state resistance in series with the stator resistance together with the dead time effect (sec:3.1.2) are considered. In addition, since the effectiveness of the duty cycles/voltages arises one sampling time after the application, the following considerations are done:

- $d_x^* = d_x^{k+1}$
- $v_x^* = v_x^{k+1}$
- $i_x^* = i_x^{k+2}$
- $\Lambda^* = \Lambda^{k+2}$, $\lambda_x^* = \lambda_x^{k+2}$, $\delta^* = \delta^{k+2}$

$$
\begin{aligned}
v_\alpha^* &= R_{tot} i_\alpha^k + \frac{\lambda_\alpha^* - \lambda_\alpha^{k+1}}{Ts} + v_{dt,\alpha}^k & v_\beta^* &= R_{tot} i_\beta^k + \frac{\lambda_\beta^* - \lambda_\beta^{k+1}}{Ts} + v_{dt,\beta}^k \\
v_d^* &= R_{tot} i_d^k + \frac{\lambda_d^* - \lambda_d^{k+1}}{Ts} - w_e^k \lambda_q^{k+1} + v_{dt,d}^k & v_q^* &= R_{tot} i_q^k + \frac{\lambda_q^* - \lambda_q^{k+1}}{Ts} + w_e^k \lambda_d^{k+1} + v_{dt,q}^k \\
v_{ds}^* &= R_{tot} i_{ds}^k + \frac{\Lambda^* - \Lambda^{k+1}}{Ts} + v_{dt,ds}^k & v_{qs}^* &= R_{tot} i_{ds}^k + \Lambda^{k+1} \frac{\delta^* - \delta^{k+1}}{Ts} + w_e^k \Lambda^{k+1} + v_{dt,qs}^k
\end{aligned}
\tag{50}
$$

with $i_x^k \approx i_x^{k+1}$, $\omega_e^k \approx \omega_e^{k+1}$, $v_{dt,x}^k \approx v_{dt,x}^{k+1}$.

Going to the pros of the deadbeat regulators:

- outstanding performances, with possibly a requested torque rate one order of magnitude higher than the one with stator dqs controllers
- due to the lack of PI regulators, there are no tuning procedures about the control.

As cons instead:

- the need to implement an ultra-precise stator flux observer, otherwise, almost instantaneous loss of control or consistent steady-state error

- even though all the parameters of the e-drive are known, the sensitivity to model uncertainties and parameters variations is critical, resulting in a much less robust solution in this sense, compared to PI-based ones.
- for DB-FPC only, the asymmetric behavior in dynamic conditions typical of dqs controllers comes out clearly, making $\alpha\beta$ and dq FVC still a preferred solution for deadbeat regulators.

4.7 Closed-loop tests of the complete e-drive

In order to test the presented control strategies, each control topology is implemented inside a different MCU and added upstream (one for time) of the VSI-SM block, considering as machine model only the flux-based dq model with losses for time reasons.

To speed up the simulations, the PWM modulator is bypassed and the average behaviour given by the duty cycles is considered, neglecting the PWM characteristic ripple which it is not relevant for the control performance evaluation.

To significantly stress the controls, it is decided to drive the machine under fast torque reversals, passing from the motoring peak current MTPS profile to the generation counterpart.

The general settings are summarized in Table 5. However, the reference torque rate Te^*_{slope}, the reversal frequency of the latter $f_{Te^*,rev}$ and the safety coefficient on voltage kv_{lim} are imposed differently for each control in the way they properly stress the regulations and such that to avoid significant instability marks. About the PIs gains, they are set as defined in Sections 4.4 and 4.5.

Table 5: Test conditions MCU-VSI-SM simulations.

Settings			
Initial d-axis flux linkage	λ_{d0}=λ_{PM}	0.0558	Vs
Initial q-axis flux linkage	λ_{q0}	0	Vs
Magnetizing current limit	$I_{LIM} = I_{max,IPM}$	1403.8	Apk
Stator current limit (EM-based CVC)	$Is_{LIM} = I_{max,IPM}$	1403.8	Apk
Initial mechanical speed	n_0	0	rpm
Mechanical speed enable time	t_ω	0.3	s
Final mechanical speed	n_{max}	18.1e3	rpm
Acceleration	a	6e3	rpm/s
Initial desired torque	Te^*_0	0	Nm
Torque enable time	t_{Te*}	0.05	s
Slope desired torque	Te^*_{Slope}	Variable	Nm/s
Reversal frequency desired torque	$f_{Te^*,rev}$	Variable	Hz
Maximum desired torque	$Te_{MTPSm(0)}$	431.4	Nm
Minimum desired torque	$Te_{MTPSg(0)}$	-431.4	Nm
DC-link voltage	v_{dc}=v_{dc0}	230	V
SiC-MOSFET junction temperature	T_j	100	° C
Stator temperature	T_{Cu}=T_{Cu0}	120	° C
Dead time	t_{dt}	500	ns
Safety coefficient on voltage	k_{vdc}/k_{vlim}	Variable	/
Switching frequency	f_{sw}	1e4	Hz
Controller crossover frequency	f_c=$f_{sw}/20$	500	Hz
Controller zero frequency	f_z=$f_c/10$	50	Hz
Phase margin PTO	PM_{PTO}	60	°
PTO crossover frequency	$f_{c,PTO}$	35	Hz
Stator flux observer cut-off frequency	$f_{cut,OBS}$	20	Hz
Simulation time	t_{sim}	4	s
Solver details			
Simulink solver	Ode45		
Plecs solver	RADAU		
Min step size	auto		
Max step size	$\frac{1}{10 \cdot f_{sw}}$ s		

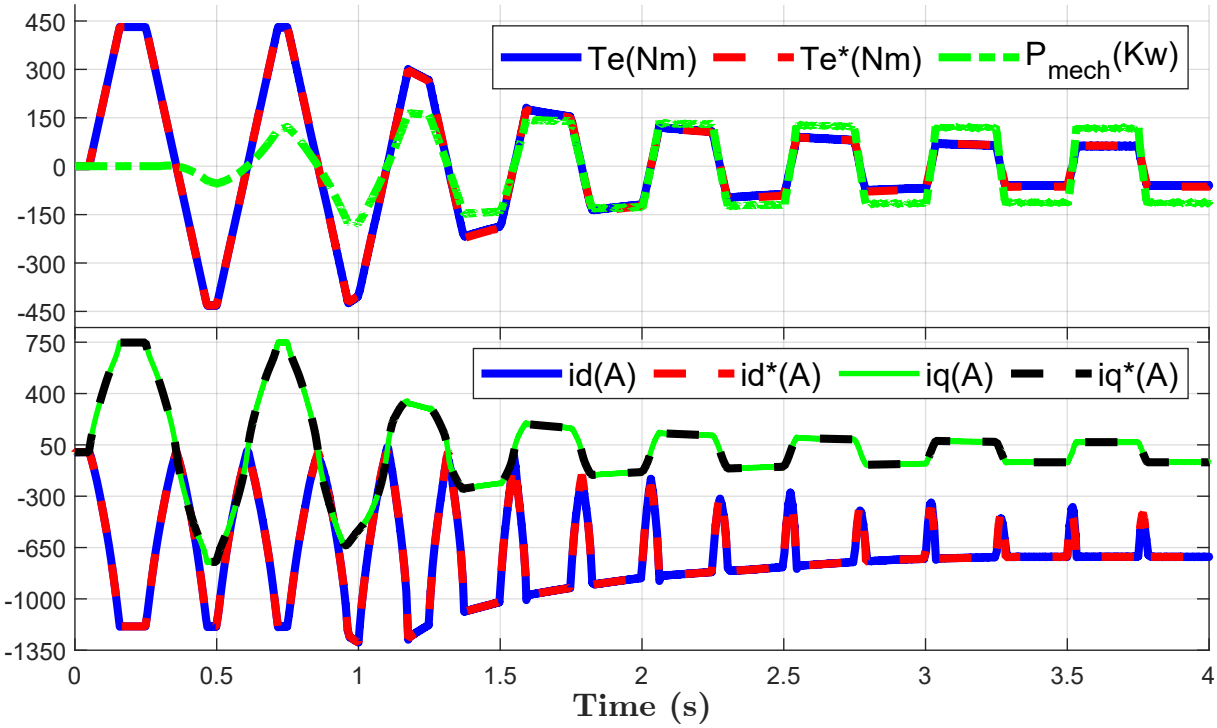

Settings: $k_{vlim} = 0.86, Te^*_{Slope} = 4.0e + 0.3Nm/s, f_{Te*,rev} = 2Hz$

Figure 4.13: Torque and *dq* current dynamics BP-CVC.

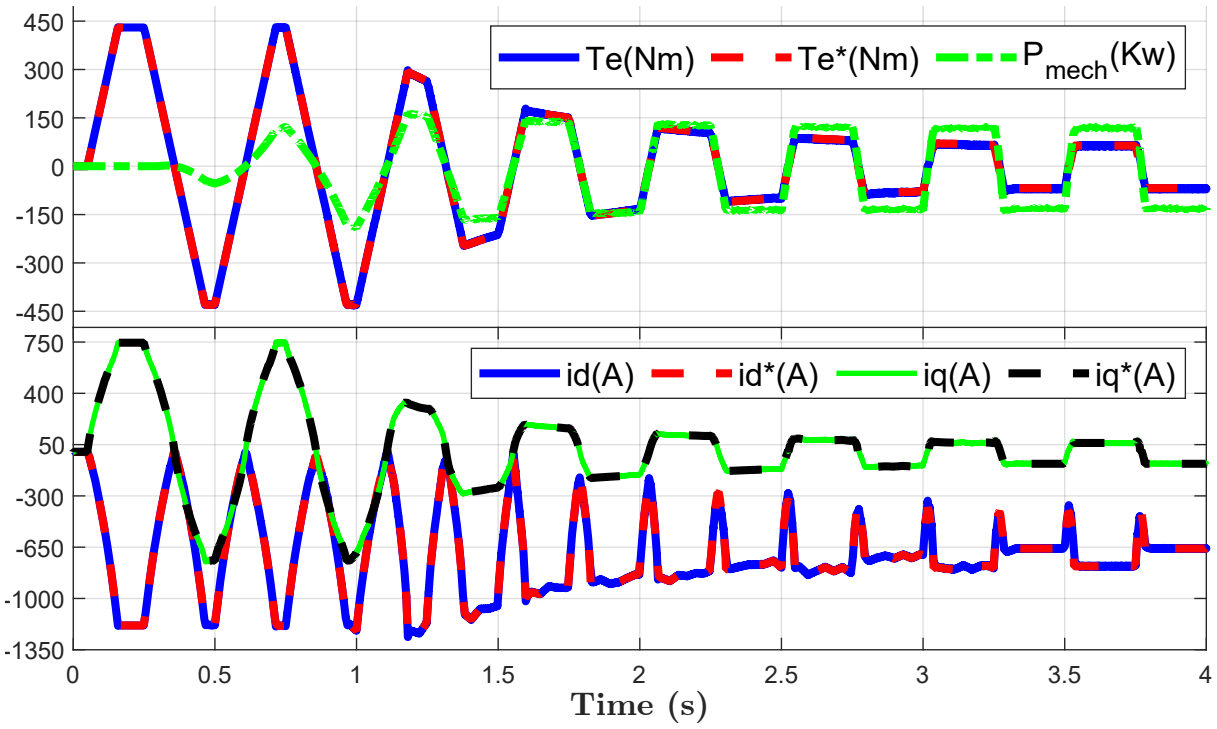

Settings: $k_{vlim} = 0.9, Te^*_{Slope} = 4.0e + 0.3Nm/s, f_{Te*,rev} = 2Hz$

Figure 4.14: Torque and *dq* current dynamics LUTs-based-CVC

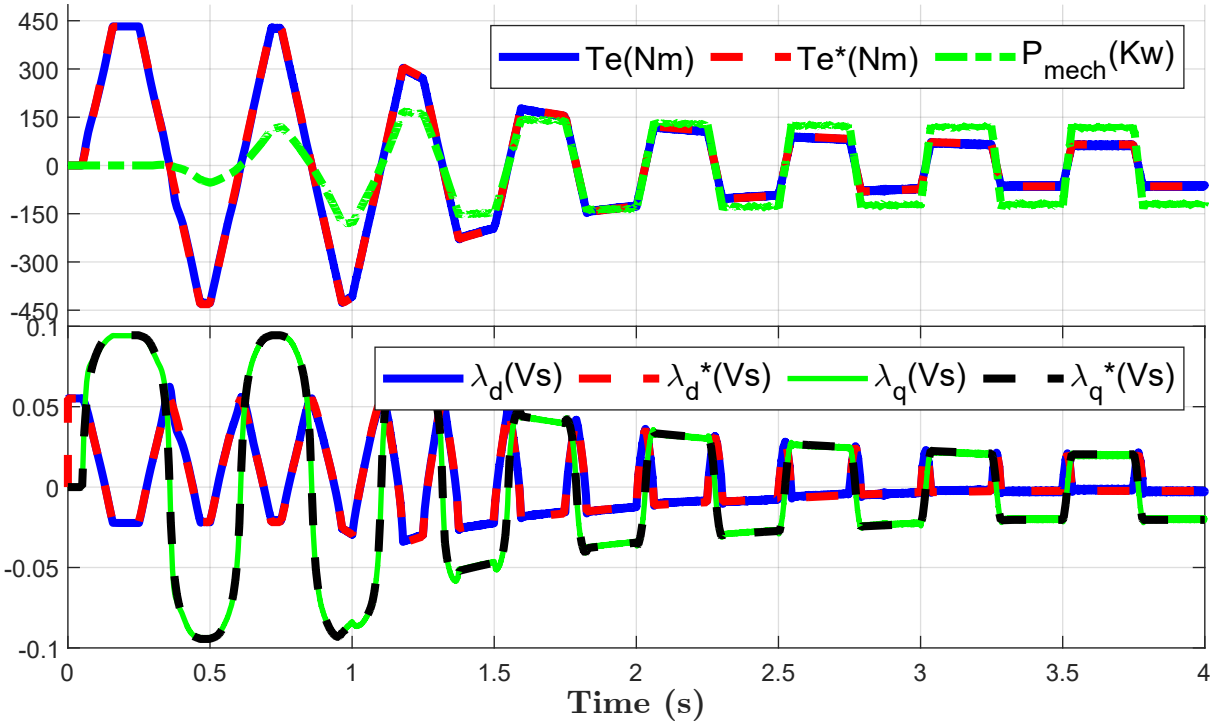

Settings: $k_{vlim} = 0.88, Te^*_{Slope} = 4.0e+03Nm/s, f_{Te*,rev} = 2Hz$

Figure 4.15: Torque and *dq* flux dynamics BP-FVC.

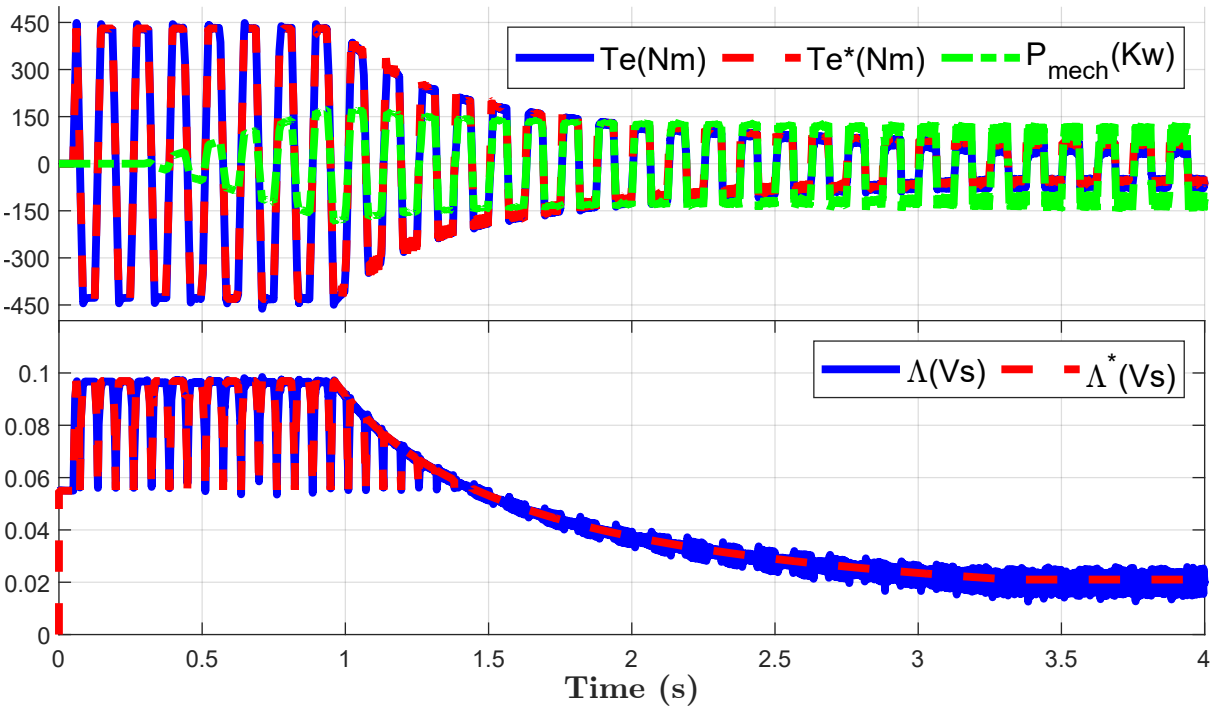

Settings: $wb_\delta = 4wb_{ds/qs}, k_\delta = 0.85, k_{vlim} = 0.9, Te^*_{Slope} = 4e+4Nm/s, f_{Te*,rev} = 8Hz$

Figure 4.16: Torque and flux dynamics DTC-SVM.

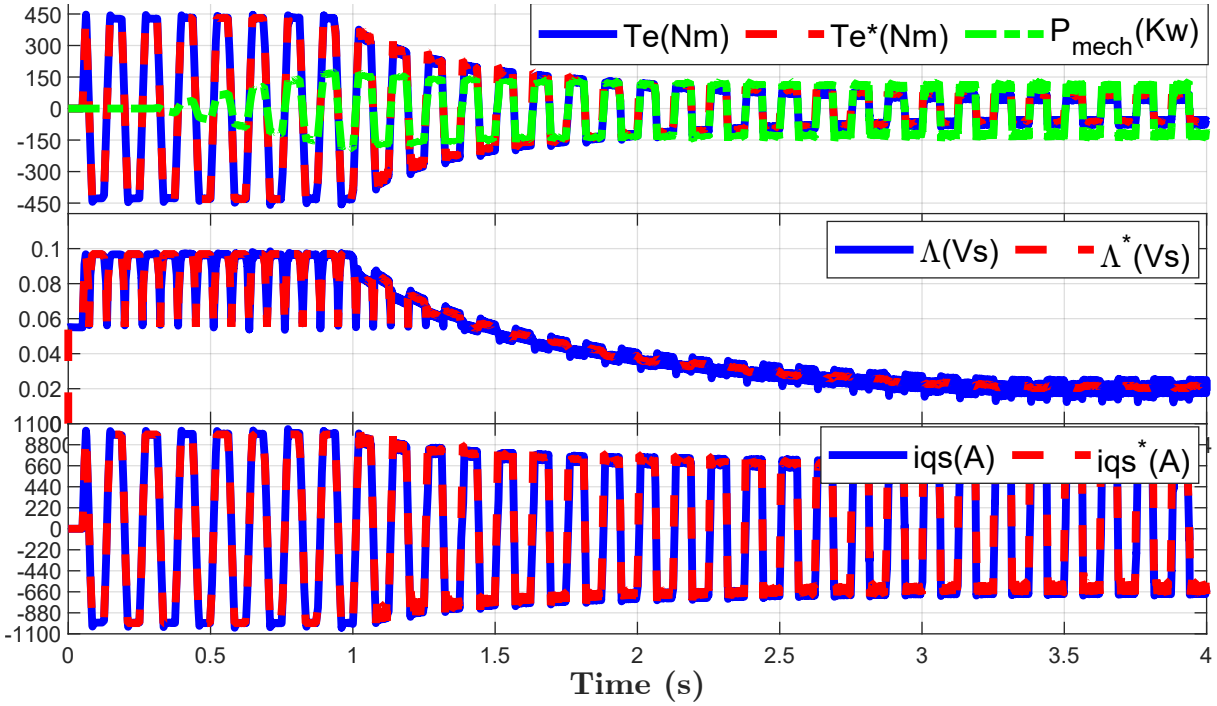

Settings: $wb_{\delta} = wb_{ds/qs}, k_{\delta} = 0.85, k_{vlim} = 0.9, Te^{*}_{Slope} = 4e + 4Nm/s, f_{Te*,rev} = 8Hz$

Figure 4.17: Torque,flux and qs current dynamics DFVC.

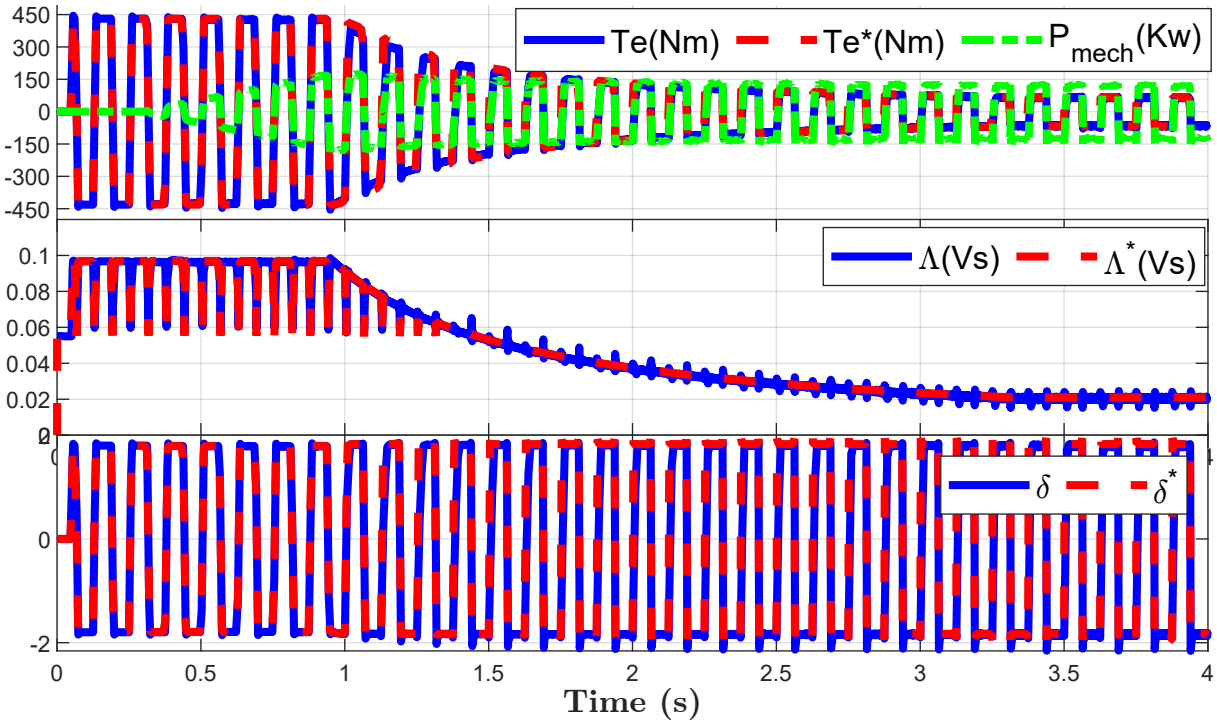

Settings: $k_{vlim} = 0.9, Te^{*}_{Slope} = 8.0e + 04Nm/s, f_{Te*,rev} = 8Hz$

Figure 4.18: Torque,flux and load angle dynamics LUTs-based-FPC.

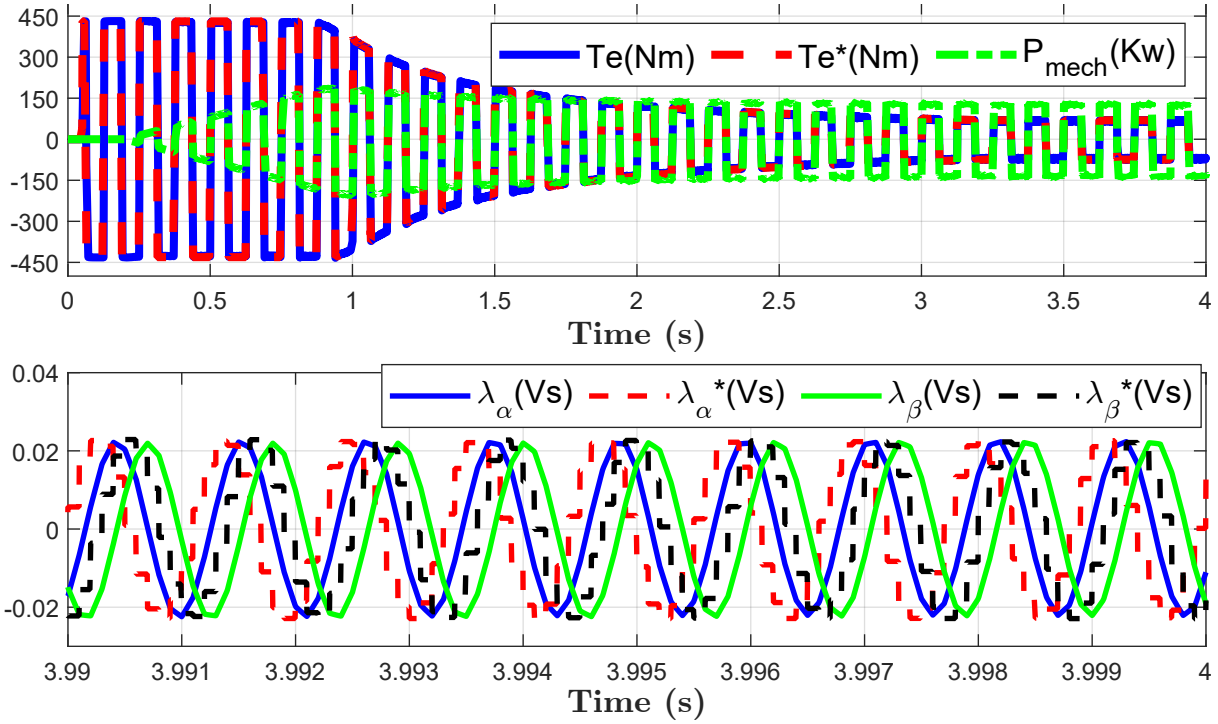

Settings: $k_{vlim} = 0.95, Te^*_{Slope} = 4.0e+05 Nm/s, f_{Te*,rev} = 8Hz$

Figure 4.19: Torque and $\alpha\beta$ flux dynamics Deadbeat-$\alpha\beta$FVC.

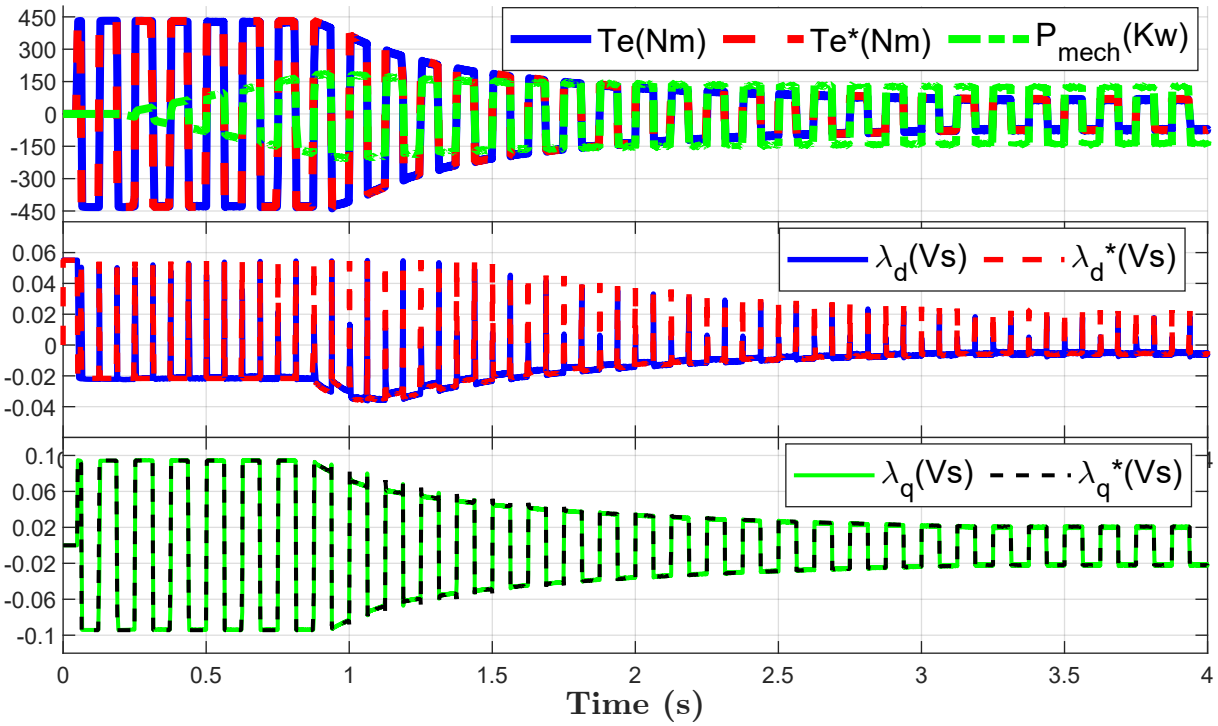

Settings: $k_{vlim} = 0.95, Te^*_{Slope} = 4.0e+05 Nm/s, f_{Te*,rev} = 8Hz$

Figure 4.20: Torque and dq flux dynamics Deadbeat-dqFVC.

Chapter 5:
Texa Motor

The AFSMs are much less common machines in which the magnetic flux is concentrated along the axis rather than being radial. Several topologies exist also here, mainly depending on the number of stator and rotor plates [8].

The Texa machine considered here is a high-performance, light-weight, double-rotor layout AFPM traction motor. For confidentiality reasons, all the results are expressed in per-unit, adopting as base values:

- i_{base} = maximum phase current (data-sheet value)
- λ_{base} = maximum d-axis flux @cold (Matlab-extrapolated)
- L_{base}= maximum q-axis inductance @cold (Matlab-extrapolated)
- l_{base} = maximum d-axis differential inductance @cold (Matlab-extrapolated)
- $\lambda_{m,base}$ = maximum PM flux @cold (Matlab-extrapolated)
- Tm/e_{base} = peak mechanical torque (data-sheet value)
- n_{base} = maximum mechanical speed (data-sheet value)
- P_{base} = peak mechanical power (data-sheet value)

5.1 Experimental flux and torque maps extrapolation

In the data-sheet of the machine, the company already provides FEA-evaluated flux maps. However, looking for an accurate control of the machine, the experimental evaluation of the flux maps was mandatory.

In addition, the heavy presence of permanent magnet potentially makes the flux maps highly sensitive to the magnets temperature. Therefore, a double characterization of the machine it is necessary. One obtained in 'cold' rotor condition, hence without heating and controlled thermal conditions, and the other one in 'hot' rotor condition, with a warm-up procedure and controlled thermal conditions. The adopted procedures follow the ones explained in [9] and [10], respectively for the 'cold' and 'hot' cases.

The idea is to control the MUT with a simple CVC (4.4.1), imposing in sequence a mesh of points in the $\mathbf{I}_{dq}$ plane, while it is speed-driven at constant speed by a servo machine. Then, exploiting the steady-state form of the dq voltage equations (Eq.(4)), measuring speed, phase currents and measuring or estimating the phase voltages, the dq flux and the corresponding electromagnetic torque maps (Eq.1) are obtained. Eventually, as in this case, the mechanical torque can be sensed to verify the accuracy of the results.

The DM is speed-controlled and force the MUT to rotate at an imposed speed. The speed choice is critical and it is a trade-off between having a good signal-to-noise ratio (at high speed) and small iron losses effects (at low speed). Here, it was set to 250 rpm.

For symmetry reasons, the investigated area on the current plane includes the first two quadrants with a little extension to small negative values of i_q to avoid boundary effects. The Figure 5.1 below shows the grid of tested currents in the two cases.

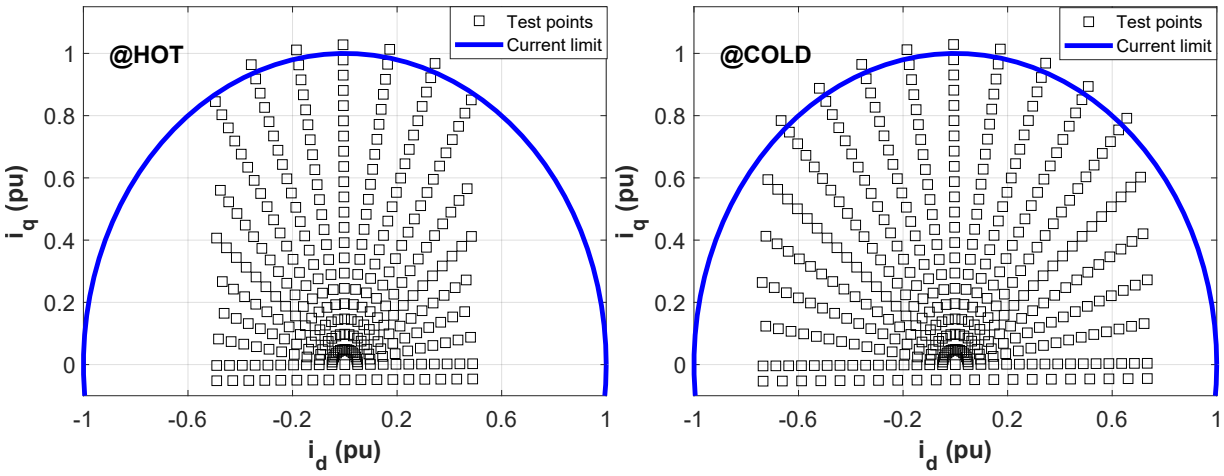

Figure 5.1: Grid of dq currents tested in the flux maps extrapolation.

To note that, under the Texa specifications, i_d was limited way before the maximum phase current constraint and in a different ways according to the stator winding temperature, to avoid the demagnetization of the magnets.

In addition, to compensate for the voltage drop on the stator resistance as well as to mitigate any stator resistance variation due to temperature variation, three points in sequence (M1-G-M2) are tested for each operating point in the mesh of currents, reversing two times i_q. In the end of each motoring-generation-motoring sequence the magnets flux estimate is done controlling the MUT with zero current.

All the measures (voltage, speed, current and torque) are logged at least for a mechanical revolution, after the steady-state operations for speed and currents are reached. The mechanical round measurements are then averaged to cancel any periodicity due to space and time harmonics in addition to mechanical asymmetry.

Moreover, a strain gauge torque transducer was used to compare the sensed torque with the electromagnetic one computed from the obtained flux maps . The plot in Figure 5.2 shows such comparisons in per-unit with respect to the base torque.

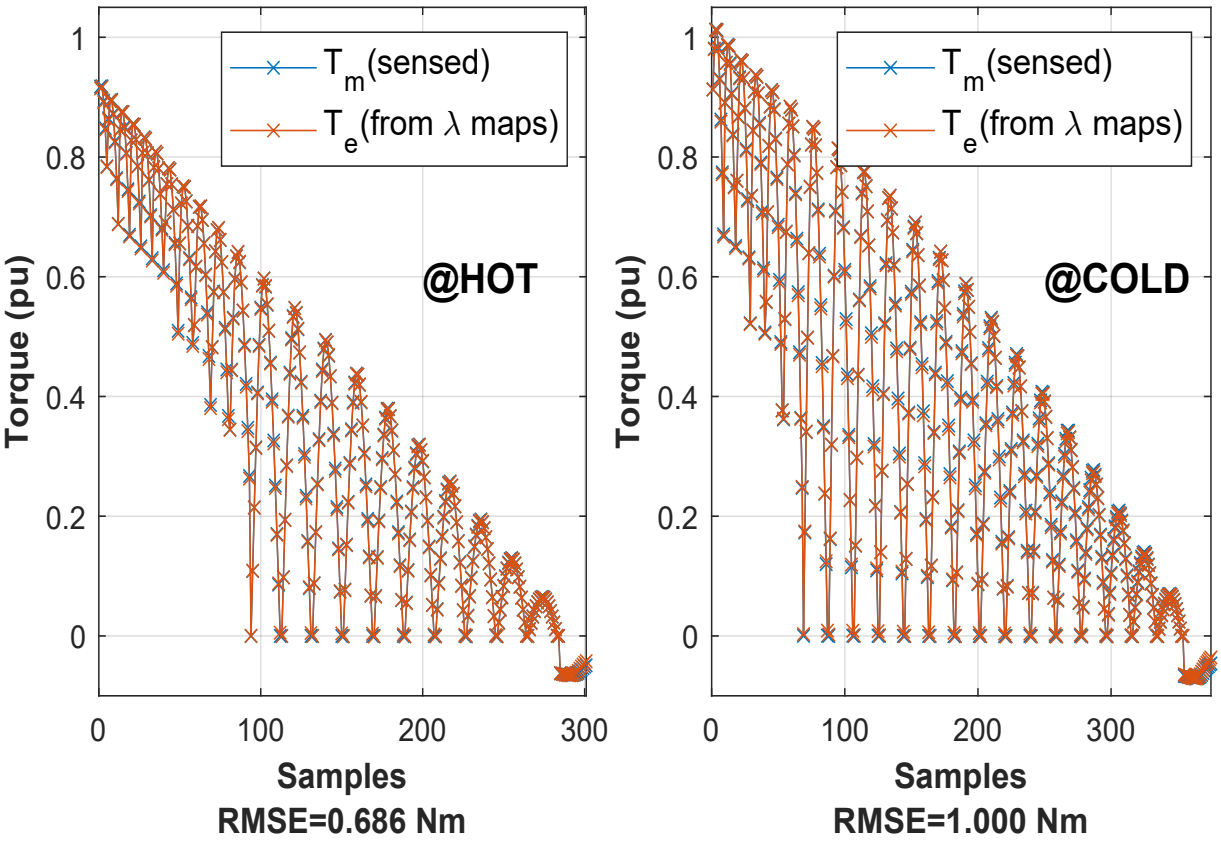

Figure 5.2: Measured and computed torque in the flux maps extrapolation.

Verified the accuracy of the results, the flux linkage maps (Section 2.2.2) and the torque maps (Section 2.2.5) are extrapolated (Figure 5.3) with the Matlab command *scatteredinterpolant*, after a regular *dq* currents domain is defined.

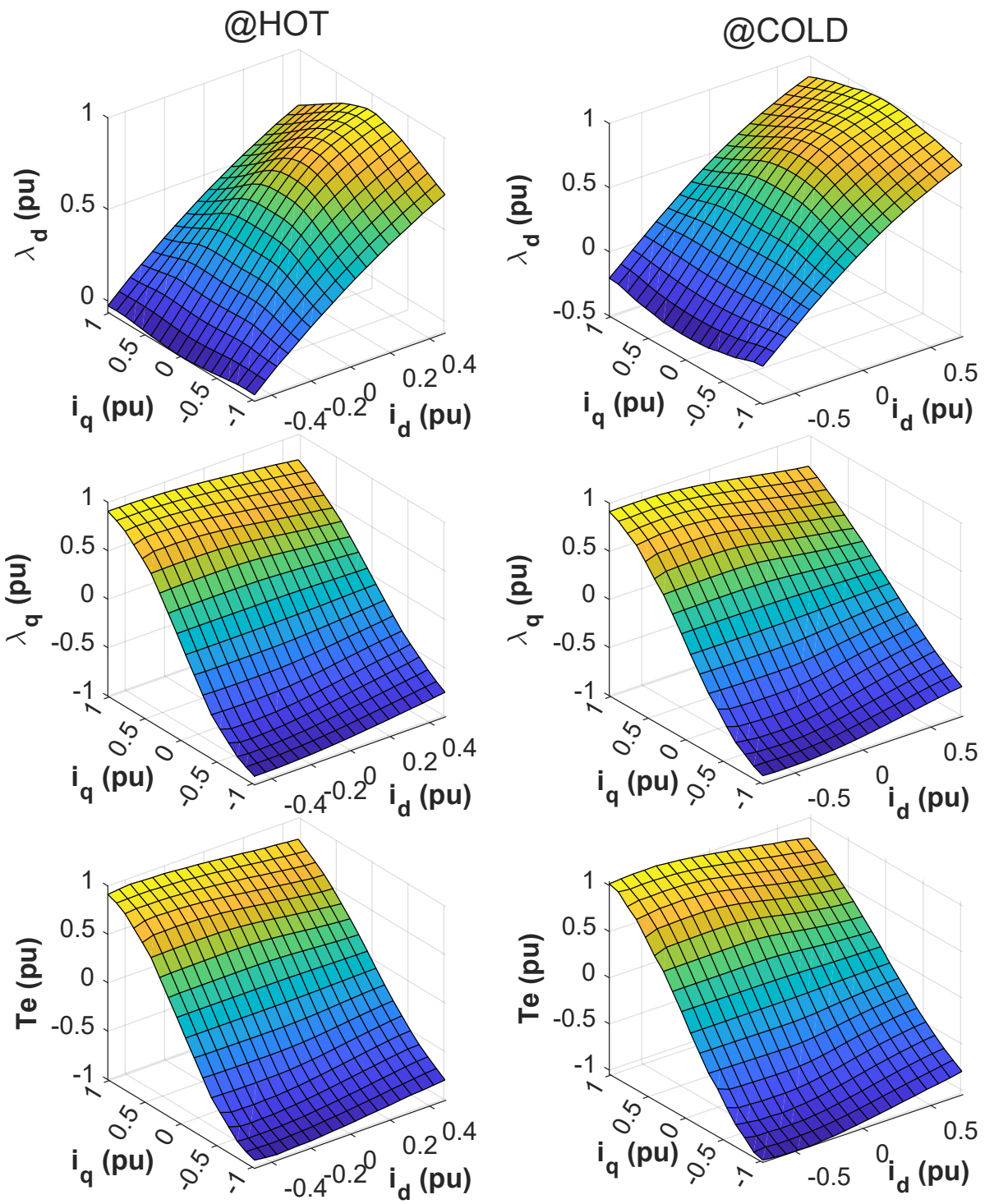

Figure 5.3: Flux and Torque maps in the $\mathbf{I}_{dq}$ plane.

5.2 Differential inductances, MTPA, MTPV and MTPS

Directly from the flux maps, the differential inductance maps are computed with the Matlab command *gradient* and reported in the dq current plane, replacing $\boldsymbol{i}_{m,dq}$ with $\boldsymbol{i}_{dq}$ in Equation (13).

The determination of the approximated differential inductances is almost mandatory. Indeed, except for the FVC (Section 4.4.2) and the FPC (Section 4.4.2), in all the other PI-based control strategies, the differential inductances are used to update the PI gains based on the operating points.

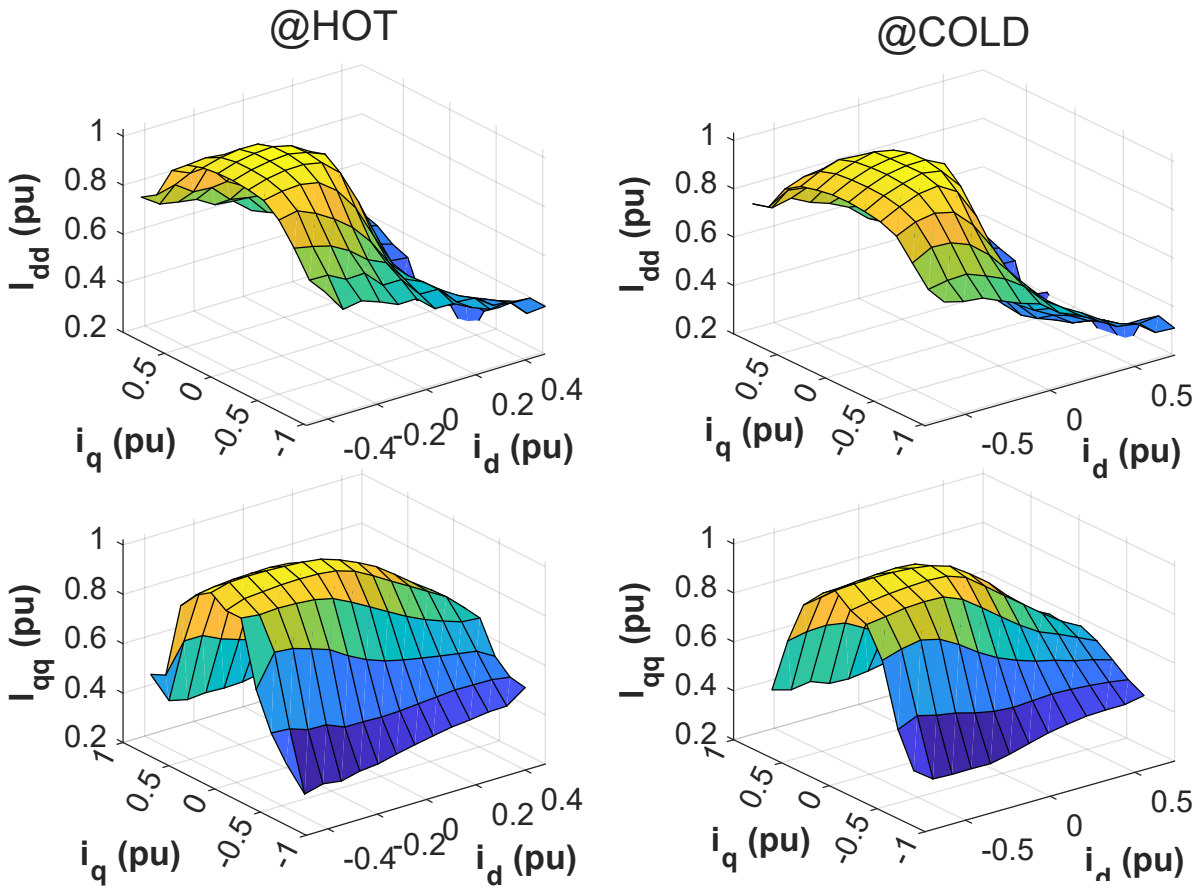

Figure 5.4: Differential inductance maps in the $\mathbf{I}_{dq}$ plane.

In addition, it is possible to determine the machine characteristic profiles (MTPA and MTPV), following the same script adopted in Section 2.2.5.

The results in Figure 5.5, confirm the similarities of the considered AFPM machine with an SPM one from the current-to-flux relation point of view, with the MTPA and the MTPV profiles close to vertical lines.

Furthermore, the condition $|I_0| < I_{max}$ is observed, indicating that the MTPV line can be reached at high speed.

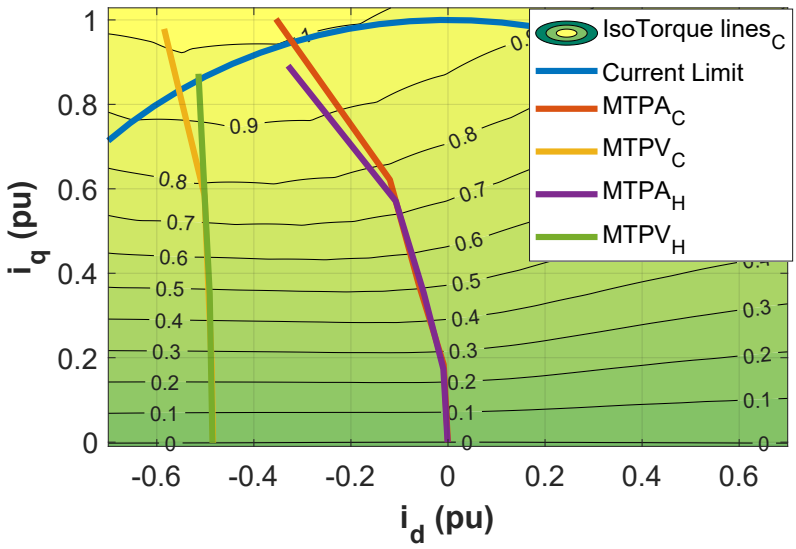

Figure 5.5: IsoTorque lines, current limit, MTPA, MTPV in the $\mathbf{I}_{dq}$ plane.

In addition, in order to preliminarily evaluate the performance of the machine, checking at the same time the accuracy of the nameplate data, the MTPS profiles are computed.

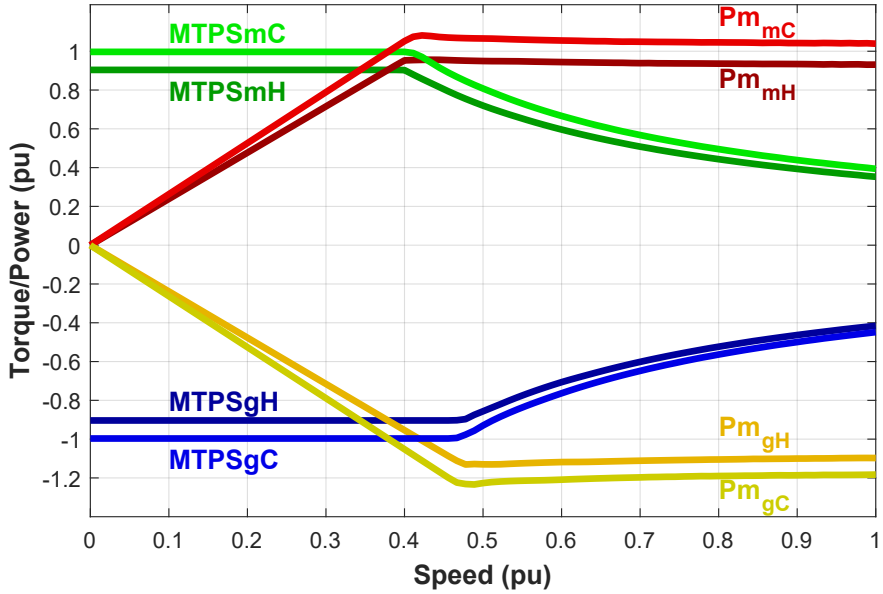

Figure 5.6: Electromagnetic Torque and Mechanical Power in MTPS.

As expected, the performance decreases a bit with the temperature, maintaining however, values close to the nameplate ones.

A good estimate of the torque capability drop can be obtained by considering the electromagnetic torque expression of an isotropic machine:

$$Te = \frac{3}{2} \cdot pp \cdot \left(\lambda_d \cdot i_q - \lambda_q \cdot i_d\right) = \frac{3}{2} \cdot pp \cdot \left(L_d \cdot i_d \cdot i_q + \lambda_m \cdot i_q - L_q \cdot i_q \cdot i_d\right)$$
$$\text{Assuming:} \quad L_d = L_q = L_s \qquad Te = \frac{3}{2} \cdot pp \cdot \left(\lambda_m \cdot i_q\right) \tag{51}$$

Assuming that the peak current point of a vertical MTPA line is maintained before the base speed for both the temperature cases and computing the ratio $K = \frac{\lambda_m = \lambda_d(0, I_{max})@\text{HOT}}{\lambda_m = \lambda_d(0, I_{max})@\text{COLD}}$, the torque ratio $\frac{Te_{HOT}}{Te_{COLD}}$ is approximated as $K \approx 0.91$ before the base speed. In the end, the PM flux decreases with the temperature, causing a nearly corresponding drop in torque capability.

For the 'cold' case, considering low speeds, where the iron losses can be reasonably neglected, the computed electromagnetic torque matches perfectly the peak mechanical torque provided in the datasheet.

In terms of peak mechanical power, even higher values are obtained, but the effect of losses can no more be neglected due to the remarkable speed. Indeed, it is important to consider that these profiles are obtained assuming $\boldsymbol{i}_{mdq} = \boldsymbol{i}_{dq}$, and therefore they result to be quite optimistic, especially at high speed.

5.3 Proposed CVC

Apart from the different control strategies presented in Chapter 4, the presence of isotropy enables the implementation of a very straightforward CVC control.

In addition to the MTPA and MTPV trajectories, another way to check the non-saliency of the Texa machine is looking at the d and q axes apparent inductances L_d and L_q.

Indeed, the isotropic rotor of an SPM is ideally characterized by constant inductance along the entire circumference with $L_s = L_d = L_q$. Similarly, due to symmetry considerations, a similar trend is expected in a non-salient AFPM machine.

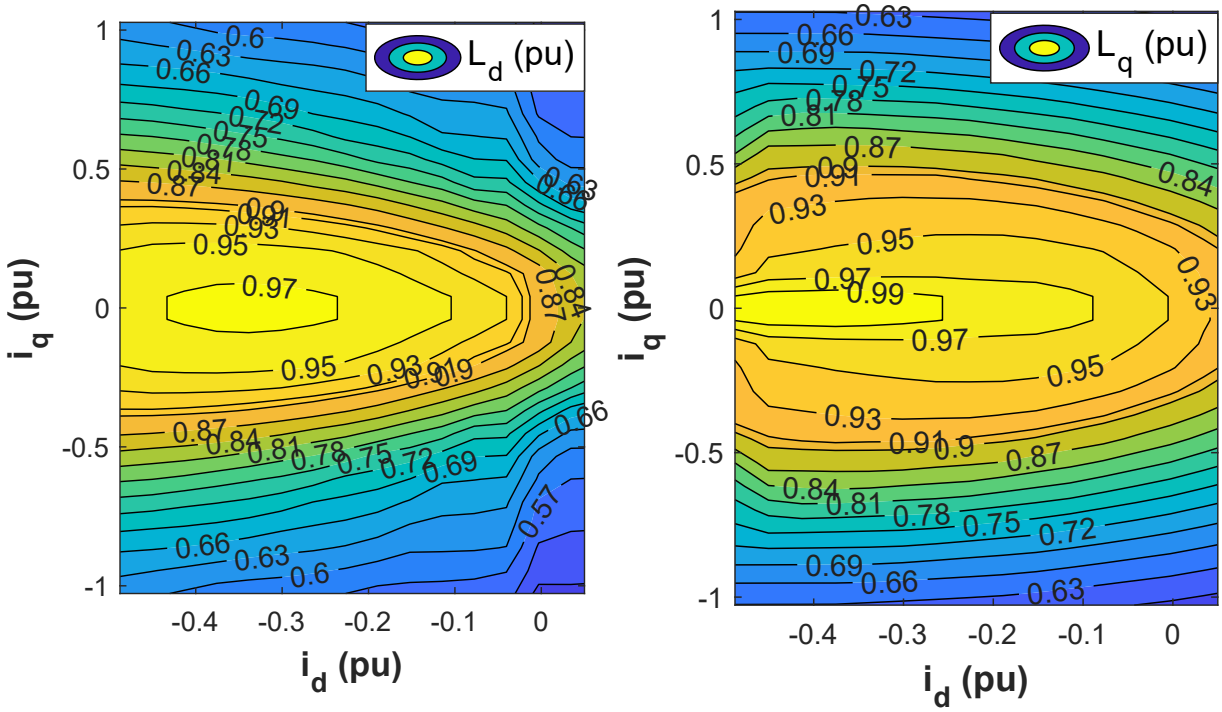

Figure 5.7: dq inductance maps in the $II - III$ quadrants of the $\mathbf{I}_{dq}$ plane @hot.

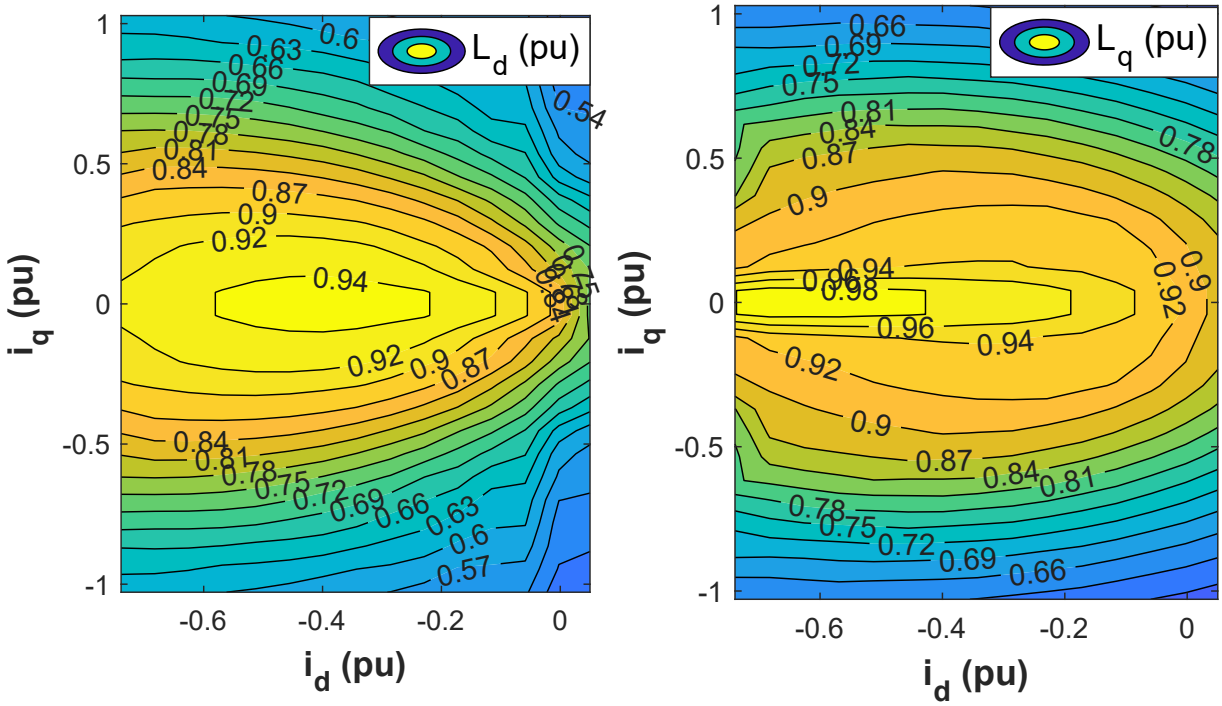

Figure 5.8: dq inductance maps in the $II - III$ quadrants of the $\mathbf{I}_{dq}$ plane @cold.

The Matlab-extrapolated apparent inductances L_d and L_q reported in the Figures 5.7 and 5.8, emphasize the good isotropy of the considered machine, with a very similar trend shown by the two inductances under both rotor temperature conditions. In order to find a unique inductance value L_s, the average between L_d and L_q is computed.

To find an expression that could link the flux-linkage and current magnitude, the dq magnetic model expression (Eq.6) of an isotropic machine is squared on both sides and the two equations are summed to get a third final expression:

$$\begin{aligned} \lambda_d^2 &= L_s^2 i_d^2 + \lambda_m^2 + 2L_s\lambda_m i_d \\ \lambda_q^2 &= L_s^2 i_q^2 \\ \Lambda^2 &= L_s^2 I^2 + \lambda_m^2 + 2L_s\lambda_m i_d \end{aligned} \tag{52}$$

Substituting the BP-flux limit Λ_{LIM} (Section 4.4.1) and the chosen current magnitude limit I_{LIM} and rearranging the expression, a first current limitation on the d-axis is obtained:

$$i'_{d,LIM} = \frac{\Lambda_{LIM}^2 - L_s^2 I_{LIM}^2 - \lambda_m^2}{2L_s\lambda_m} \tag{53}$$

Three cases corresponding to three regions in the $\mathbf{I}_{dq}$ plane are distinguished (Figure 5.9).

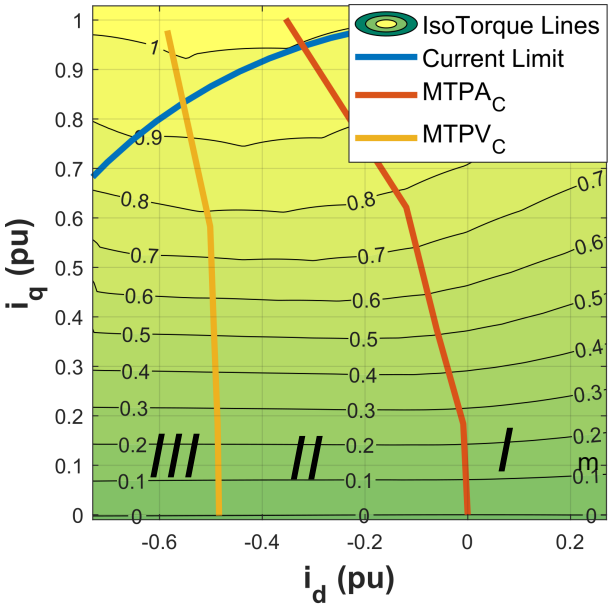

Figure 5.9: Three regions partition of the $\mathbf{I}_{dq}$ plane.

I) $i'_{d,LIM} > 0$, on the MTPA right

II) $I_0 \leq i'_{d,LIM} \leq 0$, between MTPV and MTPA

III) $i'_{d,LIM} < I_0$, on the MPTV left

where I_0 is computed as $\frac{\lambda_m(i_q=0)}{L_s(i_q=0)}$.

For case I): $i''_{d,LIM}$ is forced to 0 and $i_{q,LIM}$ is defined as I_{LIM}.
For case II): $i_{q,LIM}$ is defined as $\sqrt{I^2_{max} - i''^2_{d,LIM}}$, with $i''_{d,LIM} = i'_{d,LIM}$.
For case III): $i''_{d,LIM}$ is set to I_0 and $i_{q,LIM} = \frac{\Lambda_{LIM}}{L_s}$.

Regardless of the case, the torque limit Te_{LIM} is found based on Equation (51) as:

$$Te_{LIM} = \frac{3}{2} \cdot pp \cdot \left(\lambda_m \cdot i_{q,LIM}\right) \tag{54}$$

About the definition of the dq flux limits, the priority is given to the q axis imposing:

$$\begin{aligned} \lambda_{q,LIM} &= \Lambda_{LIM} \\ \lambda_{d,LIM} &= \sqrt{\Lambda^2_{LIM} - \lambda^*_q 2} \end{aligned} \tag{55}$$

Apart from the BP-flux limit, the computation of the other constraints requires the values of λ_m and L_s. By construction (Section 2.1.2), λ_m depends just on the i_q value, hence a simple 1D-LUT can be used. L_s as said, is the result of the average between L_d and L_q. Looking at these latter plots in Figures 5.7 and 5.8, it is evident the horizontality of the contour lines especially in the II and III quadrants where the machine has to be driven. This means a strong L_s dependence on the i_q value as well, resulting in the end in another 1D-LUT.

Once the boundaries for $\boldsymbol{i}_{dq}, \Lambda, \boldsymbol{\lambda}_{dq}, T_e$ are obtained, the reference values $\boldsymbol{i}^*_{dq}, \boldsymbol{\lambda}^*_{dq}, Te^*$ can be determined. The reference torque Te^* is given just by forcing the input reference torque Te^*_{IN} between $\pm Te_{LIM}$.
Subsequently, in order $i^*_q \rightarrow \lambda^*_q \rightarrow \lambda^*_d \rightarrow i^*_d$ are obtained just exploiting Equation(51) and the isotropic version of Equation(6).

Always assuming an isotropic magnetic model (Eq.6), the flux-linkage estimates $\hat{\lambda}_d$ and $\hat{\lambda}_q$ are obtained, defining hence the feed-forward terms as well.

Regarding the PI gains setting, neglecting the cross-differential inductances and assuming $l_{dd} = l_{qq} = l_s$, they are computed for both axes as $k_p = l_s\omega_b^*$ and $k_i = 0.1k_p$, where l_s is updated based on the i_q value as done for L_s and λ_m.

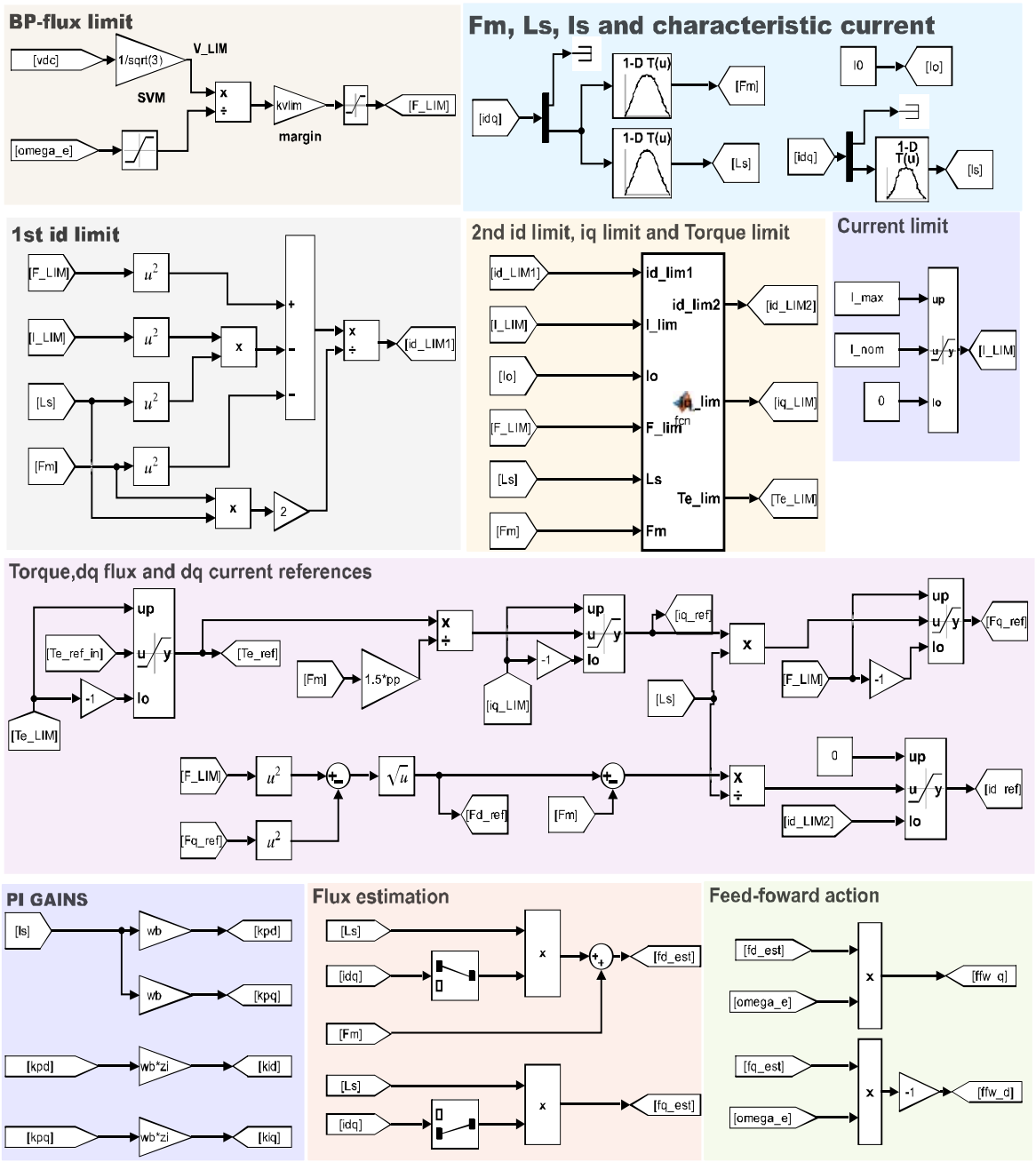

Figure 5.10: Proposed CVC.

To assess the control performance, it is decided to drive the machine under fast torque reversals, passing from the motoring nominal current MTPS profile to the generation counterpart, with settings reported in Table 6.

In addition, to achieve a unified control scheme, the average values of the stator inductance map, of the stator differential inductance map, and of the magnets flux map are computed from the cold and the hot magnetic models.

The loss maps are not provided, therefore for the machine modelling, a flux-based dq model without the iron and PM losses is used (Section 2.3.1). As inverse flux maps, an average between the cold and the hot case, is computed. In addition, based on the datasheet reported values, the stator resistance dynamics is Matlab-reconstructed, mimicking the exponential behaviour given by the skin effect, as well as considering the temperature effect directly in Simulink.

About the inverter, the usual one equipped with Microsemi power devices is considered (Chapter 3) and to speed up the simulation, the PWM modulator is bypassed and the average behaviour given by the duty cycles is considered.

Table 6: Test conditions Texa motor.

Settings			
Initial d-axis flux linkage	λ_{d0}=λ_{PM}	0.6053	pu
Initial q-axis flux linkage	λ_{q0}	0	pu
Stator current limit	$I_{LIM} = I_{nom}$	0.3448	pu
Initial mechanical speed	n_0	0	pu
Mechanical speed enable time	t_ω	0.3	s
Final mechanical speed	n_{max}	1	pu
Acceleration	a	$0.\overline{66}$	pu/s
Initial desired torque	Te^*_0	0	pu
Torque enable time	t_{Te*}	0.05	s
Slope desired torque	Te^*_{Slope}	22.57	pu/s
Reversal frequency desired torque	$f_{Te^*,rev}$	4	Hz
DC-link voltage	v_{dc}	1	pu
SiC-MOSFET junction temperature	T_j	100	° C
Stator temperature	T_{Cu}	80	° C
Dead time	t_{dt}	500	ns
Safety coefficient on voltage	k_{vlim}	0.9	/
Switching frequency	f_{sw}	1e4	Hz
Controller crossover frequency	f_c=$f_{sw}/20$	500	Hz
Controller zero frequency	f_z=$f_c/10$	50	Hz
Phase margin PTO	PM_{PTO}	60	°
PTO crossover frequency	$f_{c,PTO}$	35	Hz
Simulation time	t_{sim}	4	s
Solver details			
Simulink solver	Ode45		
Min step size	auto		
Max step size	1e-5 s		

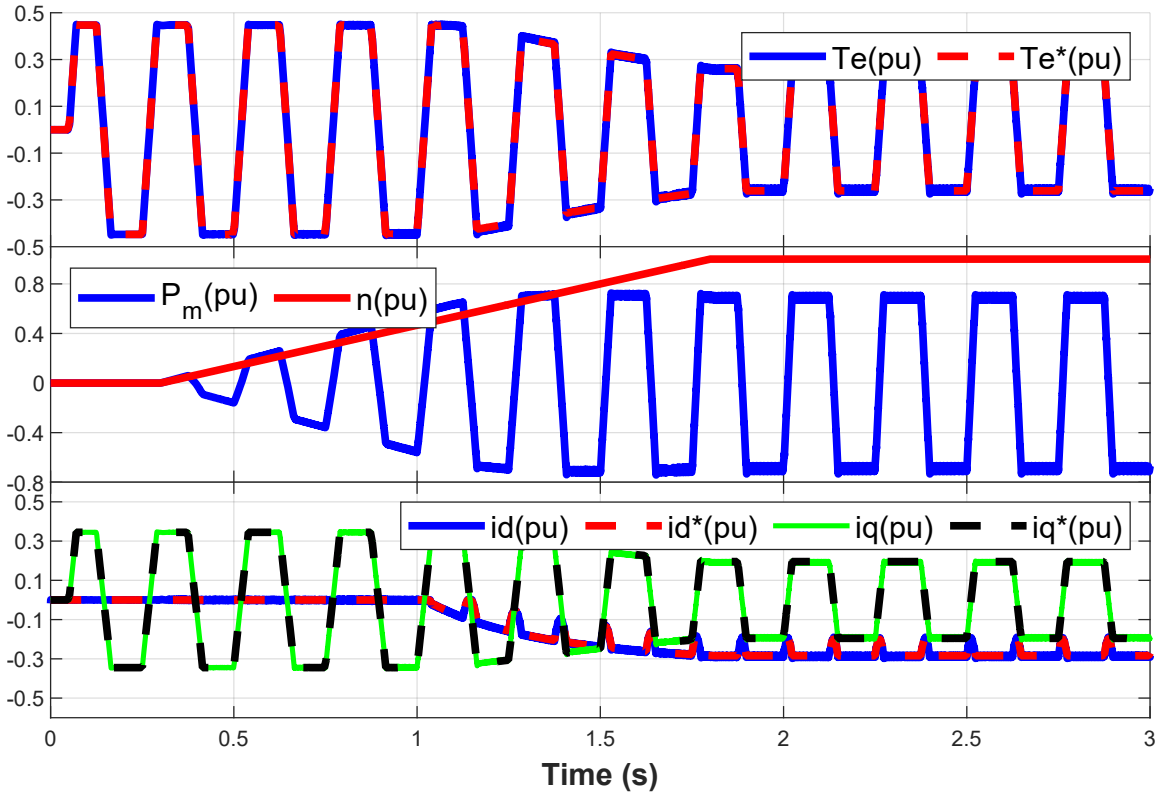

Figure 5.11: Torque, power, speed and dq current dynamics.

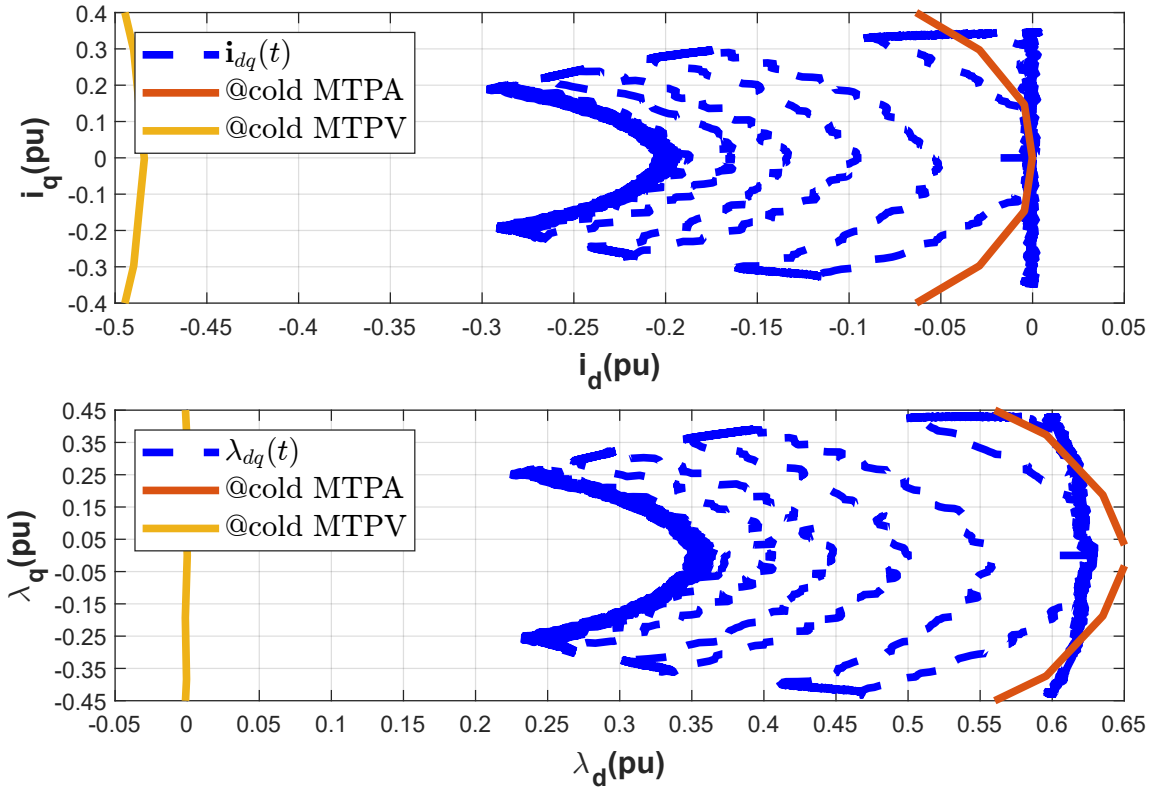

Figure 5.12: dq current and dq flux dynamics in the dq plane.

Based on the results in Figure 5.11, it can be said that the control performance are very satisfactory, with a good torque tracking both at low speed and at high speed (no iron losses are considered in the machine model). In general, the response appears to be quite aligned with the more traditional CVCs (Section 4.4.1).

Focusing on the dq current dynamics both in Figure 5.11 and in Figure 5.12, it is clear the attempt of the control in driving the machine along the vertical line identified by $i_d = 0$, before the flux-weakening starts and hence resembling the MTPA of an ideal isotropic machine.

Then, as soon as the base speed is reached, the control injects current in the negative d axis, going against the magnet flux, decreasing meanwhile the magnitude of the q axis current to fulfill the current limitation set by $I_{LIM} = I_{nom}$. In the end, the dq current and flux trajectories in the flux weakening region are identified by a counterclockwise rotation in the II quadrant and by a clockwise rotation in the III quadrant.

As the maximum speed is reached, there is no more need to decrease the flux and therefore the d axis current is kept steady apart during the q axis current reversal when the q axis reference flux cross the zero and contemporaneously the d axis one assumes the flux limit value, with the consequent increase of i_d.

To sum up, the advantages of the proposed CVC appear to be:

- The control scheme simplicity with just three 1-D LUTs for updating parameters and no control LUTs
- As for the other CVCs, no need to implement a flux observer.

As disavantages instead:

- Possible inaccuracy of the isotropic approximation with higher current values, resulting in torque ripples and possible instability if the voltage safety margin is not increased.
- Regulators' gains are operating-point dependent as for the other CVCs, causing variation in the dynamic performance.

Conclusions and future developments

As demonstrated and highlighted in this text, the digital torque regulation of synchronous machines can be done in several ways.

Apart from predictive controllers, all the others exploit the simplicity provided by proportional-integral regulators, trying to minimize the differences between two estimated or measured variables and their reference values. Predictive controllers offer very high performance, but all the e-drive actors have to be accurately modelled, under the threat of a sudden loss of control. On the other hand, regulation using PI regulators is less effective, but results to be more tolerant to model deviations and parameter uncertainties.

In the end, the controller choice depends by the requirements and is always a trade-off between control structure simplicity, performances and robustness. Balancing these factors is the Control engineer's work, guaranteeing in any case the absolute stability of the control in any operating conditions.

When discussing possible refinements and extensions to this work, the main ones that come to mind are:

- The addition and the control of a boost DC/DC converter upstream, often used to increase the battery voltage, especially in automotive applications.
- The computation of the inverter efficiency map, similarly to what is done with the machine and to get the overall e-drive efficiency and power balance.
- A deeper analysis of the several VSI modulation techniques with their own optimization criteria.
- An extension to the modelling and control of three-phase asynchronous machines.
- A sensor/hardware deeper study to make feasible a real hardware implementation of the controls, validating and checking the veracity of the simulated results.

Appendix

Direct and inverse Clarke transformation

In order to move to a convenient frame for controlling purposes, the first step is to convert a three-phase coordinate system (abc) into a two-phase one ($\alpha\beta$) (Figure 1.3). This operation can be done using the non-power invariant form of the Clarke transformation (A.1), derived from the real and imaginary part extrapolation of the space vector $\boldsymbol{x}(x_a, x_b, x_c)$. In addition, the common mode of the three-phase coordinates (x_a, x_b, x_c) is computed even though it is irrelevant for the torque production.

$$\begin{bmatrix} x_\alpha \\ x_\beta \\ x_0 \end{bmatrix} = \mathbf{T} \begin{bmatrix} x_a \\ x_b \\ x_c \end{bmatrix} = \frac{2}{3} \begin{bmatrix} 1 & -\frac{1}{2} & -\frac{1}{2} \\ 0 & \frac{\sqrt{3}}{2} & -\frac{\sqrt{3}}{2} \\ \frac{1}{2} & \frac{1}{2} & \frac{1}{2} \end{bmatrix} \begin{bmatrix} x_a \\ x_b \\ x_c \end{bmatrix} \tag{A.1}$$

The inverse passage allows the conversion from a two-phase model to a three-phase one (A.2).

$$\begin{bmatrix} x_a \\ x_b \\ x_c \end{bmatrix} = \mathbf{T^{-1}} \begin{bmatrix} x_\alpha \\ x_\beta \\ x_0 \end{bmatrix} = \begin{bmatrix} 1 & 0 & 1 \\ -\frac{1}{2} & \frac{\sqrt{3}}{2} & 1 \\ -\frac{1}{2} & -\frac{\sqrt{3}}{2} & 1 \end{bmatrix} \begin{bmatrix} x_\alpha \\ x_\beta \\ x_0 \end{bmatrix} \tag{A.2}$$

Direct and inverse rotation

To pass from the complex $\alpha\beta$ frame to a rotating dq one associated with the rotor flux (Figure 1.3), a rotation of coordinates is required. The rotation angle θ_d changes in time and corresponds to the position of the d-axis with respect to the α one. Expressing the basis vectors $\boldsymbol{\alpha}$ and $\boldsymbol{\beta}$ in dq coordinates and transposing, the rotation matrix $\mathbf{R}_{\alpha\beta}^{dq}$ or simply $\mathbf{R}$ is obtained.

$$\begin{bmatrix} x_d \\ x_q \\ x_0 \end{bmatrix} = \mathbf{R} \begin{bmatrix} x_\alpha \\ x_\beta \\ x_0 \end{bmatrix} = \begin{bmatrix} \cos(\theta_d) & \sin(\theta_d) & 0 \\ -\sin(\theta_d) & \cos(\theta_d) & 0 \\ 0 & 0 & 1 \end{bmatrix} \begin{bmatrix} x_\alpha \\ x_\beta \\ x_0 \end{bmatrix} \tag{A.3}$$

In the same way, passing from the rotating dq frame to the static $\alpha\beta$ one, involves the use of a rotation ,but this time in the opposite direction.

$$\begin{bmatrix} x_\alpha \\ x_\beta \\ x_0 \end{bmatrix} = \mathbf{R^{-1}} \begin{bmatrix} x_d \\ x_q \\ x_0 \end{bmatrix} = \begin{bmatrix} \cos(\theta_d) & -\sin(\theta_d) & 0 \\ \sin(\theta_d) & \cos(\theta_d) & 0 \\ 0 & 0 & 1 \end{bmatrix} \begin{bmatrix} x_d \\ x_q \\ x_0 \end{bmatrix} \tag{A.4}$$

Direct and inverse Park

Combining (A.1) with (A.3) and (A.2) with (A.4) it is possible to get the expression of the so-called non-power invariant Park transformation (A.5) and its inverse (A.6), passing from the static abc frame to a rotating dq one and vice versa (Figure 1.3).

$$\begin{bmatrix} x_d \\ x_q \\ x_0 \end{bmatrix} = \mathbf{R} \begin{bmatrix} x_\alpha \\ x_\beta \\ x_0 \end{bmatrix} = \mathbf{R} \cdot \mathbf{T} \begin{bmatrix} x_a \\ x_b \\ x_c \end{bmatrix} = \mathbf{P} \begin{bmatrix} x_a \\ x_b \\ x_c \end{bmatrix} =$$
$$= \begin{bmatrix} \frac{2}{3}\cos(\theta_d) & -\frac{1}{3}\cos(\theta_d) + \frac{\sqrt{3}}{3}\sin(\theta_d) & -\frac{1}{3}\cos(\theta_d) - \frac{\sqrt{3}}{3}\sin(\theta_d) \\ -\frac{2}{3}\sin(\theta_d) & \frac{1}{3}\sin(\theta_d) + \frac{\sqrt{3}}{3}\cos(\theta_d) & \frac{1}{3}\sin(\theta_d) - \frac{\sqrt{3}}{3}\cos(\theta_d) \\ \frac{1}{3} & \frac{1}{3} & \frac{1}{3} \end{bmatrix} \begin{bmatrix} x_a \\ x_b \\ x_c \end{bmatrix} \tag{A.5}$$

$$\begin{bmatrix} x_a \\ x_b \\ x_c \end{bmatrix} = \mathbf{T^{-1}} \begin{bmatrix} x_\alpha \\ x_\beta \\ x_0 \end{bmatrix} = \mathbf{T^{-1}} \cdot \mathbf{R^{-1}} \begin{bmatrix} x_d \\ x_q \\ x_0 \end{bmatrix} = \mathbf{P^{-1}} \begin{bmatrix} x_d \\ x_q \\ x_0 \end{bmatrix} =$$
$$= \begin{bmatrix} \cos(\theta_d) & -\sin(\theta_d) & 1 \\ -\frac{1}{2}\cos(\theta_d) + \frac{\sqrt{3}}{2}\sin(\theta_d) & \frac{1}{2}\sin(\theta_d) + \frac{\sqrt{3}}{2}\cos(\theta_d) & 1 \\ -\frac{1}{2}\cos(\theta_d) - \frac{\sqrt{3}}{2}\sin(\theta_d) & \frac{1}{2}\sin(\theta_d) - \frac{\sqrt{3}}{2}\cos(\theta_d) & 1 \end{bmatrix} \begin{bmatrix} x_d \\ x_q \\ x_0 \end{bmatrix} \tag{A.6}$$

Frequency response OL transfer function in the CVC scheme

Based on the CVC OL transfer function (Eq.41), the following Equations (A.7) and (A.8) are extrapolated.

$$|G(jw_c)| = \left|\frac{K_p jw_c + K_i}{jw_c}\right| \cdot \left|\frac{1}{1.5T_{sw}jw_c + 1}\right| \cdot \left|\frac{1}{l_{xx}jw_c}\right| = \frac{\sqrt{K_p^2 + \left(\frac{K_i}{w_c}\right)^2}}{w_c l_{xx} \cdot \sqrt{(1.5T_{sw}w_c)^2 + 1}} = 1 \tag{A.7}$$

$$\begin{aligned} \angle G(jw_c) &= atan2\left(-\frac{K_i}{w_c}, K_p\right) - atan2\left(1.5T_{sw}w_c, 1\right) - 90^\circ \rightarrow \\ PM &= -atan2\left(\frac{K_i}{w_c}, K_p\right) - atan2\left(1.5T_{sw}w_c, 1\right) + 90^\circ \rightarrow \\ tan\underbrace{\left(-PM - atan2\left(1.5T_{sw}w_c, 1\right) + 90^\circ\right)}_{\sigma} &= \frac{K_i}{K_p w_c} \rightarrow K_i = K_p w_c tan\left(\sigma\right) \end{aligned} \tag{A.8}$$

Substituting the last expression in (A.8) into (A.7) and performing some manipulations:

$$\begin{aligned} K_p &= w_c l_{xx}\sqrt{\left((1.5T_{sw}w_c)^2 + 1\right)} \cdot \cos(\sigma) \\ K_i &= w_c^2 l_{xx}\sqrt{\left((1.5T_{sw}w_c)^2 + 1\right)} \cdot \sin(\sigma) \end{aligned} \tag{A.9}$$

While for the simplified design method adopted in Section 4.4.1 the gains are placed as:

$$\begin{aligned} K_p &= w_c l_{xx} \\ K_i &= w_c^2 l_{xx} z_i, \text{ with } z_i \in [0.05, 0.1] \end{aligned} \tag{A.10}$$

Imposing $f_{sw} = 1e4, f_c = \frac{f_{sw}}{20} = 500Hz$ and $l_{xx} = 2e-4H$, with an imposed PM of 60° for the accurate method and $z_i = 0.1$ for the simplified one, the magnitude and phase Bode diagrams of both the OL transfer functions are extrapolated in Figure A.1. In addition, to show the proximity of the OL crossover frequency and the CL bandwidth for systems with good phase margin and unitary feedback, the magnitude Bode diagram of the simplified method CL transfer function is added in Figure A.1.

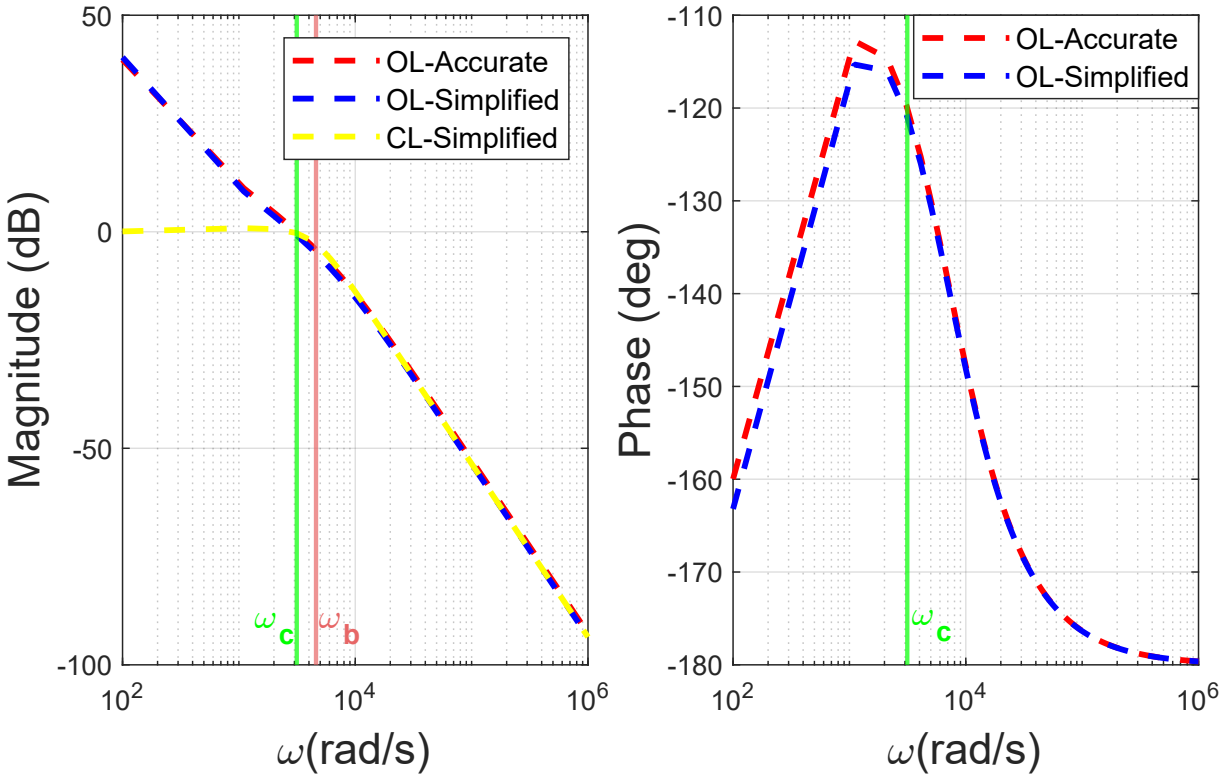

Figure A.1: Bode diagrams comparison OL and CL transfer functions CVC.

References

[1] Simone Ferrari, Paolo Ragazzo, Gaetano Dilevrano, and Gianmario Pellegrino. “Flux-Map Based FEA Evaluation of Synchronous Machine Efficiency Maps”. In: (2021), pp. 76–81. DOI: 10.1109/WEMDCD51469.2021.9425678.

[2] Sam-Young Kim, Chinchul Choi, Kyeongjin Lee, and Wootaik Lee. “An Improved Rotor Position Estimation With Vector-Tracking Observer in PMSM Drives With Low-Resolution Hall-Effect Sensors”. In: *IEEE Transactions on Industrial Electronics* 58.9 (2011), pp. 4078–4086. DOI: 10.1109/TIE.2010.2098367.

[3] A. Vagati, M. Pastorelli, and G. Franceschini. “High performance control of synchronous reluctance motor”. In: 1 (1996), 295–303 vol.1. DOI: 10.1109/IAS.1996.557035.

[4] E. Trancho, E. Ibarra, A. Arias, C. Salazar, I. Lopez, A. Diaz de Guereñu, and A. Peña. “IPMSM torque control strategies based on LUTs and VCT feedback for robust control under machine parameter variations”. In: (2016), pp. 2833–2838. DOI: 10.1109/IECON.2016.7793556.

[5] Bon-Ho Bae, N. Patel, S. Schulz, and Seung-Ki Sul. “New field weakening technique for high saliency interior permanent magnet motor”. In: 2 (2003), 898–905 vol.2. DOI: 10.1109/IAS.2003.1257641.

[6] Gianmario Pellegrino, Radu Iustin Bojoi, and Paolo Guglielmi. “Unified Direct-Flux Vector Control for AC Motor Drives”. In: *IEEE Transactions on Industry Applications* 47.5 (2011), pp. 2093–2102. DOI: 10.1109/TIA.2011.2161532.

[7] Sandro Rubino, Luisa Tolosano, Fabio Mandrile, Eric Armando, and Radu Bojoi. “Flux Polar Control (FPC): A Unified Torque Controller for AC Motor Drives”. In: *IEEE Transactions on Industry Applications* 59.4 (2023), pp. 4140–4163. DOI: 10.1109/TIA.2023.3270110.

[8] Zhuo Hao, Yangyang Ma, Pengyu Wang, Geng Luo, and Yisong Chen. “A Review of Axial-Flux Permanent-Magnet Motors: Topological Structures, Design, Optimization and Control Techniques”. In: *Machines* 10.12 (2022). DOI: 10.3390/machines10121178.

[9] Eric Armando, Radu Iustin Bojoi, Paolo Guglielmi, Gianmario Pellegrino, and Michele Pastorelli. “Experimental Identification of the Magnetic Model of Synchronous Machines”. In: *IEEE Transactions on Industry Applications* 49.5 (2013), pp. 2116–2125. DOI: 10.1109/TIA.2013.2258876.

[10] Eric Armando, Paolo Guglielmi, Gianmario Pellegrino, and Radu Bojoi. “Flux linkage maps identification of synchronous AC motors under controlled thermal conditions”. In: (2017), pp. 1–8. DOI: 10.1109/IEMDC.2017.8002334.